NAVAL POSTGRADUATE SCHOOL
MONTEREY, CALIFORNIA

THESIS

FUSION OF SYNTHETIC APERTURE RADAR DATA AND VISIBLE IMAGERY FROM SIR-C

by

Andrew G. Hartigan

September 1995

Thesis Advisor: R. C. Olsen

Approved for public release; distribution is unlimited

19960327 062

DTIC QUALITY INSPECTED

REPORT DOCUMENTATION PAGE

Form Approved OMB No. 0704-0188

Public reporting burden for this collection of information is estimated to average 1 hour per response, including the time for reviewing instruction, searching existing data sources, gathering and maintaining the data needed, and completing and reviewing the collection of information. Send comments regarding this burden estimate or any other aspect of this collection of information, including suggestions for reducing this burden, to Washington Headquarters Services, Directorate for Information Operations and Reports, 1215 Jefferson Davis Highway, Suite 1204, Arlington, VA 22202-4302, and to the Office of Management and Budget, Paperwork Reduction Project (0704-0188) Washington DC 20503.

1. AGENCY USE ONLY	2. REPORT DATE September 1995	3. REPORT TYPE AND DATES COVERED Master's Thesis

4. TITLE AND SUBTITLE Fusion Of Synthetic Aperture Radar Data And Visible Imagery From SIR-C	5. FUNDING NUMBERS
6. AUTHOR Andrew G. Hartigan	
7. PERFORMING ORGANIZATION NAME(S) AND ADDRESS(ES) Naval Postgraduate School Monterey CA 93943-5000	8. PERFORMING ORGANIZATION REPORT NUMBER
9. SPONSORING/MONITORING AGENCY NAME(S) AND ADDRESS(ES)	10. SPONSORING/MONITORING AGENCY REPORT NUMBER

11. SUPPLEMENTARY NOTES The views expressed in this thesis are those of the author and do not reflect the official policy or position of the Department of Defense or the U.S. Government.

12a. DISTRIBUTION/AVAILABILITY STATEMENT Approved for public release; distribution is unlimited.	12b. DISTRIBUTION CODE

13. ABSTRACT

Remotely sensed imagery from space has typically been done by platforms using only one portion of the electromagnetic spectrum. The SIR-C/X-SAR Space Shuttle mission, however, had the unique opportunity to obtain visible imagery and synthetic aperture radar data from the same platform. SAR and visible images of Norfolk Navy Base in Norfolk, Virginia were successfully merged and analyzed, demonstrating that combining the information from two different parts of the electromagnetic spectrum increases the useful information content of an image. Principal Component Analysis on the radar data demonstrated successful data reduction and feature extraction. Attempts at unsupervised classification using neural network analysis were less successful.

14. SUBJECT TERMS Remote Sensing, Synthetic Aperture Radar, Principal Component Analysis, Data Fusion, Synergism	15. NUMBER OF PAGES 131
	16. PRICE CODE

17. SECURITY CLASSIFICATION OF REPORT Unclassified	18. SECURITY CLASSIFICATION OF THIS PAGE Unclassified	19. SECURITY CLASSIFICATION OF ABSTRACT Unclassified	20. LIMITATION OF ABSTRACT UL

NSN 7540-01-280-5500

Standard Form 298 (Rev. 2-89)
Prescribed by ANSI Std. 239-18 298-102

DISCLAIMER NOTICE

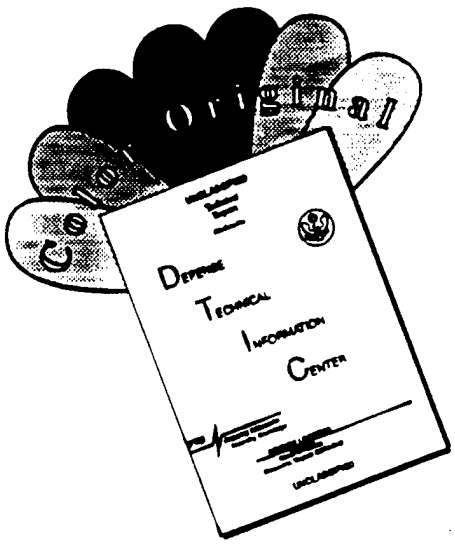

THIS DOCUMENT IS BEST QUALITY AVAILABLE. THE COPY FURNISHED TO DTIC CONTAINED A SIGNIFICANT NUMBER OF COLOR PAGES WHICH DO NOT REPRODUCE LEGIBLY ON BLACK AND WHITE MICROFICHE.

DISCLAIMER NOTICE

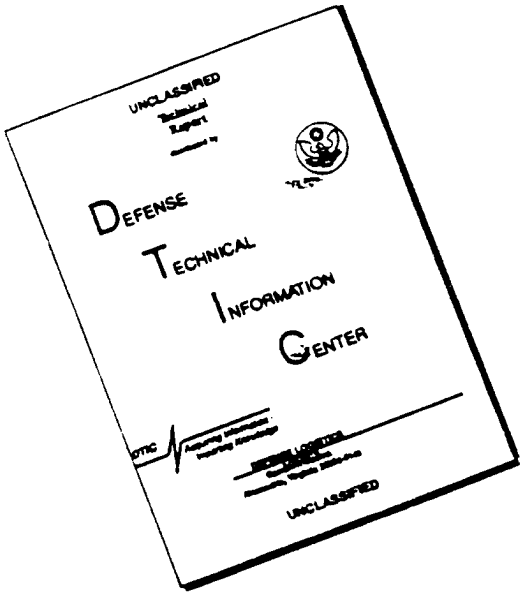

THIS DOCUMENT IS BEST QUALITY AVAILABLE. THE COPY FURNISHED TO DTIC CONTAINED A SIGNIFICANT NUMBER OF PAGES WHICH DO NOT REPRODUCE LEGIBLY.

Approved for public release; distribution is unlimited.

FUSION OF SYNTHETIC APERTURE RADAR DATA AND VISIBLE IMAGERY FROM SIR-C

Andrew G. Hartigan
Lieutenant, United States Navy
B.A., University of Virginia, 1984

Submitted in partial fulfillment
of the requirements for the degree of

MASTER OF SCIENCE IN APPLIED PHYSICS

from the

NAVAL POSTGRADUATE SCHOOL
September 1995

Author: Andrew G. Hartigan

Approved by: R. C. Olsen, Thesis Advisor

Donald Walters, Second Reader

William B. Colson, Chairman,
Department of Physics

ABSTRACT

Remotely sensed imagery from space has typically been done by platforms using only one portion of the electromagnetic spectrum. The SIR-C/X-SAR Space Shuttle mission, however, had the unique opportunity to obtain visible imagery and synthetic aperture radar data from the same platform. SAR and visible images of Norfolk Navy Base in Norfolk, Virginia were successfully merged and analyzed, demonstrating that combining the information from two different parts of the electromagnetic spectrum increases the useful information content of an image. Principal Component Analysis on the radar data demonstrated successful data reduction and feature extraction. Attempts at unsupervised classification using neural network analysis were less successful.

TABLE OF CONTENTS

I. INTRODUCTION.....1

II. BACKGROUND.....3

A. HISTORY OF REMOTE SENSING IN THE VISIBLE WAVELENGTHS.....3

B. HISTORY OF REMOTE SENSING IN MICROWAVE WAVELENGTHS.....9

C. SHUTTLE IMAGING RADAR-C AND X BAND SYNTHETIC APERTURE RADAR (SIR-C/X-SAR).....12

D. PREVIOUS RESEARCH IN MULTISENSOR DATA FUSION....13

III. THEORY.....21

A. RADIATION-MATTER INTERACTION.....21

B. RADIATION-MATTER INTERACTION IN VISIBLE WAVELENGTHS.....23

1. Crystal Field Effect.....24

2. Charge Transfer.....24

3. Conjugate Bonds.....25

C. RADIATION-MATTER INTERACTION IN MICROWAVE WAVELENGTHS.....25

1. Surface Scattering.....27

2. Volume Scattering.....31

3. Scattering Matrix.....32

4. Radar Resolution.....33

IV. PROCESS.....35

V. OBSERVATIONS.....39
A. DIFFERENCES BETWEEN LIKE AND CROSS POLARIZED RADAR IMAGES.....40
B. DIFFERENCES BETWEEN L AND C BAND RADAR IMAGES...41
C. COMBINED FALSE COLOR RADAR IMAGES.....42
D. ADDITION OF VISIBLE IMAGERY TO THE RADAR INFORMATION.....44

VI. ANALYSIS.....49
A. PRINCIPAL COMPONENT ANALYSIS.....49
1. The Covariance and Correlation Matrix.....50
2. Principal Component Transformation.....53
3. Principal Component Analysis of Radar Bands Only.....58
B. NEURAL NETWORK ANALYSIS.....62
1. Background.....62
2. Neural Network Results.....63

VII. SUMMARY.....69

VIII. CONCLUSION.....73

APPENDIX: FIGURES AND IMAGES.....75

LIST OF REFERENCES.....127

INITIAL DISTRIBUTION LIST.....131

ACKNOWLEGEMENT

The author would like to thank Sue Runco and the personnel at the NASA Earth Observation Lab in Houston, Texas for their patient assistance and support throughout this thesis.

The author would also like to thank Tony Freeman and the SIR-C personnel at the Jet Propulsion Lab in Pasadena, California for their technical assistance and timely processing of data.

Thanks also to Professor R.C. Olsen for his academic wisdom and patience.

Finally, a special thanks to the crews of STS-59 and STS-68 for their acquisition of the data and their adventurous pursuit of science.

I. INTRODUCTION

The Department of Defense has a continuous need for remotely sensed tactical information in areas inaccessible to friendly forces. Since 1960, this has been done from space as well as from aircraft. The spaceborne platforms performing this mission have usually done so using only one particular portion of the electromagnetic spectrum. There have been sensors that span both the infrared and the visible wavelengths but there have been few spaceborne sensors dedicated to imaging vastly different portions of the electromagnetic spectrum concurrently, such as the microwave or radar portion of the spectrum, with wavelengths in the centimeter region, and the visible portion of the spectrum, with wavelengths in the hundreds of nanometers region. The Spaceborne Imaging Radar (SIR-C) missions flown in April and October of 1994 on the Space Shuttle Endeavour, however, had the unique opportunity to provide coincident data from the SIR-C synthetic aperture radar, and the 70 mm medium format cameras mounted inside the shuttle. This thesis explored the process of merging the two sets of data digitally to determine whether combining the visible and microwave portions of the electromagnetic spectrum provides more useful information than the individual parts. These combined data sets were analyzed using Principal Component Analysis and a neural network classifier in order classify areas on the earth's surface.

Specifically, images of the Norfolk Naval Base in Norfolk, Virginia were investigated, assuming, as in a tactical warfare situation, that terrain and object classification must be done with limited available ground truth.

II. BACKGROUND

A. HISTORY OF REMOTE SENSING IN THE VISIBLE WAVELENGTHS

Remote sensing is defined as the acquisition of information about an object without being in direct contact with it (Elachi, 1987). In the scientific community, it has evolved over time to mean the remote collection of information related in some way to the earth's natural resources or environment (Slater, 1980). The history of remote sensing, however, demonstrates that improvements in capability have all been a function of technological advancements, many of them driven by the need for better military reconnaissance.

The history of remote sensing began with aerial photography in 1858 when Gaspard Tournachon succeeded in taking a balloon photograph of the village Bievre, near Paris, France. This historic event was due primarily to the invention of the wet plate process of photographic development, invented in 1851, which allowed exposures of less then a couple of seconds to be a suitable means of photography. Still, an exposed plate required very still conditions and needed to be developed within twenty minutes of exposure. (Newhall, 1969)

This new science of obtaining airborne imagery was exploited during the civil war, most notably by the Union

General George McClellan, who used it to survey Confederate positions in Virginia (Avery and Berlin, 1992).

The invention of the dry plate process of photographic development in 1871 allowed the next great improvement in aerial photography. Dry plates did not have to be developed immediately and their exposure time was reduced to small fractions of a second, 60 times faster than the wet plate process. This allowed much higher quality images due to the reduced exposure time and many more images per flight, since they could be developed once on the ground. (Newhall, 1969)

As lens, film, and camera technology became more advanced, smaller, and lighter, cameras were attached to smaller less expensive balloons, kites, and even pigeons. In 1912, Julius Neubronner successfully attached cameras as light as 2 1/2 ounces to pigeons in Cronberg, Germany. (Newhall, 1969)

The development of the airplane was the technological advancement that allowed photographers to take pictures of a particular predetermined site, instead of being at the mercy of the wind or a bird. The first recorded use of aircraft to obtain photography was in 1909 when Wilbur Wright flew a camera over Centotelli, Italy. This method of remote sensing was widely used and improved out of necessity during World Wars I and II. The primary advancements in technology during World War II were the automation of the film advancement in the camera, and the speed of the film processing. By 1943, it was standard for a Mosquitoe

reconnaissance aircraft to carry three cameras each with 500 film negatives. (Newhall, 1969)

Aerial photography reached new heights after World War II as a mission of V-2 rockets that were captured from Germany. In an experiment performed by the Applied Physics Laboratory of The John Hopkins University, a 35 mm motion picture camera was launched on a V-2 rocket from the White Sands Proving Ground in New Mexico in 1946. The camera took continuous pictures during ascent and descent and was ejected from the rocket during descent at approximately 25,000 feet. This was a precursor to the film return method used by satellites in subsequent decades. An Atlas rocket carried a camera to 700 miles in 1959. These rocket platforms, however, did not remain in space long enough to take photos during any time other than the ascent and descent. The development of orbiting satellites allowed the first sustained spaceborne remote sensing platform, the Explorer VI, to be launched in September of 1959. (Newhall, 1969)

The images from the Explorer VI inspired the development of dedicated meteorology satellites. The first of these, TIROS (Television and Infrared Observing Satellite), was a series of ten satellites, launched from 1960 to 1965. TIROS was improved upon in subsequent meteorological satellite systems. The essential imagery of real time weather, short range prediction, and long range forecasts continued to be provided by the following systems; Environmental Science Services Administration,

(ESSA), the Improved TIROS Operating System, (ITOS), and TIROS-N. (Allison and Schnapf, 1983)

Concurrently, the development of military reconnaissance capability was also being applied to orbiting satellite platforms in the top secret CORONA program. In August of 1960, the KH-1 camera system launched on CORONA mission 9009 successfully returned film in a re-entry vehicle which was captured in mid-air by a U.S. Air Force C-119 aircraft. The KH-1 camera had a resolution capability of 12 meters, providing this first successful mission with over 4.1 million square kilometers of Soviet Union reconnaissance coverage. In the heat of the Cold War, rapid advancements were made to the reconnaissance camera systems. Most significantly, camera control, color film type and metering, faster lens systems, and spacecraft thermal control contributed to improvements in imaging systems. The KH-4B camera system achieved a resolution capability of two meters in September of 1967. (McDonald, 1995)

Remote sensing from optical systems continued to diversify among spaceborne platforms for several reasons, most obviously because a much larger area could be imaged without the distortion of a wide angle lens. Also, the orbital mechanics of spacecraft allowed for constant or repetitive observations. (Slater, 1980)

In 1965 the Defense Meteorological Satellite Program (DMSP) was originated with the objective to obtain and disseminate world wide meteorological data on a daily basis.

The payload consisted of two vidicon cameras which provided TV pictures with a resolution of 2.4 km. Relay satellites transmitted real time data to a data reconstruction site. In 1987, upgraded Block 5 series DMSP satellites carried a passive microwave radiometer, (SSM/I), in the first spaceborne attempt to combine both reflected and emitted energy in cloud analysis. This passive microwave sensor operated in the K and Q bands, sensing wavelengths from 8.1 to 15.5 mm. (Kramer, 1992)

In 1972, NASA launched the first Landsat satellite, which was historically significant for the fact that it produced digital imagery. Digital imagery is far more amenable to computer processing techniques than analog imagery, allowing contrast enhancements and feature extraction not necessarily recognizable by the human eye (Strain and Engle, 1992). At the time the satellite was called the Earth Resources Technology Satellite, (ERTS-1). Its primary payload was the Multi-Spectral Scanner, (MSS), which operated in four spectral bands from .5 to 1.1 μm, including the near infrared. Subsequently, Landsat 2 through Landsat 5 have been successfully launched, with the last two Landsats carrying the Thematic Mapper, (TM), as the primary payload. The TM is a scanning optical sensor that increased the resolution capability of Landsat from 79 meters to 30 meters and increased the number of operating spectral bands to seven in the visible and infrared regions, from .45 to 2.35 μm. Landsat has been a major supplier of

earth imagery for both scientific and military applications over the course of its lifetime. (Gupta, 1991)

Continuing improvements in launch vehicle capability permitted satellites to reach geostationary altitudes. This allowed continuous observation from a single platform that covered almost a third of the earth's surface. In 1974, The National Oceanographic and Atmospheric Association ,(NOAA), began to launch the Geostationary Operational Environmental Satellites, (GOES), to take advantage of this capability as a geostationary meteorological satellite constellation. The primary payload, Visible Infrared Spin Scan Radiometer, (VISSR), operates with 8 visible channel detectors and 12 spectral bands of infrared information. (Kramer, 1992)

The latest major optical sensor system in orbit is the French SPOT satellite constellation (Systeme Probatoire d'Observation de la Terre). SPOT-1 was launched in 1986, and carries a High Resolution Visible sensor, (HRV), as its primary payload. The HRV operates in three spectral bands which cover the visible wavelengths from .5 to .89 μm, with a resolution of 20 meters. There is also a panchromatic mode (black and white imagery) which has a spatial resolution of ten meters, and covers the portion of the visible spectrum from .51 to .73 μm. SPOT has increased commercially available resolution capability and made possible the digital merging of its panchromatic band with other sensors to increase their spatial resolution capability as well. This process is addressed later in this thesis. (Kramer, 1992)

B. HISTORY OF REMOTE SENSING IN MICROWAVE WAVELENGTHS

Radar as a remote sensing tool has its origins in Real Aperture Side Looking Radar, (SLAR), developed in the early 1950's. This was the result of advances in antenna design, microwave components, and radar recording techniques developed to provide high resolution imagery useful for military reconnaissance. (Moore, 1983)

SLAR systems do not have fine resolution capability from long range, since the along track range resolution, (r_a), is a function of the radar wavelength, (λ), the antenna length, (D), and the range to the target, (R):

$$r_a = \frac{\lambda R}{D} \qquad \text{Equation 2.1}$$

This limitation led to the development of synthetic aperture radar, (SAR), which has no range or wavelength dependence on the along track resolution or the cross track resolution. For synthetic aperture radar the resolution can approach the following theoretical limit:

$$r_a = \frac{D}{2} \qquad \text{Equation 2.2}$$

This feature makes SAR systems particularly attractive for long range and space based radar remote sensing applications. (Moore, 1983)

The first SAR imaging system used in earth orbit was the oceanographic satellite Seasat, launched in 1978.

Seasat carried an L-band SAR, operating at approximately 1.28 GHz, with a 25 meter resolution capability. The radar transmitted and received horizontally polarized electromagnetic waves and had a 20 degree look angle relative to the vertical. Seasat generated only 70 days of operational data before a power failure ended its mission, however this data was used extensively in ice and ocean monitoring. (Kramer, 1992)

The next spaceborne SAR was the Shuttle Imaging Radar, (SIR-A), launched on the Space Shuttle in November of 1981 with the mission of evaluating SAR as a tool for geological mapping. This radar was also an L-band HH radar. It had a resolution cell size of approximately 40 meters and a 47 degree look angle. (Simonett, 1983)

SIR-B was launched on the Space Shuttle in October of 1984. This was the first spaceborne SAR capable of varying the radar look angle at the earth's surface. The three look angles of 28°, 45°, and 58° were analyzed in an attempt to understand the complexity of microwave backscatter at varying radar incidence angles. SIR-B improved the resolution cell size of the radar pixels to 25 meters. (Lozano-Garcia and Hoffer, 1993)

Numerous papers have been written using results from the SAR systems on the SIR-A and SIR-B shuttle missions. The most comprehensive source of these SAR references found in the search for background material is located on the NASA Jet Propulsion Lab, (JPL), home page on the World Wide Web. One publication on forest type classification by

Lozano-Garcia and Hoffer [1993], is reviewed further in this chapter.

Each of the first two SIR missions was flown with a Large Format Camera, (LFC), on board the space shuttle. This 450 kg camera generated an image format size of 23 x 46 centimeters and had a resolution capability of 15 meters. In a comprehensive literature review, several technical papers written on the earth observation imagery of the LFC were found from a search of the NASA Technical Report Server at the following World Wide Web address: http://techreports.larc.nasa.gov/cgi-bin/NTRS; however, no publications were found which addressed merging of synthetic aperture radar and LFC visible data.

The most recently launched unmanned orbiting SAR platforms are the ERS-1 and the JERS-1, launched in 1991 and 1992 respectively. The European Remote Sensing Satellite, (ERS-1), has an imaging mode capable of 30 meter resolution using C-band VV polarization radar at an incidence angle of 23°. The Japanese Earth Resources Satellite, (JERS-1), has an 18 meter resolution capability, using L-band HH polarization at a look angle of 35.2°.

Several publications using the ERS-1 data are listed on the JPL document mentioned above. One paper by R.M. Hoffer [1994], applied to the classification of Eucalyptus tree stands is reviewed later in this chapter. A set of compact discs of excellent JERS imagery was released by the National Space Development Agency of Japan in 1994.

C. SHUTTLE IMAGING RADAR-C AND X BAND SYNTHETIC APERTURE RADAR (SIR-C/X-SAR)

The synthetic aperture radar data used in this analysis was provided by the Shuttle Imaging Radar, SIR-C/XSAR. This radar was flown on Space Shuttle flights STS-59 and STS-68 in April and October of 1994. The radar consists of an antenna structure and associated hardware designed to fit within the payload bay of the Space Shuttle. The antenna is a 12 x 3.7 meter, 10,500 kg array of separate panels (Figure 1). The antenna consists of two planar arrays, one for L-band, operating at 23.5 cm wavelength and one for C-band, operating at 5.8 cm wavelength. The power output of the radar is 5.2 kW for the L band and 1.3 kW for the C band. The X-band radar antenna operates separately from the L and C band antennas. X-band radar data were not used in the analysis due to difficulty in acquiring and unpacking usable data. Each planar array contains a grid of hundreds of small low power solid state dual polarized microstrip transmitters embedded in the surface of the antenna. These radiators can transmit and receive both vertically and horizontally polarized waves. This allows for the SIR-C to collect four different combinations of radar backscatter, HH (horizontally transmitted, horizontally received), HV (horizontally transmitted, vertically received), VH (vertically transmitted, horizontally received), and VV (vertically transmitted, vertically received). In addition, measurements include the relative phase difference between

the HH, VV, VH, and HV returns. This allows for the derivation of the complete scattering matrix of each pixel within a scene. The beam can be steered +/- 23 degrees from the nominal 40 degree off nadir position. (Freeman and Chapman, 1994)

D. PREVIOUS RESEARCH IN MULTISENSOR DATA FUSION

Previous research in multisensor data fusion has investigated techniques to improve surface classification accuracy by using more of the information available from the electromagnetic spectrum.

Guindon et al. [1980], from the Canada Center for Remote Sensing applied the fusion of airborne synthetic aperture radar, an airborne multispectral scanner, and Landsat data to the classification of forest types in British Columbia. The radiometric and geometric correction procedures required in rugged topography received particular attention. The conclusion was that the 11 channel airborne multispectral scanner, spanning from .38 to 14 μm provided the same weighted average classification accuracy of 88% that a combined 12 band SAR-Landsat data set provided. The 12 band data set was the best four bands from each of the three sensors. The following table summarizes these results.

Data Set	Weighted Average classification accuracy
11 Channel Airborne MSS	88%
Best 4 Channel Airborne MSS	72%
8 Channel SAR	69%
Best 4 Channel SAR	49%
SAR (shallow incidence angle)	49%
SAR (steep incidence angle)	45%
Landsat MSS	44%
12 Best bands (SAR, AMSS, LMSS)	88%
8 SAR + 4 Landsat	83%

Table 2.1: From Guindon et al. [1980], Results of combined airborne SAR, MSS, and Landsat data applied to Forest Type Classification in British Columbia

S. T. Wu [1982], of NASA applied the fusion of Seasat L-band and aircraft X-band dual polarized synthetic aperture radar data with four band Landsat MSS data to the problem of land type classification in the Western Kentucky coal region. Since there was a high degree of correlation between MSS bands, only two of the bands were used in the combined classification process. In unsupervised classification of seven land cover types, the percentage of pixels classified correctly improved in every case for the combined five band data set over the SAR bands and the MSS bands separately.

Land Cover Types	SAR (3 bands)	MSS (4 bands)	SAR/MSS (5-bands)
Pasture	46.9%	81.3%	96.7%
Forest	92.3%	88.0%	92.5%
Residential	10.0%	59.4%	79.0%
Soybean Field	89.5%	59.4%	90.9%
Corn Field	88.3%	32.5%	99.0%
Water	99.9%	97.4%	99.9%
Strip Mine	64.9%	47.7%	77.4%
Overall	48.2%	64.2%	81.1%

Table 2.2: From S. T. Wu [1982], Results of combined Seasat and Landsat data applied to the classification of the Kentucky Coal Region

P.S. Chavez [1986], of the U.S. Geological Survey applied the process of sensor fusion to Landsat TM data and panchromatic photography from the National High Altitude Program (NHAP). He successfully demonstrated the benefits of sensor fusion by maintaining the spectral resolution of Landsat TM while incorporating the spatial resolution of NHAP.

R. Welch and M. Ehlers [1987], of the University of Georgia merged data from the newly launched SPOT-1 satellite with Landsat TM data. After the TM data had been resampled to ten meter resolution using parametric cubic interpolation for smoothing purposes, they found striking success in merged image contrast and spectral discrimination by using an intensity-hue-saturation (IHS) transformation process. This process, which is fully documented in Haydn et al [1982], is started by transforming three resampled TM bands

from the Red-Green-Blue color space into the IHS domain. The ten meter panchromatic SPOT data is then substituted for the intensity band of the IHS image and the new IHS image is transformed back into the RGB color domain. Although this research combined two different types of visible information, having nothing to do with SAR, it is relevant to this work in that the merged three band image contained information from four separate spectral bands of image data.

D. G. Leckie [1990], of Petawawa National Forestry Institute demonstrated that registered radar, visible, and infrared data were better at forest type classification than any of the bands individually, (See Figure 2). First, all possible combinations of the four polarization components of C and X band airborne SAR (8 total radar bands), five visible, three near infrared, and one mid infrared bands of an airborne multispectral scanner were analyzed. It was found that a 5 band combination of near-IR, green, mid-IR, X_{vv} and C_{hh} provided close to the maximum classification accuracy obtainable using all bands.

D. F. Lozano-Garcia and R.M. Hoffer [1993], combined SAR data from the SIR-B mission of the Space Shuttle with Landsat TM data in an effort to demonstrate synergistic classification capabilities over forests in Northern Florida. This was the first time spaceborne radar data could be obtained and analyzed from different incidence angles; 28°, 45°, and 58°. The best classification performance was obtained using a subset of 4 bands of data; green, near IR, and mid IR from the TM, and 28° L_{hh} radar

data from the SIR-B. This provided better classification than even the combination of all ten bands. This is demonstrated with respect to the classification of swamps, clear-cut, young pine, pine, old pine, and water in the following table.

Number of channels	Average classification accuracy (%)	Channels utilized*
2	79.6	5,10
3	84.4	4,5,10
4	88.4	2,4,5,10
5	88.2	2,4,5,7,10
6	86.8	2,4,5,7,9,10
7	86.7	2,3,4,5,7,9,10
8	84.6	2,3,4,5,7,8,9,10
9	84.9	2,3,4,5,6,7,8,9,10
10	84.2	1,2,3,4,5,6,7,8,9,10

Table 2.3: From Lozano-Garcia and Hoffer [1993], Results of combined SIR-B data and Landsat TM data applied to Forest Classification in Northern Florida

* where: channel 1 is Landsat .45-.52 μm
channel 2 is Landsat .52-.60 μm
channel 3 is Landsat .63-.69 μm
channel 4 is Landsat .76-.90 μm
channel 5 is Landsat 1.55-1.75 μm
channel 6 is Landsat 2.08-2.35 μm
channel 7 is Landsat 10.4-12.5 μm
channels 8,9,10 are SIR-B, L-band HH polarization at incidence angles 28°, 45°, and 58° respectively

R.M. Hoffer [1994], applied this synergy of SAR and TM data to the classification of Eucalyptus stands in Gerais, Brazil. The data source in this case for SAR was ERS-1. The results of this study demonstrated that TM data alone classified Eucalyptus stands better than the combined data set. Apparently, adverse topographic effects in areas of rolling terrain degraded the SAR data. The results of the study are summarized below.

Classification Type	Landsat TM accuracy	ERS-1 SAR accuracy	Combined accuracy
Medium Eucalyptus	93.4%	0.0%	91.0%
Young Eucalyptus	92.7%	78.0%	91.1%
Pasture	96.7%	51.7%	96.1%
Bare Soil	83.9%	38.4%	62.5%
Lake	94.7%	64.1%	92.7%
River	98.0%	67.9%	67.3%
Cloud	100%	67.8%	65.3%
Overall classification accuracy	94.8%	35.7%	85.9%

Table 2.4: From Hoffer [1994], Results of combined ERS-1 data and Landsat TM data applied to Eucalyptus stand classification in Gerais, Brazil

Chiuderi, et al., [1994] combined the concept of multisensor data fusion with neural network classifiers to demonstrate improved classification abilities of agricultural areas near Florence, Italy. The data set included images from a P, L, and C band multipolarization SAR flown on board a DC-8 aircraft, and a 12 channel

multispectral scanner, (TMS), covering visible and IR wavelengths flown on board an ER-2 aircraft. Two separate neural network classification methods showed improved classification accuracy when SAR data was added to the MSS data set. The first study employed a backpropogation neural network. The classification accuracy of wheat, woods, alfalfa, vineyards, bare soil, and grassland was 65.68% using TMS data alone, but improved to 90.68% using the SAR data as well. The second study employed a self-organizing-map neural network approach. The classification accuracy improved from 97.88% to 98.73% when SAR data was added to the TMS data set.

Previous work by this author was done with data from the STS-59 SIR-C Space Shuttle mission using SAR and Space Shuttle medium format photographic imagery of Mount Pinatubo, in the Republic of the Philippines. Figure 3 is an R-G-B color image taken from the hand held Hasselblad camera onboard the space shuttle. Figure 4 is a false color composite image of three of the radar bands; L-band HH, L-band HV, and C-band HV are color mapped in red, green, and blue respectively. Clearly, there is much greater detail in the mountainous features of the radar composite image than in the photograph. The mudflows, called 'lahars', in the radar image, however, show no radar return at all from their origin near the cinder cone all the way to the ocean at the left side of the image. The visible photograph, on the other hand, shows significant variations in the detail of the lahars, while not breaking out any of the detail of

the mountainous terrain. The L-band HH, the C-band HV, and the blue band of the rgb image were combined to show both the mountainous detail and the detail of the mudflows in one image (Figure 5). This result is a clear demonstration that a combination of features in each of the two portions of the electromagnetic spectrum increases the overall information content of the image. The objective of the following analysis is to demonstrate this in a scene of greater military relevance.

III. THEORY

A. RADIATION-MATTER INTERACTION

Electromagnetic energy is detectable only through its interaction with other matter. When EM energy strikes matter, there are four fundamental interactions that can occur. Transmission is the process by which EM energy passes through matter without any detectable attenuation. Specular reflection is the process of EM energy "bouncing off" matter in an equal and opposite direction from which it came. Scattering, sometimes called diffuse reflection, involves the re-emissions of radiation from rough surfaces relative to the incident wavelength. Absorption is the attenuation of EM energy within a medium. In the process of absorption, radiation is converted into thermal energy within the medium, which is then re-radiated or emitted from the body. Remote sensors detect and measure the reflected, scattered, or emitted electromagnetic radiation from an object or area from some distance. (Avery and Berlin, 1985)

The interaction of matter with EM radiation is clearly a function of the wavelength of the incident radiation. The difference in wavelengths is the primary difference between the visible and the microwave portions of the electromagnetic spectrum (See Figure 6). Another significant difference between the visible and radar remote sensing instruments used for this thesis study is the difference between an active and a passive system. The

incident EM energy for visible wavelength remote sensing is provided by the sun, hence, no artificial radiation source is required. Synthetic aperture radar, however, must provide its own source of microwave energy, then measure the received component. This is an active system. It is this feature that allows radar to be a viable sensor even at night.

Every object interacting with electromagnetic energy emits and reflects energy with unique characteristics that are a function of its physical state and molecular and chemical properties. This distinctive property is called a spectral signature. For the purpose of classifying items in a remotely sensed image, it is desirable to expand the band of frequencies that are analyzed to ensure that the uniqueness of an objects spectral signature is identified. (Avery and Berlin, 1985)

The purpose of this thesis study is to analyze the utility of combined radar and visible wavelengths when applied to the classification of objects based upon their spectral signatures. The following discussion of the radiation-matter interactions of the different portions of the electromagnetic spectrum is intended to help understand what features cause differences in spectral signatures.

B. RADIATION-MATTER INTERACTION IN VISIBLE WAVELENGTHS

Specular reflection occurs in wave-matter interaction when the material is smooth relative to the incident wavelength. The reflection coefficient, R, is a function of the incidence angle, θ, and the complex index of refraction, n. This interaction varies for vertically and horizontally polarized waves:

$$|R_h|^2 = \frac{\sin^2(\theta-\theta_t)}{\sin^2(\theta+\theta_t)} \qquad \text{Equation 3.1}$$

$$|R_v| = \frac{\tan^2(\theta-\theta_t)}{\tan^2(\theta+\theta_t)} \qquad \text{Equation 3.2}$$

Where θ_t is the transmission angle, and $\sin\theta = n\sin\theta_t$. The reflection coefficient as a function of incidence angle for two different values of the index of refraction is plotted in Figure 7. (Elachi, 1987)

Most natural surfaces, however, are rough relative to the incident wavelength, therefore scattering and absorption play a more predominant role. Multiple scattering from a particulate surface results in some energy being reflected toward the medium, sometimes penetrating the medium. If the material has an absorption band, the reflected energy is depleted of energy in that band. (Elachi, 1987)

The result of this absorption in visible remote sensing is the cause of the colors we see in objects. For example, an object that absorbs all wavelengths within the visible spectrum except for blue will appear blue to the human eye.

An object that absorbs all wavelengths will appear black and an object that reflects all wavelengths will appear white.

The actual mechanisms responsible for different absorption bands are primarily electronic excitation processes within the atoms and molecules reacting with the impinging electromagnetic energy. The most important of these processes involve the crystal field effect, charge transfer, and conjugate bonds.

1. Crystal Field Effect

In solid materials, valence electrons of adjacent atoms form electron pairs that hold the atoms together. In the case of certain elements, this leaves unpaired electrons in unfilled inner shells. These electrons have excited states that are strongly affected by the electrostatic field of the surrounding crystalline structure. These excited states of the unpaired electron often have frequency ranges that fall into the visible spectrum. (Elachi, 1987)

2. Charge Transfer

In some cases, when the electron pairs described above are bound by less energy, they are not confined and can move about through a macroscopic solid. These electron pairs have the ability to transfer charge from one ion to another.

For example, the blue sapphire contains the impurities Fe^{+2}, and Ti^{+4}. When an electron is transferred from the iron to the titanium, giving both ions a +3 charge, an excited state is formed, creating an absorption band from the yellow through the red. The result is the deep blue color of the sapphire. (Elachi, 1987)

3. Conjugate Bonds

The loosely bound electron pair described above plays a major role in the spectral response of many organic compounds, including biological pigments. These substances contain a system of alternating single and double atomic bonds called conjugate bonds. The transfer of a pair of electrons from a single to a double bond causes a reversal of the bonds, resulting in an excited state with absorption in the visible wavelengths. The chlorophyll in plants is a classic example of this type of spectral characteristic. (Elachi, 1987)

C. RADIATION-MATTER INTERACTION IN MICROWAVE WAVELENGTHS

The uniqueness of the SIR-C synthetic aperture radar platform lies in its ability to both transmit and receive horizontally and vertically polarized waves. The following discussion is the theory of radar backscatter and an attempt to understand the differences between like and cross polarized returns. A more thorough understanding of these

differences will greatly aid in the exploitation of the SIR-C data.

The classical radar equation expresses power returned to the receiving antenna as a function of the transmitter power, P_t, antenna gain, G, the radar cross section of the incident surface, σ_{rt}, and the receiving antenna area, A, modified by isotropic spreading functions and atmospheric attenuation.

$$P_r = \frac{P_t G \sigma_{rt} A}{(4\pi r^2)^2} e^{-2\alpha r} \qquad \text{Equation 3.3}$$

While the radar transmitting and receiving characteristics are fixed, having been designed into the radar, it is the interaction of the microwave signal with the surface of the earth which warrants thorough discussion.

Radar images are representations of the power received for each of the individual picture elements, or pixels, within a scene. Each pixel represents the average radar backscatter reflected to the radar antenna from that specific area on the earth. The backscatter can be expressed as a coefficient, σ, that is defined as the ratio of energy received by the receiving antenna over the energy that would have been received if the surface reflected the incident energy isotropically. The scattering coefficient is a function of polarization, look angle, wavelength, and the interaction properties of the target; geometric, dielectric, and conductive. Modeling the backscatter properties of a given area on the earth incorporates both

surface and volume scattering models. For example, an area of vegetated terrain would involve surface scattering from the air-vegetation and vegetation-ground interfaces as well as volume scattering from the zone within the vegetation. (Fung and Ulaby, 1983)

1. Surface Scattering

A simple model of the surface scattering process involves a series of large facets with superimposed roughness. An electromagnetic wave incident on the surface creates an electric field at the surface of the facet. This will cause an excitation of the atomic oscillators within the material that is a function of the dielectric property of the medium. These new electromagnetic oscillators then reradiate energy isotropically from the incident material. The re-radiated energy that is opposite in direction from the incident radiation minus the energy lost due to atmospheric attenuation and isotropic spreading is the energy received by the radar antenna. (Elachi, 1987)

For a perfectly conducting, smooth rectangular facet of dimensions L and b parallel to the x and y axes respectively, an incident plane wave of either vertical or horizontal polarization in the x-z plane results in the following backscatter coefficient:

$$\sigma(\theta) = \frac{4\pi b^2 L^2}{\lambda^2}\left[\frac{\sin(kL\sin\theta)}{kL\sin\theta}\right]^2\cos^2\theta \qquad \text{Equation 3.4}$$

where: $\sigma(\theta)$ = the backscatter coefficient as a function of the angle of incidence relative to the vertical

λ = wavelength

$k = 2\pi/\lambda$

(Fung and Ulaby, 1983)

This facet backscatter is plotted as a function of θ in Figure 8. A reradiated field from a single facet would have a field similar to an antenna with the dimensions of the facet. This simple model, however, assumes roughness scales larger than the wavelength of the incident electromagnetic wave and incidence angles less than 30°. For larger angles of θ, the primary surface scattering is due to Bragg scattering, or point source scattering, where roughness scales of horizontal dimension L are the predominant contributor when L meets the following condition.

$$L = \frac{\lambda}{2\sin\theta} \qquad \text{Equation 3.5}$$

This is also demonstrated in Figure 8. (Elachi, 1987)

To account for the superimposed roughness on a facet, the model assumes incident electromagnetic waves upon a sphere. If the radius of the sphere is less than 1/10 of the incident wavelength, then the Rayleigh scattering cross section applies, which is expressed in the following equation and is independent of the angle θ.

$$\sigma_{rt} = 64\pi^5\left(\frac{\varepsilon-1}{\varepsilon+2}\right)^2\left(\frac{r^6}{\lambda^4}\right) \qquad \text{Equation 3.6}$$

where: σ_{rt} = the backscatter cross section expressed in meters

r = radius of sphere

ε = complex dielectric constant

If the sphere is greater than approximately 1.6 times the wavelength of the incident radiation, then Rayleigh scattering no longer applies and the spheres' radar cross section is equivalent to its geometric cross section, modified by the dielectric constant:

$$\sigma_{rt} = [\frac{\varepsilon^{1/2}-1}{\varepsilon^{1/2}+1}]^2 \pi r^2 \qquad \text{Equation 3.7}$$

Combining these different shapes, sizes and slopes of slightly rough surfaces, polarized surface backscattering can be represented by the following first order expression according to Fung and Ulaby, 1983.

$$\sigma_{pp}(\theta) = 8k^4h^2\cos^4\theta|\alpha_{pp}|^2 W(2k\sin\theta) \qquad \text{Equation 3.8}$$

where pp = polarization

$k = 2\pi/\lambda$

h^2 = variance of surface heights

α_{PP} = Fresnel reflection coefficient for a given polarization

$W(2k\sin\theta)$ the Fourier transform of the correlation coefficient of the normalized roughness spectrum

This expression is valid only for small values of h compared to λ. The α_{pp} Fresnel reflection coefficient is dependent upon the incidence angle and the properties of the material. In the case of the VV and HH polarization for example,

$$\alpha_{vv} = (\varepsilon_r - 1)[\sin^2\theta - \varepsilon_r(1 + \sin^2\theta)][\varepsilon_r\cos\theta + (\varepsilon_r - \sin^2\theta)^{1/2}]^{-2} \qquad \text{Equation 3.9}$$

$$\alpha_{hh} = (1 - \varepsilon_r)(\cos\theta + \sqrt{\varepsilon_r - \sin^2\theta})^{-2} \qquad \text{Equation 3.10}$$

where ε_r = the relative permittivity of the surface.

Figures 9 and 10 show this difference in backscatter for horizontal and vertical polarization for slightly rough surfaces. The three lines on each plot demonstrate the effect of the size of the roughness, l. For each plot the relative permittivity of the surface is assumed constant, and $k = 2\pi/\lambda$. For random surfaces of small scale roughness, these expressions are valid for incidence angles less than approximately 30 degrees. For larger angles of θ, the primary surface scattering is due to Bragg scattering as described earlier in the chapter.

For large scale roughness, where $h \geq \lambda$:

$$\sigma = \pi \sec^4\theta |R|^2 p(\tan\theta) \qquad \text{Equation 3.11}$$

where p = slope probability

R = specular reflection coefficient

(Larson, 1994)

2. Volume Scattering

Volume scattering can be represented in a simple closed form solution for the case of a continuous inhomogeneous medium with small permittivity fluctuations and no discontinuities at the top surface of the volume. The horizontally polarized backscatter coefficient for a horizontally polarized incident wave at incidence angle θ is:

$$\sigma_{hh}(\theta) = 2\pi^2 \left| \frac{kT_\perp \cos\theta \cos(\theta-\phi)}{\cos\phi(\varepsilon_a \cos\theta + \sqrt{\varepsilon_a}\ \cos\phi)} \right|^2 W(2k\sin\theta) \qquad \text{Equation 3.12}$$

where: ϕ is related to θ by Snells law

$k = 2\pi/\lambda$

$T_\perp$ = Fresnel transmission coefficient for horizontal polarization

$W(2k\sin\theta)$ is the Fourier transform of the spectrum of the random permittivity function $\varepsilon_1(x,y)$

ε_a = The average value of the inhomogeneous permittivity, $\varepsilon(x,y,z)$

(Fung and Ulaby, 1983)

This θ dependence is plotted in Figure 11. In this plot, σ^2 is identical to h^2 in the above equations, W is expressed as follows.

$$W(2k\sin\theta) = h^2 l^2 [1 + 4k^2 l^2 \sin^2\theta]^{-3/} \qquad \text{Equation 3.13}$$

The overall backscatter coefficient for a medium capable of both surface and volume scattering can be assessed using the principle of superposition of the above properties. However, this is not the case when an area is dominated by multiple scattering. A signal scattered multiple times before returning to the receiver antenna takes a slightly longer path than a signal scattered only once. This results in a slight phase delay, increasing the cross polarization component of the return signal. This is illustrated in Figure 12. (Fung and Ulaby, 1983)

Radar images produced by like polarizations (HH, VV) are empirically different from those produced by cross polarizations (HV, VH) because of the differences in the physical processes involved during the interaction of the electromagnetic wave and the surface. The primary process responsible for like polarized returns is the combined effect of surface and volume scattering. The dominant mechanisms contributing to cross polarized returns are multiple scattering due to large scale target roughness and multiple volume scattering due to inhomogeneities. Still, there are many differences between like and cross polarized returns that are not yet understood. (Larson, 1994)

3. Scattering Matrix

The fully polarametric capabilities of the SIR-C radar will help to increase our understanding of the polarization characterization of the scattered electromagnetic field.

The radar backscatter coefficient for each pixel is broken down into the scattering matrix. The scattering matrix [**S**] is related to the backscatter cross section σ_{rt} by the following expression:

$$S_{ij} = \sqrt{\sigma_{rt_{ij}}}\, e^{j\theta_{ij}} \frac{1}{\sqrt{4\pi R^2}} \qquad \text{Equation 3.14}$$

$$\text{where} \quad S_{ij} = \begin{bmatrix} S_{hh} & S_{hv} \\ S_{vh} & S_{vv} \end{bmatrix} \qquad \text{Equation 3.15}$$

S is a complex value.
If the scattering matrix is referenced in phase to S_{hh}, then the scattering matrix is characterized by three amplitudes and two relative phases, $S_{vh} = S_h$. (Onstott, 1994)

$$S = e^{j\theta_{hh}} \begin{bmatrix} S_{hh} & S_{hv} e^{j(\phi_{hv}-\phi_{hh})} \\ S_{vh} e^{j(\phi_{vh}-\phi_{hh})} & S_{vv} e^{j(\phi_{vv}-\phi_{hh})} \end{bmatrix} \qquad \text{Equation 3.16}$$

This breakdown of the radar backscatter coefficient is what allows for representation of an image in each of the like polarizations, VV and HH, the cross polarization, HV, and the phase difference.

4. Radar Resolution

The resolution cell of each pixel in a synthetic aperture radar image is measured in the along track and range direction. The along track dimension, δ_y, of the pixel is simply a function of the actual antenna array length, D.

$$\delta_y = \frac{D}{2} \qquad \text{Equation 3.17}$$

The dimension in the range direction is a function of the frequency bandwidth, **B,** of the radar and the incidence angle θ. c is the speed of light.

$$\delta_x = \frac{c}{2B}\cos\theta \qquad \text{Equation 3.18}$$

For the SIR-C radar, the 12 meter antenna length dictates an along track resolution cell capability of six meters. The actual demonstrated along track resolution, however, is eight meters, due to a weighting applied during processing to reduce sidelobe levels. The incidence angle θ varies from 17 to 63 degrees and the signal bandwidth varies from 10 to 20 MHz, resulting in a worst case 15 meters range resolution. To get a square pixel, several looks are averaged in azimuth, resulting in a higher quality image with the reduced resolution of 25 x 25 meters.

IV. PROCESS

The Norfolk Navy Base was selected as the site for this analysis after a comprehensive and unsuccessful search for visible and radar images that were obtained concurrently. Littoral sites of naval significance were checked for available radar data via the JPL SIR-C Home Page on the Internet. Focusing on a geographic area was achieved with a point and click map index on this home page. Individual datatake frames were then accessible for viewing. This proved to be an effective yet time consuming process.

Visible data were acquired from the Earth Observation Lab at Johnson Spaceflight Center in Houston, Texas. Nadir lists of all photographs taken on the SIR-C flights were reviewed to narrow down the search to a particular geographic area. Selected individual rolls of film were then viewed for images of littoral sites of naval interest. Radar and visible data of the Norfolk, Virginia area provided the best coincident data available; however, the time difference of these datatakes was seven hours and 45 minutes. Once the visible imagery was located and digitized in Houston, JPL provided data tapes of the same site.

SIR-C radar data were labeled Datatake ID 97_20, taken by mission STS-68 at 09:29:56 GMT on 6 October, 1994. The data product received was multi-look complex data containing like and cross polarized information for horizontally transmitted C and L band wavelengths. Radar incidence angle was 34.7°. The datatake provided a strip of radar imagery

approximately 100 by 43 kilometers which was cropped to cover the area of interest. The data was unpacked using software provided by JPL, then scaled appropriately to capture the entire dynamic range. Resolution of each pixel is approximately 25 x 25 meters. An X-band data tape was received from the German Space Agency, DLR. This data was not extractable from the digital tape and therefore not used in the analysis.

Visible imagery was in a positive 70mm film format, taken at 17:15:13 GMT on 6 October, 1994 from a modified medium format Hassleblad camera. This image, labeled 68-237-057, was then digitized using an Eikonix digitizer. It must be pointed out that digitization is a potentially error inducing process for the data. The digitizer is a CCD array which digitizes the light received from a light table over which the film image is placed. Adjusting tonal quality to match the original image is a subjective process of the human eye, aided by histogram optimization. Focusing is done through a view finder and difficult to adjust precisely. Finally, image scanning takes several minutes, during which any vibration to the light table affects image output quality. This process was performed several times to best match the color, contrast, and tone of the digitized image to the original film image. A 62.7 km square image was digitized to a 1696 x 1696 pixel array, resulting in a pixel resolution of approximately 37 x 37 meters.

The visible data were geo-registered to the radar data using a 3rd order polynomial transformation and resampled

using bilinear interpolation. This was done using the GCP Works package within PCI Remote Sensing software. (PCI, 1994)

The individual bands of radar data and individual color bands of the R-G-B image were combined for observation purposes using the Environment for Visualization (ENVI) software package within IDL software. Principal Component Analysis of the data was performed using PCI software.

Finally, the neural network classification process was performed using a Kohonen Self Organizing Map program written in IDL. (Gautreaux, 1995)

V. OBSERVATIONS

The imagery used in the analysis is the immediate vicinity surrounding the Norfolk Navy Base in Norfolk, Virginia. The overall region is known as the Tidewater Area of Virginia. The Chesapeake Bay, the James River, and the Elizabeth River surround the Navy base on three sides. The land mass on which the base lies, and the area across the James River is known to be a primarily residential and commercial area. There is significant industry and commercial shipping activity along the Elizabeth River. Figure 13 shows a map that outlines the analyzed area.

Figures 14 and 15 are C band HH and C band HV images respectively. Figures 16 and 17 are the L band HH and L band HV images respectively. There are several noteworthy differences in the radar images; differences between the two frequency bands and differences between the two polarization types. These differences are described and explained when possible in the following paragraphs. The observations acquired when adding the visible information, Figures 18 and 19, to the radar data are then addressed. Ground truth data for comparison is limited, as it would be in a tactical situation, to map data and some human intelligence information.

A. DIFFERENCES BETWEEN LIKE AND CROSS POLARIZED RADAR IMAGES

In the cross polarized images, Figures 14 and 16, the overall returns from the land areas are brighter than they are in the like polarized images, Figures 15 and 17. These areas are known to be primarily residential, with a great number of buildings, neighborhoods, and shopping areas. This type of surface results in multiple scattering of the incident microwave radiation, therefore the brightness difference between polarization types supports the fact that multiple scattering causes depolarization of EM waves. This overall increase of brightness in the returns over the like polarized images improves the contrast between the light and dark features on the cross polarized imagery. This makes the roads and inland waterways more easily identifiable. The areas where there is little difference between the like polarized and crossed polarized images are not culturally built up areas. For example, the large square peninsula on the left side of the image, Craney Island, is known to be a once marshy area, recently having been used as a land fill area.

Both like polarized images have more noticeable variations in the returns from the land areas than do the cross polarized images. There are pockets of increased return intensity which indicate a different surface feature or different surface geometry that is not recognizable in the cross polarized imagery. Some of these areas of

increased returns are completely saturated in the like polarized images, providing limited useful information. These same areas in the cross polarized images, however, are not saturated and do have identifiable detail. For example, the peninsula of the southern portion of the Norfolk Naval Base is completely saturated in the C_{hh} image of Figure 14, whereas, in the C_{hv} image of Figure 15, the peninsula area is broken up into separate areas of recognizably different intensity returns. This area is known to contain several warehouses and shipping storage facilities.

A final noteworthy difference between the two different types of polarizations is in the representation of ships' wakes, visible in the like polarized imagery of Figures 14 and 16, but not visible in the cross polarized imagery of Figures 15 and 17. This is the only feature noticeable from the water areas in any of the images. The water overall appears to have no return in all bands and polarizations, except for areas of wake activity. This is explained by the predominance of specular reflection in the radars interaction with water. The one exception to this observation is the lighter areas in the lower right portion of the water in the C_{hv} image of Figure 15. Since this lighter area appears over the land as well as the water, this is assumed to be noise in the data.

B. DIFFERENCES BETWEEN L AND C BAND RADAR IMAGES

Both L band images clearly have more detail in some areas of the image than in the C Band. This is most

apparent in the land-water interface area south of Craney Island and the Portsmouth Coast Guard Facility on the western shore of the Elizabeth River. This region is known to be an undeveloped land area, containing primarily grassland, and marshland nearer the shore. This difference in detail may be partially due to the power output of the transmitters and the receiver noise figures. The power outputs are 5.2 kW for L band and 1.3 kW for C band.

Both L band images show more sharpness between the light and dark areas than in the corresponding images for the C band. This is most evident in the street and waterway definition in the entire Norfolk area.

The most significant observable difference between the two frequency bands is the representation of the airfield on the Norfolk Naval Base. This feature is clearly visible in both C band images, Figures 14 and 15, yet not visible at all in the L band images, Figures 16 and 17. The airfield area could actually be misinterpreted as water in the L band images. This is not a function of the printed image, the difference is the same on a digital display with all manners of contrast stretching applied. This lack of return near the airport in L band is not clearly understood.

C. COMBINED FALSE COLOR RADAR IMAGES

Based upon the above observations of the differences between each of the different radar/polarization images, several false color images were created, with three of the

four bands represented as red, green , and blue in each image. The following table indicates which images are represented in the appropriate Figures.

Figure	Red Band	Green Band	Blue Band
20	C band HH	C band HV	L band HV
21	L band HH	L band HV	C band HH
22	C band HH	C band HV	L band HH
23	C band HV	L band HV	L band HH
24	L band HH	L band HV	C band HV

Table 5.1: Composite Radar Image Combinations

The combination of the radar bands allows features from each of the bands to be portrayed in one image. The L_{hv} band provides the best contrast between lines of communication and inland waterways, so false color images including this particular band were sharper. Only those images with both C bands represented the Naval Airfield well. All combinations represented the area south of the Portsmouth Coast Guard Facility and west of the Elizabeth River clearly. For these reasons, the best combination of radar bands found to represent the scene is Figure 20. The contrast of Figure 21 is actually better, but the airfield is nearly invisible in that image.

Figure 20 portrays the strength of the cross polarized returns of the residential areas throughout the whole image in blue with the L_{hv} band. The small areas within the

residential areas which were highlighted in both HH images are represented in red with the C_{hh} band. The land fill areas on Craney Island, the area south of the Coast Guard Facility and the area outlining the airport are represented in green with the C_{hv} band. There are also many significant returns represented in white; they are the objects which have strong returns in all radar bands, namely, the ships at pierside, the warehouses on the Naval Base, and the industrial areas and warehouses along the Elizabeth River. It is noteworthy that the colors in the image are fairly uniform in tone. There is little significant variation within the blues the reds or the greens that is normally seen when combining these three colors into one image.

D. ADDITION OF VISIBLE IMAGERY TO THE RADAR INFORMATION

The original visible image is shown in Figure 18. The image is predominantly blue in color, with several shades of browns and dark greens. The red, green, and blue pixels which comprise the image are depicted in the histogram plot of Figure 25. This plot demonstrates that in the area of the greatest number of pixels (brightness values of 60 to 180) the blue band is significantly brighter than the red or green bands. It is the variety in shade and color throughout the image which is the major contribution that the visible bands can add to the radar information. The R-G-B image which resulted from the registration with the radar images is presented in Figure 19. Significant

resolution, sharpness, and detail has clearly been lost in the registration and warping process. The first significant observation is the differences in the water area of the image. The lighter shades of blue and shades of brown in the water are likely to be variations in sediment or water depth. This is information unavailable in the radar bands. The land in the Norfolk area also has significant varieties in color, especially in the area of the Lafayette River, which is the inlet just south of the Norfolk Navy Base and the residential areas east of the base. There is little other useful information in the image as it is by itself, however, its contribution to tonal variety is evident when displayed with the radar bands in one image.

Based upon the predominance of the blue band in the R-G-B image, it was the visible band selected to display with the radar bands in false color composite images. The correlation between both red and green when compared to the blue indicates that little information is lost when the green and red bands are eliminated. This high degree of correlation is illustrated in Figure 26 and quantified in the next chapter.

Figures 27 - 30 contain band combinations as listed in the following table.

Figure	Red Band	Green Band	Blue Band
27	C band HH	L band HH	Blue
28	C band HH	L band HV	Blue
29	C band HV	L band HH	Blue
30	C band HH	Green	L band HH

Table 5.2: Composite Radar and Visible Band Combinations

The combined images of Figures 27 and 28 can be compared to the combined radar-only images of Figures 20 and 21. The obvious difference is the addition of variations in the once uniform colors of the combined radar image. The homogeneously colored residential areas now display different shades of green and blue as well as areas of yellow. No detail is lost in Figure 27, yet the variation in the water of the James River and Chesapeake Bay is retained. An attempt was made at using a visible band other than the blue band in Figure 30. This image appears to have lost significant detail and sharpness. Clearly, this portion of the study requires more ground truth data to understand the reasons for the gradations in color and benefits of adding color imagery to radar data.

There is a limitation to studying the combined effects of seven bands of radar and visible imagery by combining only three of the bands in one false color image. This method entirely eliminates the information in the other four bands. It is desirable to use all of the information

available from the seven bands and still present that information in one image. This process is made possible using Principal Component Analysis and is addressed in the next section.

VI. ANALYSIS

The overall goal of analyzing remotely sensed imagery of the earth is to understand the images presented and the information contained within them. The analysis in the previous chapter attempted to simply observe the images themselves and combine them in different ways to determine if there was an optimal way of organizing the data. The following sections provide an alternative method of inspecting the data and organizing it based on spectral and spatial characteristics into different categories of information. This was done using principal component analysis and neural network analysis.

A. PRINCIPAL COMPONENT ANALYSIS

Given the georegistered four radar and three visible bands of data, each pixel in the scene represents a seven element vector, in which each element represents the brightness level in one of the seven bands. This vector characteristic of the data permits spectral transformations, providing an alternative representation of the data to possibly discern features not evident in the original individual bands. This process also has the potential to compress the useful information in the image into fewer bands for ease of data manipulation. The following discussion of the covariance matrix and principal component transformation is simplified at times to two

dimensions. However, the mathematical logic is applicable to an unlimited number of dimensions. The discussion follows the logic of Richards, [1993].

1. The Covariance and Correlation Matrix

Given a scatter plot of any band of data with another, with each axis labeled from 0 to 255 as a brightness scale as shown in Figure 31, there is a mean value (**m**) of pixel brightness for each axis. For example, on the x axis:

$$\mathbf{m} = \frac{1}{K}\sum_{j=1}^{K} x_j \qquad \text{Equation 6.1}$$

where K = the total number of pixels

The covariance matrix, Σ_x, describes the spread or scatter of the pixels in the scene from the average value **m**.

$$\Sigma_x = \frac{1}{K-1}\sum_{j=1}^{K}(\mathbf{x}_j - \mathbf{m})(\mathbf{x}_j - \mathbf{m})^t \qquad \text{Equation 6.2}$$

where t denotes the transpose of the matrix.

The covariance matrix for a pair of spectral bands will demonstrate a high degree of correlation between the bands if the off diagonal elements of the matrix are large, approaching the magnitude of the diagonal elements. No correlation between the bands will be represented by zero valued off diagonal elements.

The 4 radar bands and 3 visible bands have the following 7 x 7 symmetrical covariance matrix:

	chh	chv	lhh	lhv	red	green	blue
chh	8300.64						
chv	1605.84	834.32					
lhh	5018.32	1061.53	4944.42				
lhv	1184.85	498.75	969.68	489.65			
red	725.86	225.29	494.47	193.26	664.79		
green	503.21	141.31	335.93	124.63	559.20	509.90	
blue	272.26	61.46	188.22	63.71	401.30	392.90	356.04

Table 6.1: Covariance Matrix of seven band Principal Component Analysis

A more easily interpretable means of representing the correlation of the bands is the normalized correlation matrix **R** with matrix elements q:

$$q_{ij} = v_{ij}/\sqrt{v_{ii}v_{jj}} \qquad \text{Equation 6.3}$$

where v_{ii} and v_{jj} represent the elements of the covariance matrix.

The following correlation matrix demonstrates more clearly the relationship between the 7 different bands:

	chh	chv	lhh	lhv	red	green	blue
chh	1						
chv	.610	1					
lhh	.783	.523	1				
lhv	.588	.780	.623	1			
red	.309	.303	.273	.338	1		
green	.245	.217	.212	.249	.960	1	
blue	.158	.113	.142	.153	.825	.922	1

Table 6.2: Correlation Matrix for seven band Principal Component Analysis

This correlation matrix demonstrates that among the radar bands, the highest degrees of correlation are between the like polarized components for each frequency band, approximately 78%. The degree of correlation between the like frequencies with different polarizations in the radar bands is between 61 and 62.3%. Among the visible wavelengths, the green band is highly correlated with each of the red and blue bands, at 92.2 and 96%. The correlation between the red band of the visible wavelengths and all of the radar bands varies from 27.3% to 33.8%. This level of correlation between each of the radar bands and the visible bands becomes smaller as the wavelengths in the visible spectrum become shorter: i.e., the correlation between the green band and the radar bands varies from 21.2% to 24.9%, and the correlation between the blue band and the radar bands ranges only from 11.3% to 15.3%.

2. Principal Component Transformation

The principal component transformation is the coordinate rotation which removes all correlation from the bands, resulting in orthogonally related image spaces and a new covariance matrix with zero valued off diagonal elements. In a two dimensional vector space, if the vectors representing the pixel brightness in the new coordinate system are displayed in the y direction, it can be shown that there is a linear transformation **G** of the original coordinates, such that:

$$\Sigma_y = G \Sigma_x G^t \qquad \text{Equation 6.4}$$

where Σ_x is the covariance matrix of the pixel data in x space, **G** is the matrix of eigenvectors of Σ_x, and Σ_y is the diagonal matrix of eigenvalues of Σ_x:

$$\Sigma_y = \begin{matrix} \lambda_1 & 0 & 0 \\ 0 & \lambda_2 & 0 \\ 0 & 0 & \lambda_n \end{matrix} \qquad \text{Equation 6.5}$$

where n is the dimensionality of the data.

$\lambda_n =$ eigenvalues of Σ_x

In the case of the seven bands under analysis, the **G** matrix, or eigenvector matrix, and the Σ_y matrix are as follows:

band	chh	chv	lhh	lhv	red	green	blue
1	-0.78861	-0.16721	-0.56742	-0.13183	-0.0807	-0.05682	-0.03223
2	-0.34325	-0.11083	0.63379	-0.00584	-0.44871	-0.40802	-0.31679
3	0.47957	-0.02003	-0.50722	-0.11641	-0.45964	-0.41758	-0.33636
4	-0.16848	0.81739	-0.10274	0.51357	-0.03969	-0.1014	-0.1316
5	0.04254	-0.53854	-0.09187	0.83278	0.03492	-0.03487	-0.06138
6	0.00929	0.03476	-0.00862	0.10563	-0.60928	0.02879	0.78449
7	-0.00058	0.00002	0.00147	0.02442	-0.45482	0.80224	-0.38594

Table 6.3: Eigenvectors of Covariance Matrix for seven band Principal Component Analysis

This eigenvector matrix is the rotation or transformation matrix **G** that is applied to the original bands to create the principal component bands. Each band listed represents one of the seven principal components. The table indicates that the first principal component band is most heavily weighted with information from the C_{hh} radar band and also significantly weighted with information from the L_{hh} band based on the values for these bands that are relatively higher than the others. The second principal component is most heavily weighted with information from the L_{hh} band, with significant contributions from all three visible bands as well as the C_{hh} band. Each of the principal component bands weightings can be determined from the above table. The image representations of these bands are presented in Figures 32 - 38.

The variances of the pixel data in the transformed coordinate system are presented in the Σ_y matrix, which is the covariance matrix of the new vector space.

$$\Sigma_y = \begin{matrix} 12571.2 & & & & & & \\ 0 & 1371.6 & & & & & \\ 0 & 0 & 1313.6 & & & & \\ 0 & 0 & 0 & 644.9 & & & \\ 0 & 0 & 0 & 0 & 118.9 & & \\ 0 & 0 & 0 & 0 & 0 & 71.2 & \\ 0 & 0 & 0 & 0 & 0 & 0 & 7.9 \end{matrix} \qquad \text{Equation 6.6}$$

From this matrix, it can be determined that the first principal component accounts for 78.09 % of the total variance of the entire data set. This is determined with the following expression:

$$\lambda_1 / \sum_{i=1}^{7} \lambda_i \qquad \text{Equation 6.7}$$

Similar calculations can determine the variance accounted for in each of the subsequent principal component bands. The entire variance of the transformed coordinate system is accounted for as follows:

Band	Variance
1	78.09%
2	8.52%
3	8.16%
4	4.01%
5	0.74%
6	0.44%
7	0.05%

Table 6.4: Variances of Principal Component bands one through seven

This table demonstrates that 78.09% of the variance of the seven image bands is contained in the first principal component and that 98.78% of the total variance is contained in the first four bands. This process has effectively compressed the information contained in seven image bands into four. It is not acceptable, however, to disregard the latter bands as pure noise because even though they represent a significant deviation from the mean of the data, they can sometimes represent localized detail. (Richards, 1993)

The first principal component image in Figure 32 shows more detail and differentiation than any of the radar bands individually, particularly in defining roads and inland waterways. It does not, however, contain the same detail as some of the combined radar images, Figures 20 - 24, or combined radar and visible images, Figures 27 - 29. This is most evident in the returns that are almost entirely black. The southern portion of the Navy Base piers, for example, does not display any detail in the first principal component, whereas it does in the combined radar band images.

The second and third principal components, Figures 33 and 34, clearly contain significant amount of information from the visible bands. This is not only evident in the images, but also in the **G** matrix, Table 6.3. These images display the different shades throughout the residential areas of Norfolk, but significantly sacrifice detail over the entire image.

It is clear that the subsequent individual principal component band images contain less and less information and more noise in Figures 35 through 38. This is supported by the variance values in Table 6.4. Principal Component six, Figure 37, is noteworthy in that it appears to have had the majority of cultural objects removed from the scene, leaving only the local existing topography.

The first three principal components are combined using red, green, and blue false colors to represent principal components one, two, and three respectively in Figure 39. This image clearly differentiates six categories of color; pink, red, light green, dark green, blue, and cyan. This is more differentiation in color than the combined radar images, and is comparable to the color differentiation in the combined visible and radar images. More ground truth would be required to determine whether these six colors classify six different types of terrain and structure. Detail is lost in many areas of the image, particularly the roads and inland waterways. This is due to the contributions of principal components two and three, which contain significant information from the visible bands which have a poorer resolution in the georegistered image.

It is important to note in this combined image, Figure 39, that the red color of the cloud in the upper left corner does not necessarily indicate that the cloud, which is a visible feature only, is strongly represented in principal component one. Table 6.3 clearly indicates limited amounts of visible information in the first principal component and

the cloud is not visible at all in Figure 32, which is the first principal component image. This red feature actually indicates a complete lack of any information in that region in principal components two and three, which are the blue and green bands of Figure 39. This ambiguity in combined principal component images should make an observer cautious of classification conclusions based solely on a color presentation of the principal component analysis.

3. Principal Component Analysis of Radar Bands Only

A principal component analysis was performed on the four radar bands, C_{hh}, C_{hv}, L_{hh}, and L_{hv} to determine whether the principal components provided information on features not discernible in any of the individual bands or if it condensed the useful information of four bands or radar data into fewer bands of principal components.

The correlation matrix, R, four this four band principal component analysis is a subset of the seven band correlation matrix, Table 6.2, minus the visible information. The correlation between the radar bands is precisely the same, with a higher degree of correlation between like polarizations than between like radar frequencies. The least amount of correlation is between bands with both different frequencies and polarizations. This is illustrated in the following table.

	chh	chv	lhh	lhv
chh	1			
chv	.610	1		
lhh	.783	.523	1	
lhv	.588	.780	.623	1

Table 6.5: Correlation Matrix of four band Principal Component Analysis

The Eigenvectors of Covariance Matrix is in Table 6.6. Unlike the correlation matrix, it is not a subset of the seven band Eigenvectors of Covariance Matrix.

Band	chh	chv	lhh	lhv
1	0.7929	0.16745	0.57087	0.13182
2	-0.57952	-0.07023	0.80863	0.07314
3	-0.18368	0.82241	-0.10792	0.52751
4	0.04157	-0.53914	-0.09265	0.83607

Table 6.6: Eigenvectors of Covariance Matrix for four band Principal Component Analysis

This matrix interestingly weighs the HH components of both frequencies higher than the HV components in the first two principal component bands. The HV components do not receive significant weighting until the third and fourth principal components. This is demonstrated in the images representing the principal components, Figures 40 through 43. The first principal component, Figure 40, looks more like the HH polarized images than the cross polarized images. However, it contains the information from both frequencies. This is most apparent in the representation of

the Navy airfield and the wetland area south of the Portsmouth Coast Guard Facility.

The variances of the pixel data in the transformed coordinate system are presented in the following matrix.

$$\Sigma_y = \begin{matrix} 12449.81 & & & \\ 0 & 1343.45 & & \\ 0 & 0 & 656.28 & \\ 0 & 0 & 0 & 119.48 \end{matrix} \qquad \text{Equation 6.8}$$

This matrix demonstrates that 85.45% of the variance in the data set is in the first principal component, as per Equation 6.7.

The percent variance for each of the principal component bands is listed below in Table 6.7.

Band	% Variance
1	85.45%
2	9.22%
3	4.50%
4	0.82%

Table 6.7: Variances of four band Principal Component Analysis

The principal component images directly reflect these values. Figure 40 has almost all of the visually identifiable information from all of the radar images, however, it is heavily weighted with like polarized information. The one noticeable contribution of the cross

polarizations that is missing is the ability to break out information within the saturated areas of the HH returns. This is most noticeable in the southern tip of the Navy piers and the bright returns on the south side of the Elizabeth River.

The first three principal component bands were combined in a false color red, green, blue image in Figure 44. This figure does an outstanding job of displaying all detail present in the four radar bands, while compressed into three bands of information. This image shows more complete detail than any of the combined false color radar images in Figures 20 through 24. This is most evident in the detail around the piers on the Navy base portrayed in red, and the red returns within yellow areas throughout the entire image. These areas in the combined radar bands were significantly more uniform in color or in many cases saturated white, providing no detail. The ships' wakes in the water also show a significant improvement in detail over any of the combined radar band images.

This principal component analysis succeeded in compressing four bands of data into three while simultaneously gaining more discernible, useful information in the data.

B. NEURAL NETWORK ANALYSIS

Neural network analysis was performed on the data using the Kohonen Self Organizing Map. This is an unsupervised classification process which categorizes the input data into a specified number of categories based on the spectral response of each pixel and the 'neighborhood' surrounding the pixel. The Self Organizing Map learns what the categories are going to be as it processes the data.

1. Background

The process of the Kohonen Self Organizing Map can be subdivided into a training and a classification process. The neural network used in the training process can be visualized as an array of highly interconnected elementary processors, called neurons (See Figure 45). The neurons are organized in a bidimensional array with every neuron connected to the input data (Chiuderi, 1994). In this case, there is a neuron for every pixel in the input image. The neurons have initial weights that are adjusted based upon their processing of the data. Each pixel input into the network is represented by a neuron. One of the categories, called nodes, is declared the 'winner' in the competition to represent the data. This is determined based on the weight values of the neurons. Once the winner has been declared, the neuron weights are updated in the 'neighborhood' of the 'won' neuron. The radius of the neighborhood decreases as

the training process continues. It can be nearly half of all the neurons at the beginning of the process but is reduced to the immediate vicinity of the 'won' neuron as the training process nears its conclusion. The data is run through this training cycle for some preset number of iterations. The optimum number of iterations is a subjective estimate with no empirical relationship existing to define it. (Gautreaux, 1995)

The network of neurons trains itself on the given data to categorize the pixels into the predetermined number of nodes. A classification program is then run to sort the pixels spatially into the categories determined in the training process. It is important to note that a category can be defined by a node during the training process to be a null category; i.e., the neural network may determine that there is not sufficient spectral differentiation in the data to justify a separate category when one does not necessarily exist.

2. Neural Network Results

Six neural network classifications were done in this analysis. In each case, eight categorizing nodes were used with 50,000 training iterations on the input data. Classifications were performed on the following input data sets.

Classification	Input Bands Used
1	C-Band HV, L-Band HV
2	C-Band HH, L-band HH
3	All 4 Radar Bands
4	All 7 Bands (radar & visible)
5	All 7 Principal Component Bands
6	First 3 Principal Components of the 7 Band PCA

Table 6.8: Neural Network Classifications and input bands

The results are presented in Figures 46 through 51. It is clear from inspecting Figures 46 and 47 that a neural network classification based upon the input of only two radar bands does not provide useful information. In figure 46, all null categories are represented in black, with only one category differentiated by the neural network. This category, represented in white, appears to be those areas which had very low return values in the HV images.

The neural network analysis done with the input of the like polarized radar images, Figure 47, resulted in six null categories, represented in white and two classified categories represented in red and blue. The limited number of pixels categorized precludes any worthwhile conclusions from this image.

When all four radar bands were used as input to the Self Organizing Map, four categories were differentiated, while the other four nodes produced null categories. In Figure 48, the null categories are represented in black, the others are represented in red, green, blue, and white.

White appears to represent those areas which were saturated in the like polarized radar images and the blue category appears only in the water areas, yet does not define all water areas. The red and green categories represent pixels in residential areas, land fill areas, the piers of the Navy base, and areas of high return values in all of the radar images. These results allow little confidence in the categorization done by the neural network with the four radar bands as input.

Figure 49 represents the classification of the neural network with all four radar bands and the three visible bands as input. In this image the eight nodes produced three null categories, represented in black and five recognizable categories, represented in red, green, blue, yellow, and white. Again, the white category appears to represent those features which have very strong returns in the like polarized radar imagery. This includes the southern tip of the Navy base, some of the residential areas, and what could be ships at pierside. Blue represents some of the land fill area, the land surrounding the Navy airfield, and what is known to be a cloud in the visible images. Yellow and green appear only in areas known to be water, yet do not relate to any recognizable features in the original images. The red category ambiguously represents pixels in the land fill area, in the water, in residential areas, and along some roads as well.

The neural network run on the seven principal component bands resulted in four null categories, represented in black and four classified categories, represented in red, green, yellow, and white. These results are displayed in Figure 50. Once again, white appears to represent a portion of those areas which had very nearly saturated returns in the like polarized radar imagery. Green and yellow are mixed thoroughly together throughout the residential areas of the image. The red category represents most of the land fill area, some shorelines, many places within the residential areas, and an extensive area on the Navy base including the airfield area.

Finally, Figure 51 displays the results from the neural network analysis using principal components one, two, and three as inputs from the seven band principal component analysis. Four null categories were classified as well as four categories displayed in red, yellow, green, and white. The white pixels represent the returns that were saturated in the like polarized images, but in this case they are more clearly broken apart from neighboring pixels. The red category appears to represent much of the coastline in the image and also some land fill area as well as the area surrounding the airfield. Yellow and green pixels in this classification do not appear to represent any unique features. Most of these pixels are in the water areas, yet some are in the residential areas as well.

A summary of the results of the six neural network analyses are presented in the following table.

Input Bands Used	Number of null categories	Number of classified categories
C-Band HV, L-Band HV	7	1
C-Band HH, L-band HH	6	2
All 4 Radar Bands	4	4
All 7 Bands (radar & visible)	3	5
All 7 Principal Component Bands	4	4
First 3 Principal Components of the 7 Band PCA	4	4

Table 6.9: Categorization results of neural network classifiers

This neural network analysis has demonstrated that the number of categories defined by the process is highest when the four radar bands and three visible bands are used as input. However, it is not clear in the output images that each of the categories consistently represents the same type of surface feature. Further study of smaller, known data sets is required to understand the categorization performed by the nodes within this Kohonen Self Organizing Map.

VII. SUMMARY

This thesis study successfully explored the process of digitally merging synthetic aperture radar data with visible imagery. The visible and radar data analyzed were received from co-located sensors on the Space Shuttle during the STS-68 SIR-C/X-SAR mission of Endeavour in October, 1994. The radar data were excellent, including C and L band frequencies and like and cross polarized returns from horizontally transmitted electromagnetic waves. The visible data used were less than adequate for outstanding results. The initial pixel resolution of approximately 37 meters was significantly larger than the 25 meter resolution of the SAR data. This resulted in a significant loss of detail and information when the visible image was warped and georegistered to the radar data. The initial goal of acquiring radar and visible data co-located in time and space proved impossible. The two images used in the study were separated in time by a period of 7 hours and 45 minutes. Ideally, future studies will contain visible and radar data coincident in both time and space with identical digital resolution.

In the radar data alone, several noteworthy differences between frequencies and polarizations were observed. The most tactically significant differences were the ability to see ships' wakes only in like polarized images, the ability to see an airfield only in C band frequencies, and the

ability to see detail within a particular wetland area only in the L band images.

The combination of radar frequencies and polarizations in false color composite images succeeded in representing most of the features of each of the individual bands in one image. Figure 20 illustrates this feat by clearly showing the airfield and the wetland area, yet the image does not clearly illustrate the ships' wakes.

The combination of the blue visible band to combined false color composite images succeeded in adding color and tone variation to the combined radar images. This is especially evident in Figures 27 through 29 in the water and residential portions of the image. More ground truth is required to understand the contributions of the tonal variation in the image.

The reorganization of the data into principal component bands was most successful when using only the four radar bands as input. The combined false color composite image of the first three principal components illustrated in Figure 44 has the best detail resolution of any image in the entire analysis. This is most evident in the red returns within areas that were saturated in many of the other images and in the representation of the ships' wakes. This principal component analysis succeeded in compressing four bands of information into three bands while retaining all useful information and improving detail resolution.

Results of the unsupervised classification attempt using neural networks provided limited useful results. In

each of six separate analyses, classification resulted in several null and ambiguous categories. Although one category repeatedly represented what could be ships at pierside, this categorization was performed better in the principal component analysis of radar imagery. Further investigation of the neural network algorithm combined with some supervised classification may improve these results in the future.

VIII. CONCLUSION

Multi-frequency, multi-polarization synthetic aperture radar data from the SIR-C/X-SAR Space Shuttle mission of October, 1994 were successfully fused with visible imagery from the same mission. Merged SAR and visible images of the Norfolk Navy Base in Norfolk, Virginia were analyzed by combining different bands from the different spectra in false color composite images and by performing Principal Component Analysis. Several combinations of the different radar frequencies and polarizations, with and without visible data, demonstrated that fused data sets from different parts of the electromagnetic spectrum can increase the useful information content in an image. Principal Component Analysis was performed using two different data sets. Excellent data reduction and feature enhancement results were obtained when using only radar bands as input. Results were interesting yet ambiguous when combined radar and visible data were used as input. Attempts at unsupervised classification using neural network analysis were not successful. Further effort is required in refining the neural network classification algorithm, possibly incorporating supervised classification methods.

A link between the indexing databases of visible imagery at Johnson Spaceflight Center and synthetic aperture radar data at JPL would allow for greater optimization of SIR-C data and permit more thorough spectral analysis of the earth's surface.

APPENDIX: FIGURES AND IMAGES

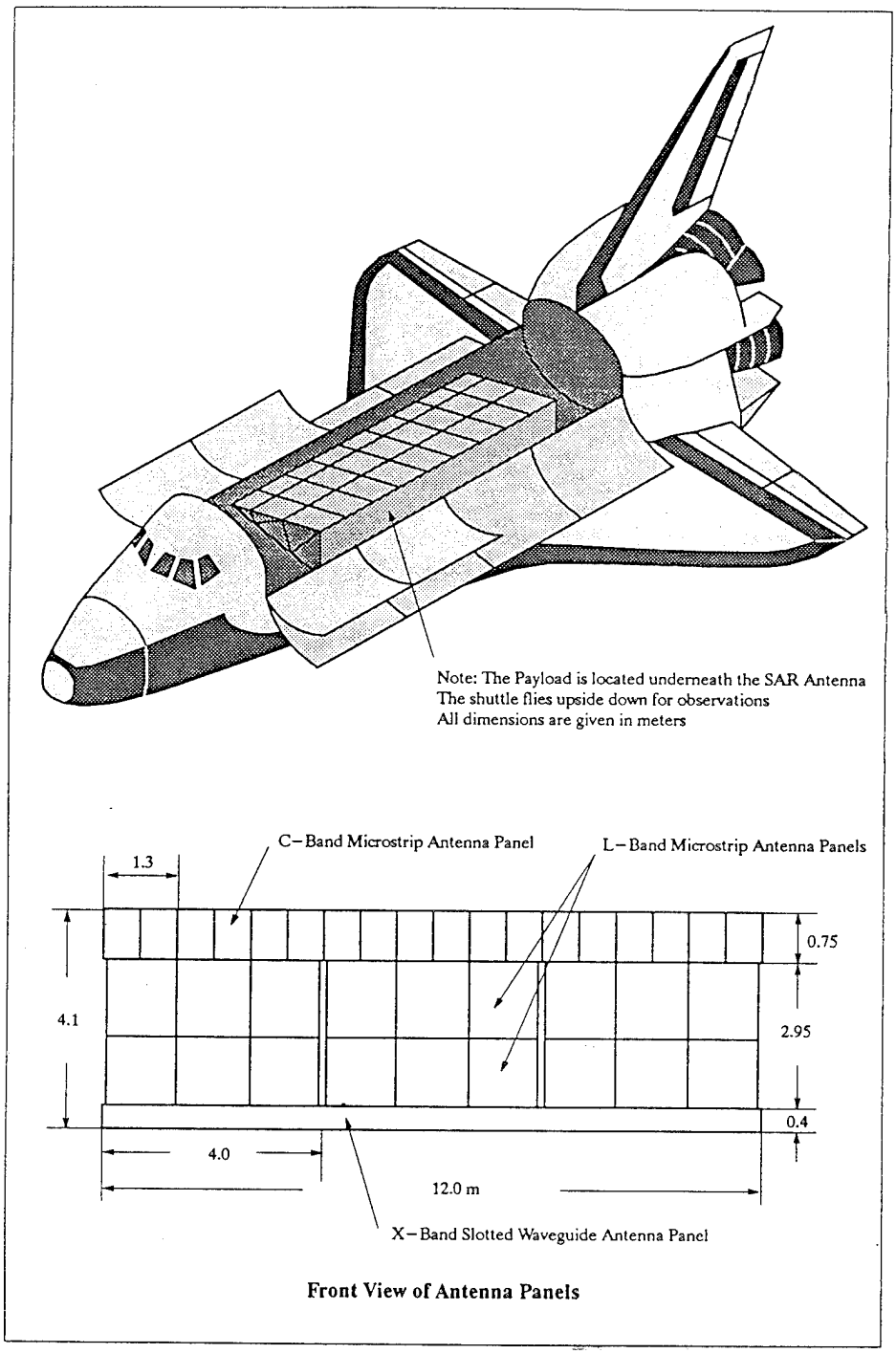

Figure 1: From Kramer [1993], SIR-C/X-SAR synthetic aperture radar in the payload bay of the Space Shuttle

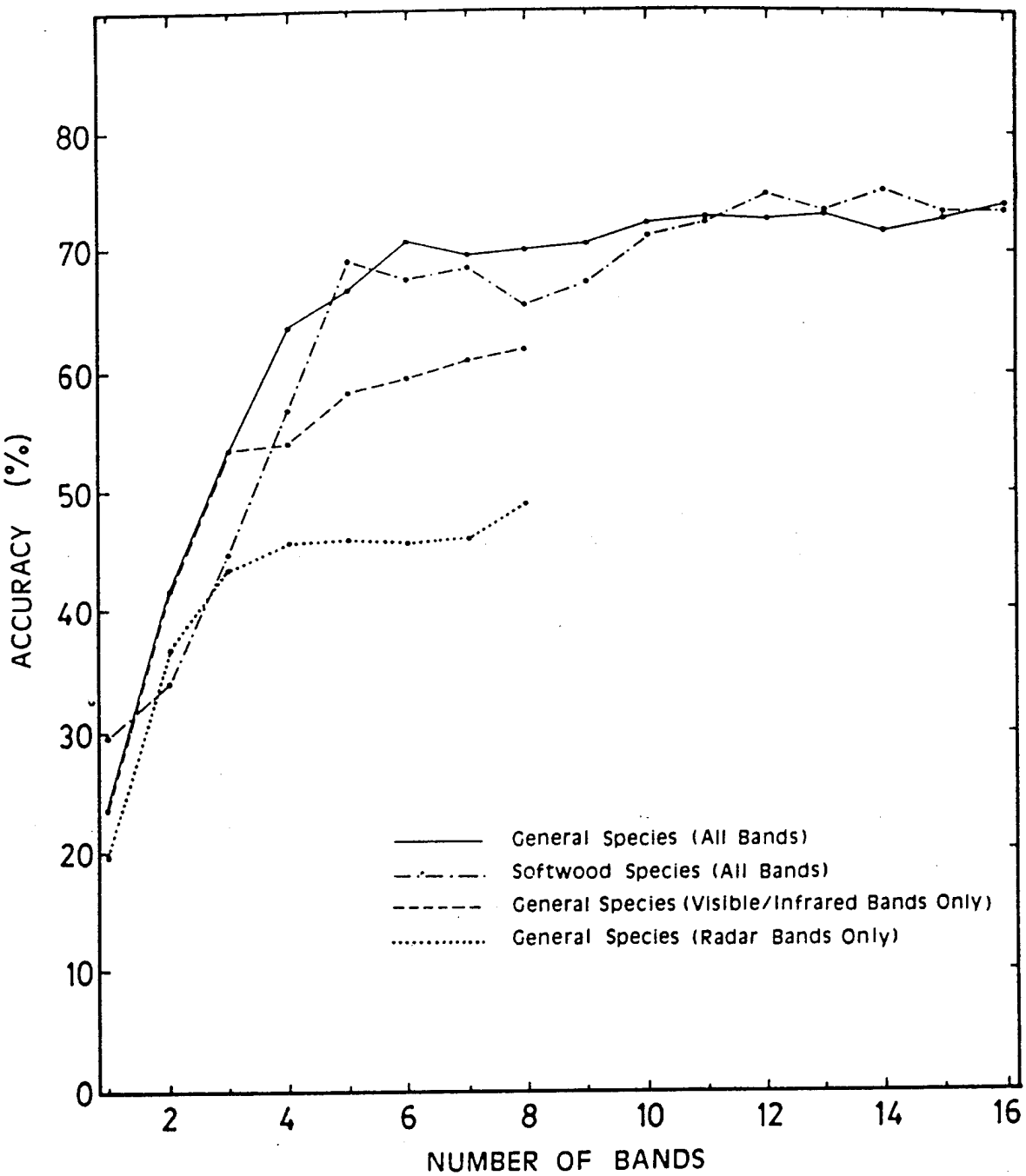

Figure 2: From Leckie [1990], Results of forest type classification using several combinations of C and X band airborne SAR, and visible and IR wavelengths from an airborne multi-spectral scanner

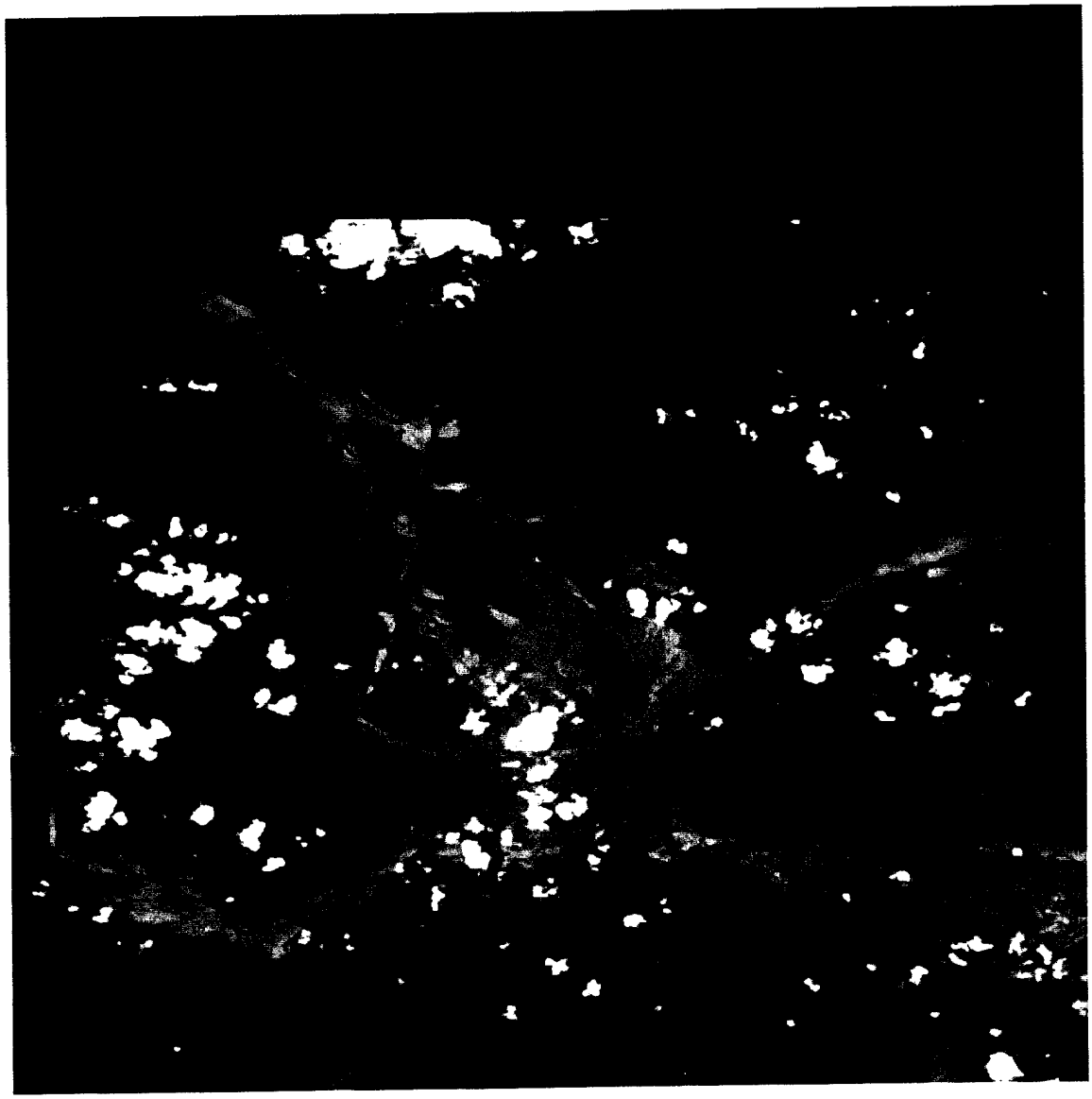

Figure 3: Digitized medium format photograph of Mount Pinatubo, Philippines taken from STS-59, April, 1994

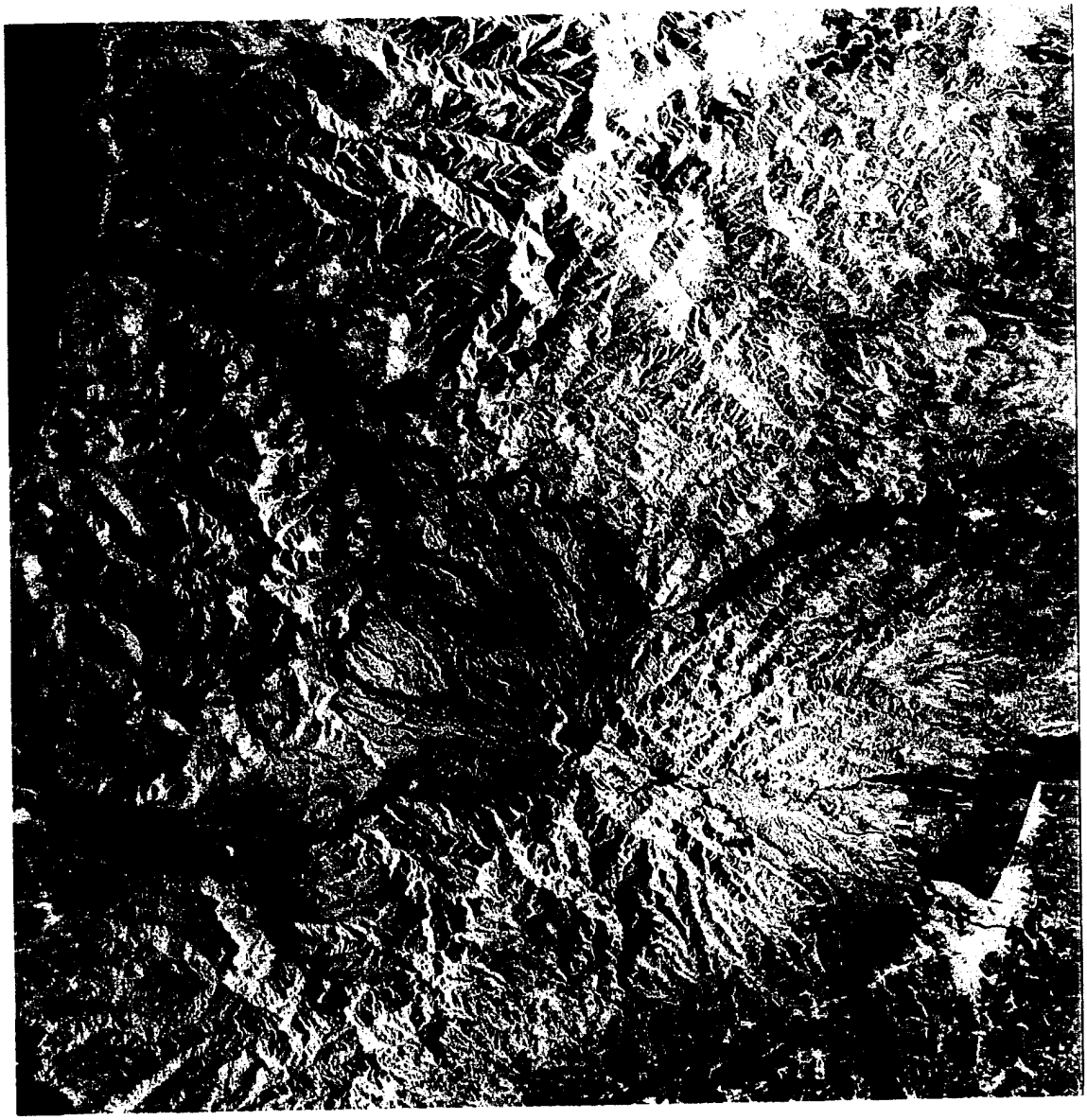

Figure 4: False color composite of SIR-C radar image of Mount Pinatubo, Philippines taken from STS-59, April 1994. L-band HH is red, L-band HV is green, C-band HV is blue.

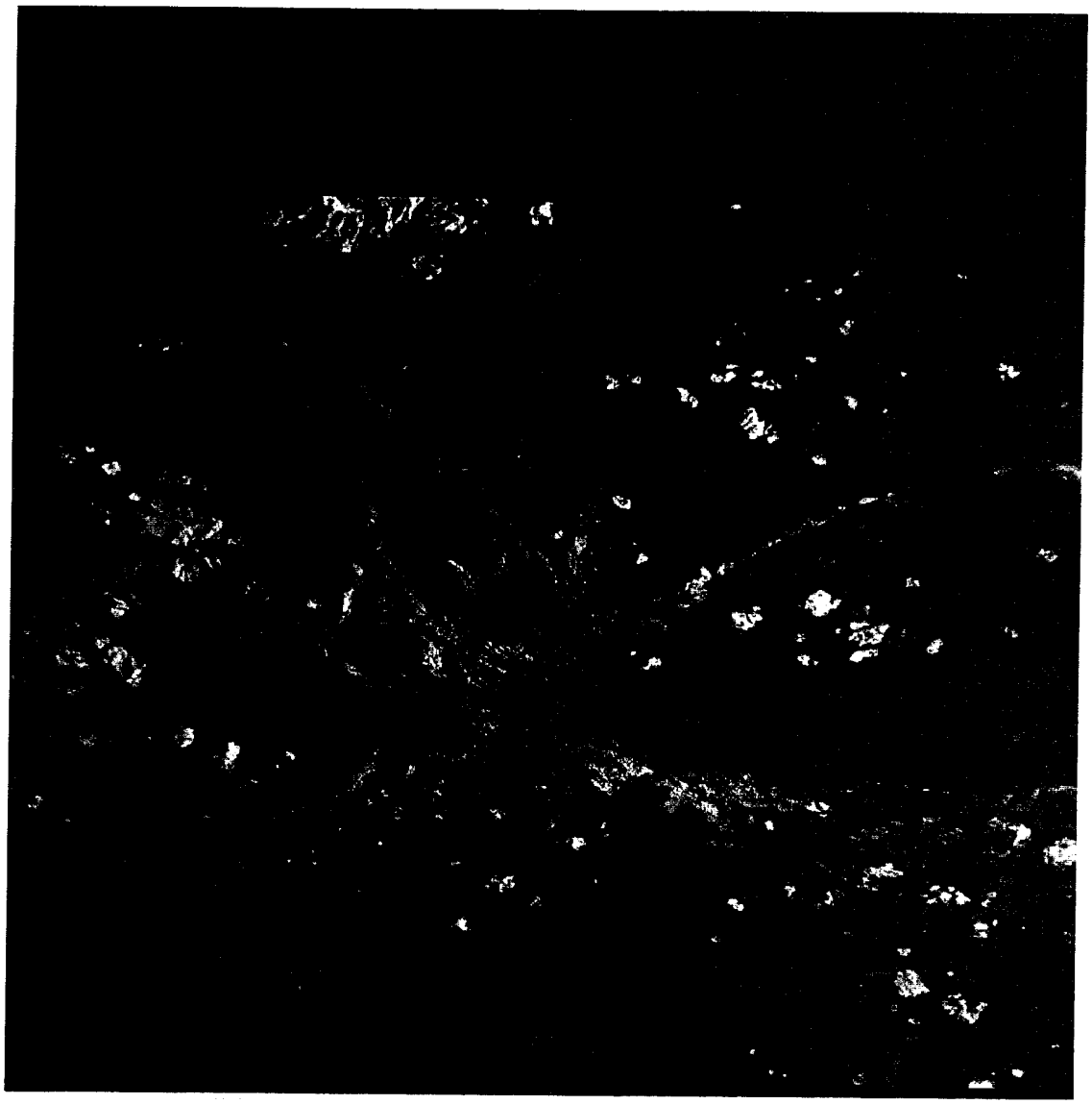

Figure 5: Digitally combined false color image of radar and visible wavelengths of Mount Pinatubo, Philippines taken from STS-59, April 1994. L-band HH is red, C-band HV is green, the blue band of the visible image is blue.

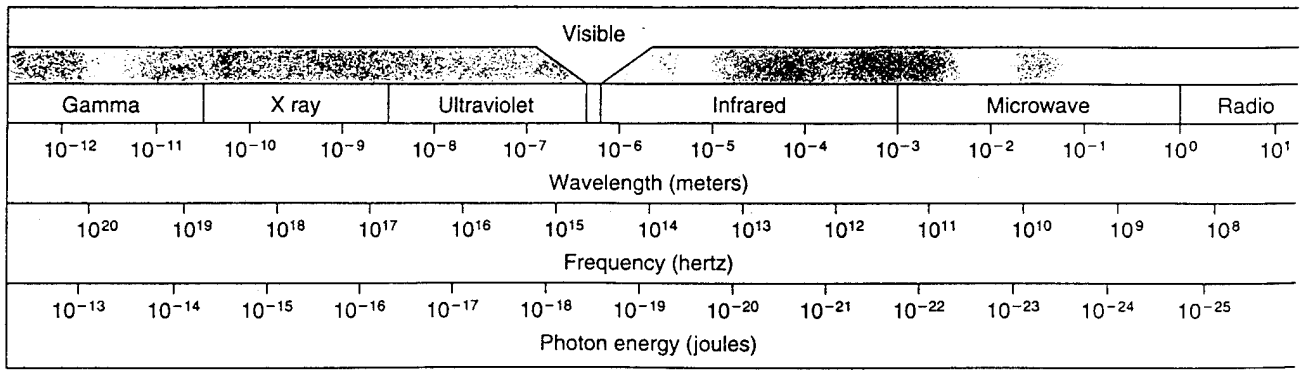

Figure 6: From Avery and Berlin [1985], The electromagnetic spectrum illustrates the difference between microwave and visible wavelengths

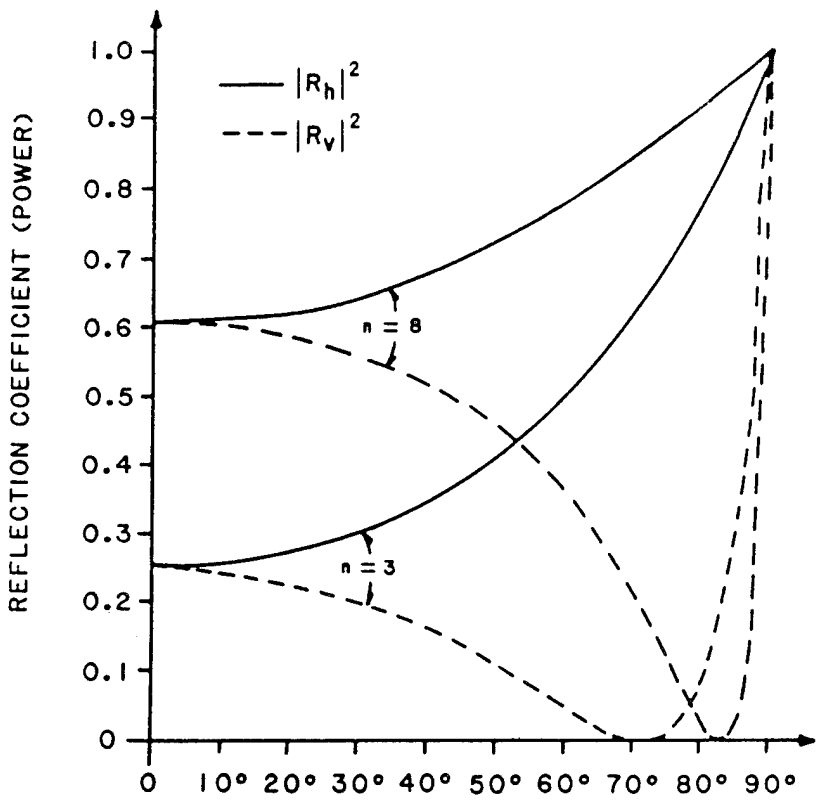

Figure 7: From Elachi [1987], Reflection coefficient as a function of incidence angle for two materials of different indices of refraction. The dashed curve corresponds to vertical polarization, the solid curve corresponds to horizontal polarization.

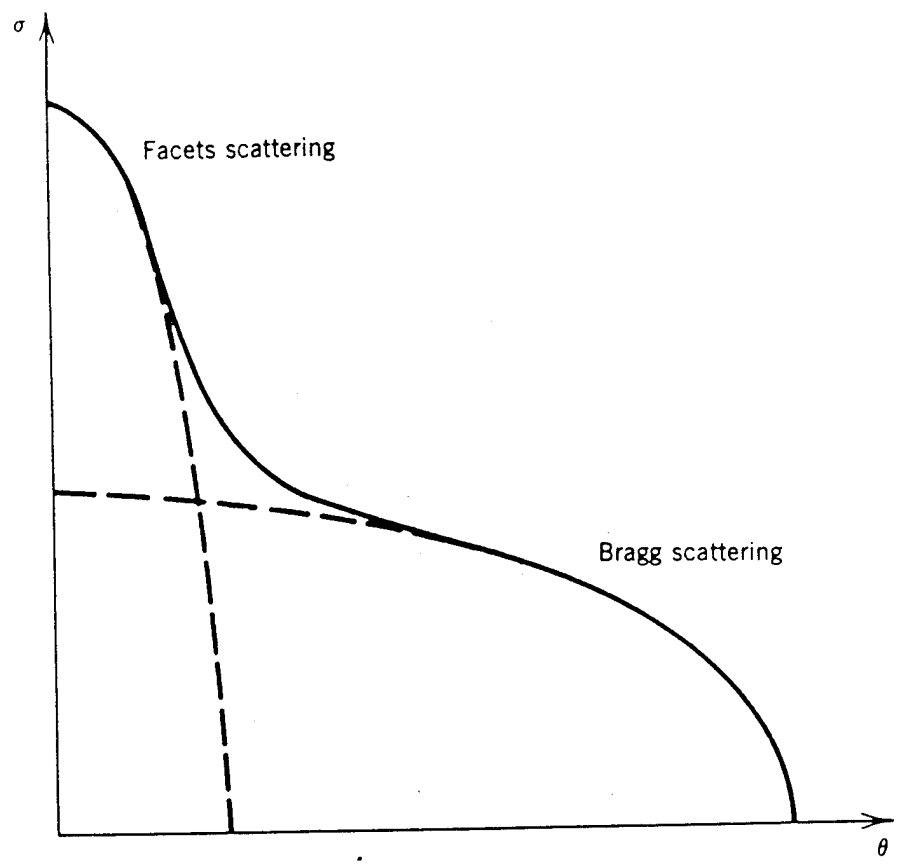

Figure 8: From Elachi [1987], Facet and Bragg scattering as a function of incidence angle.

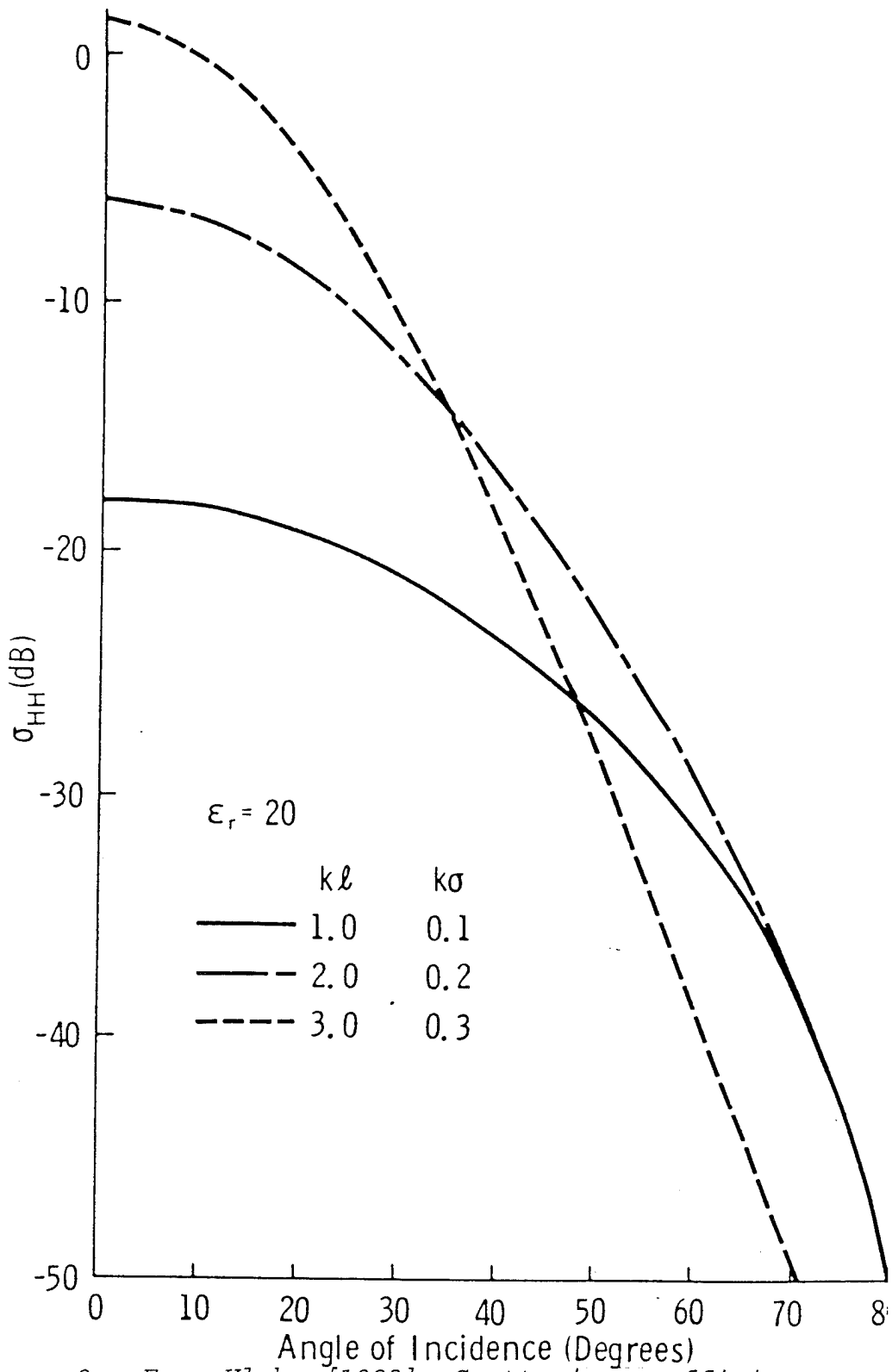

Figure 9: From Ulaby [1983], Scattering coefficient as a function of angle of incidence for a horizontally polarized wave on a slightly rough surface. The three lines represent different sizes of roughness measurements (1).

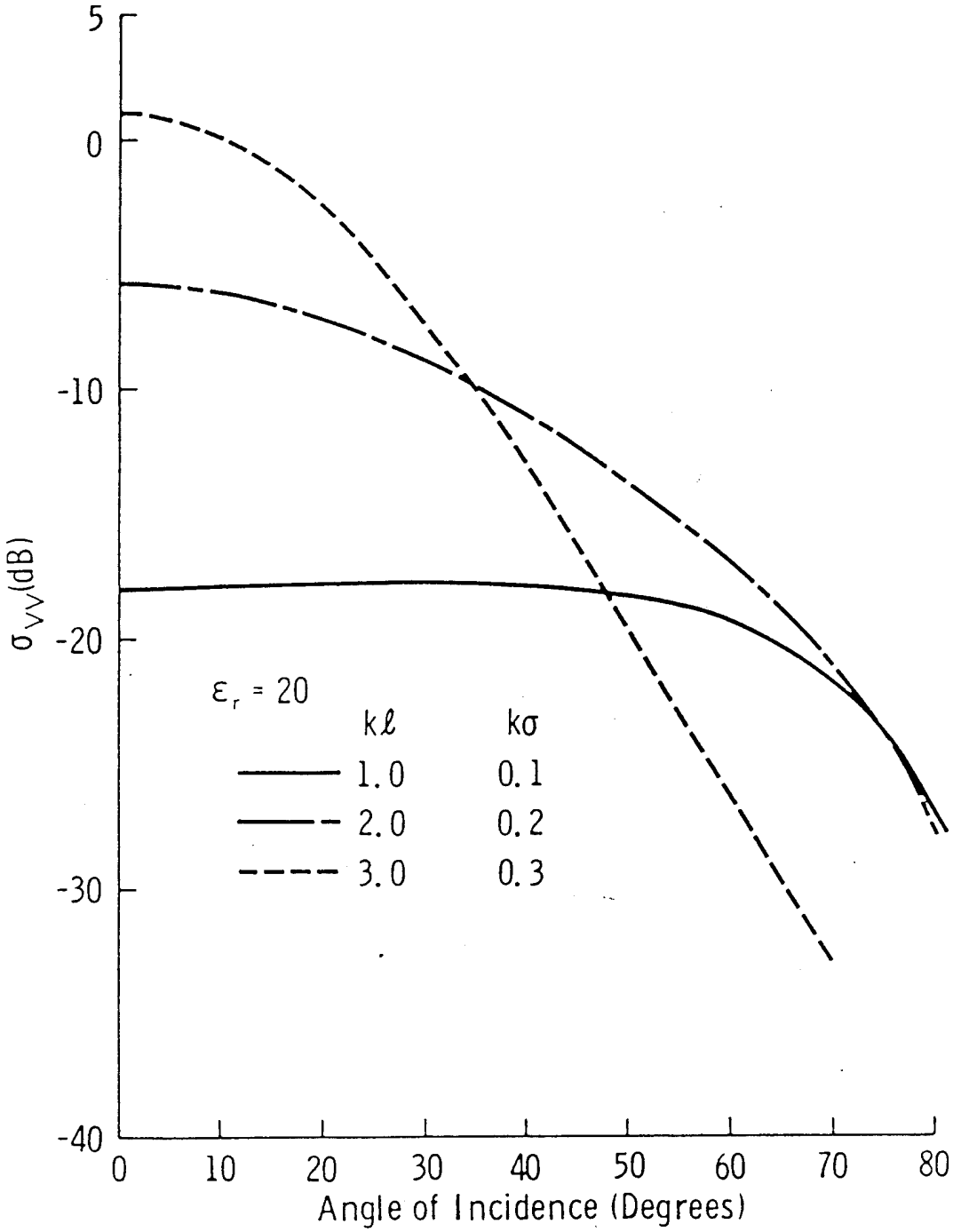

Figure 10: From Ulaby [1983], Scattering coefficient as a function of angle of incidence for a vertically polarized wave on a slightly rough surface. The three lines represent different sizes of roughness measurements (l).

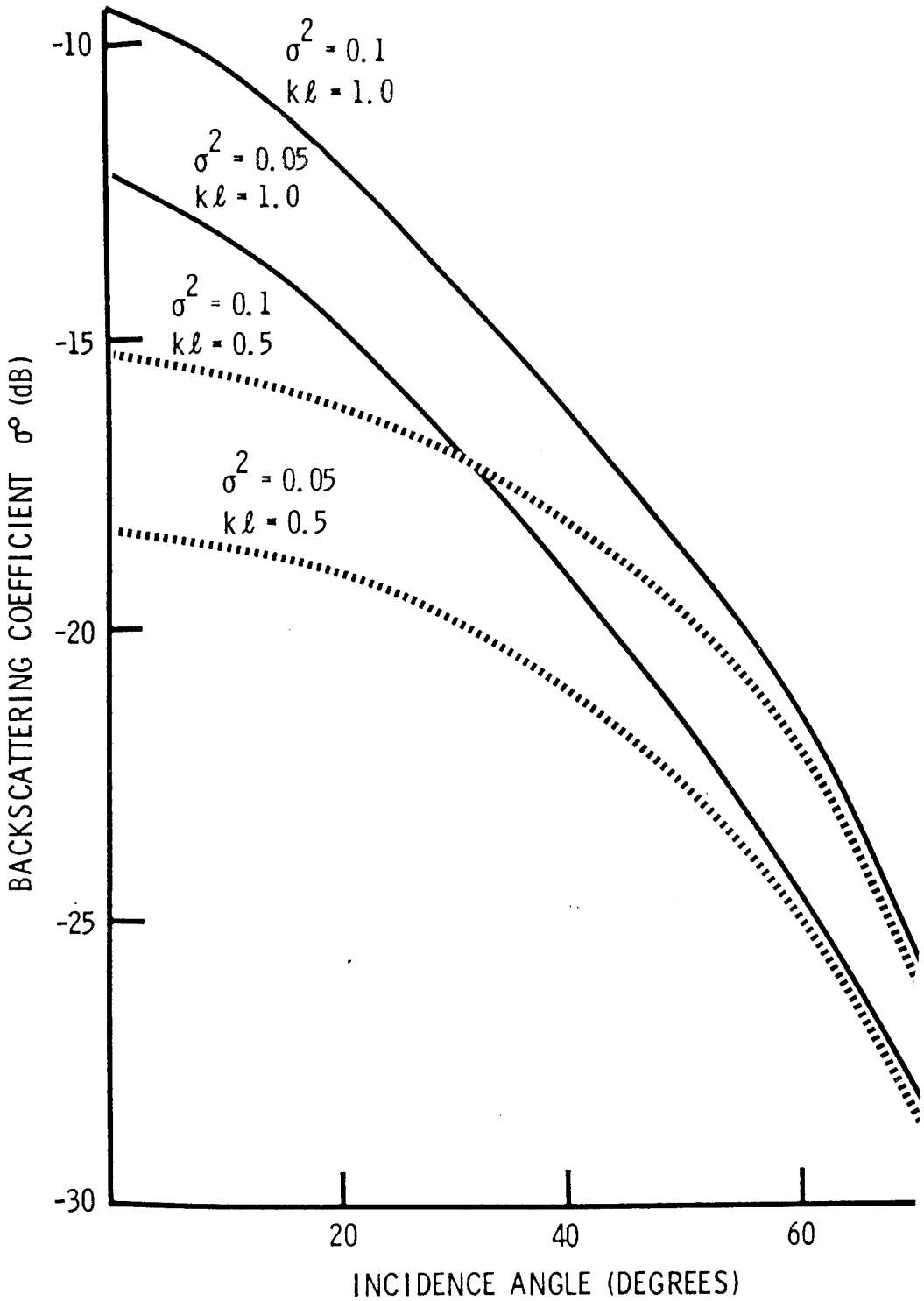

Figure 11: From Ulaby [1983], Radar backscatter coefficient as a function of angle of incidence illustrates volume scattering for different mediums. σ^2 represents the height variance of the medium, kl represents the permittivity

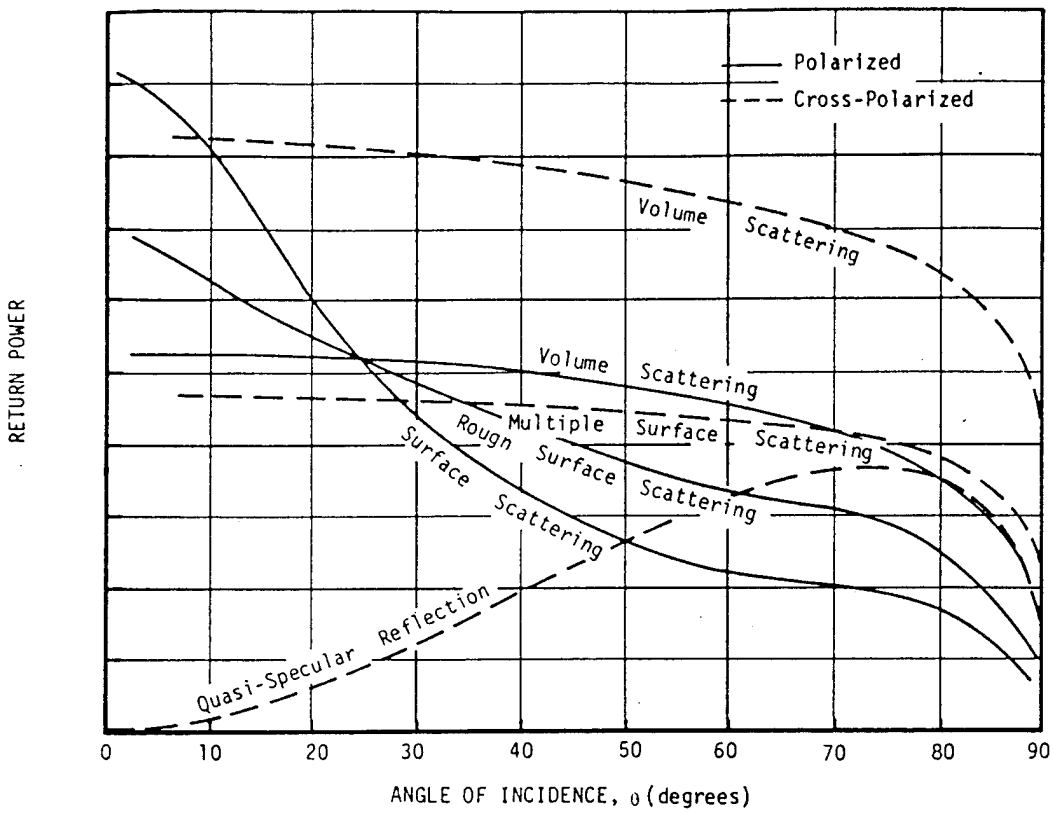

Figure 12: From Ulaby [1983], Return power as a function of angle of incidence for several like polarized and cross polarized conditions

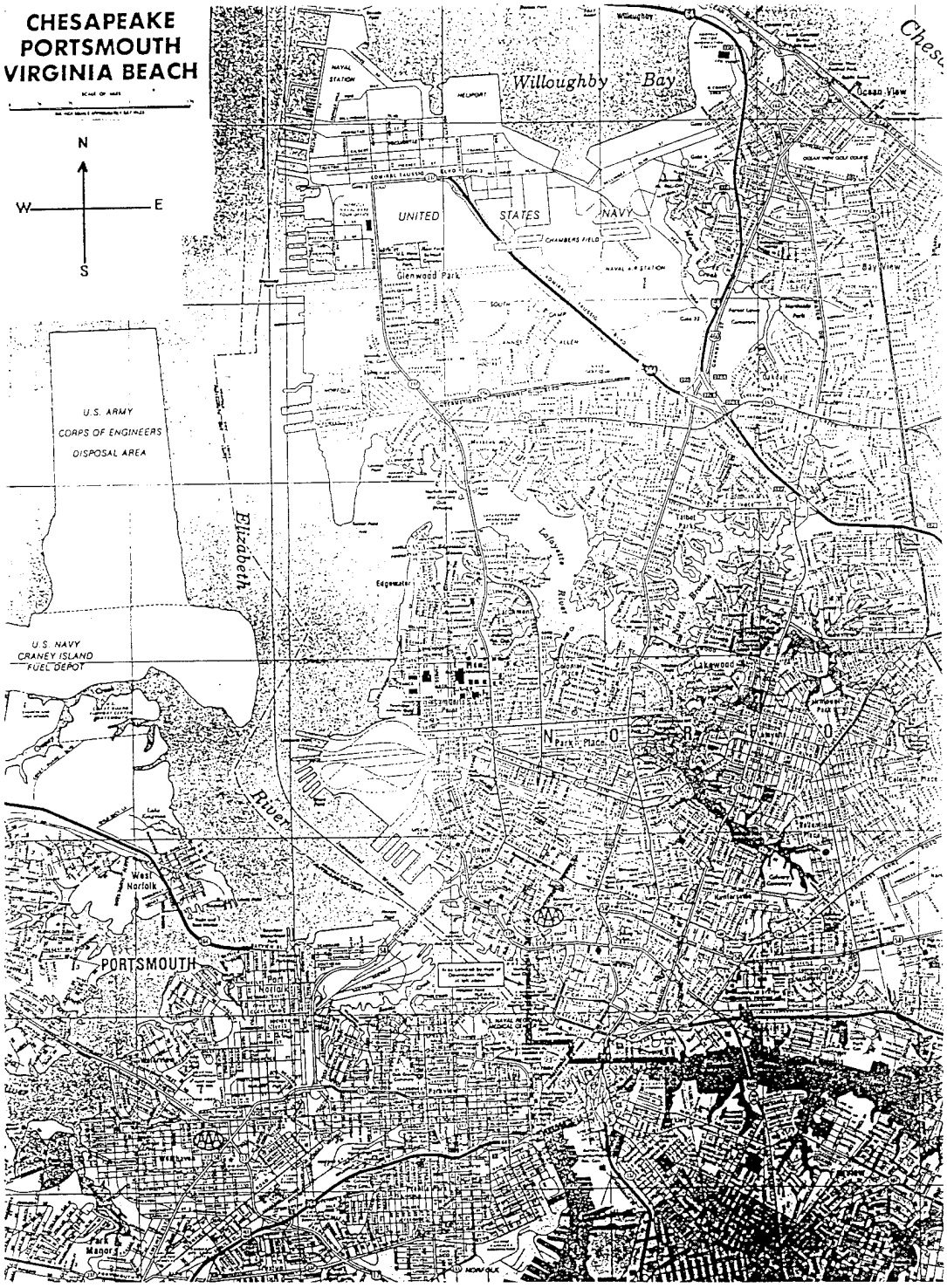

Figure 13: Map of the Norfolk, Virginia region. North is up. The James River is at the NW corner of this map, the Chesapeake Bay at the NE corner. The Portsmouth Coast Guard Facility is just south of Craney Island Fuel Depot.

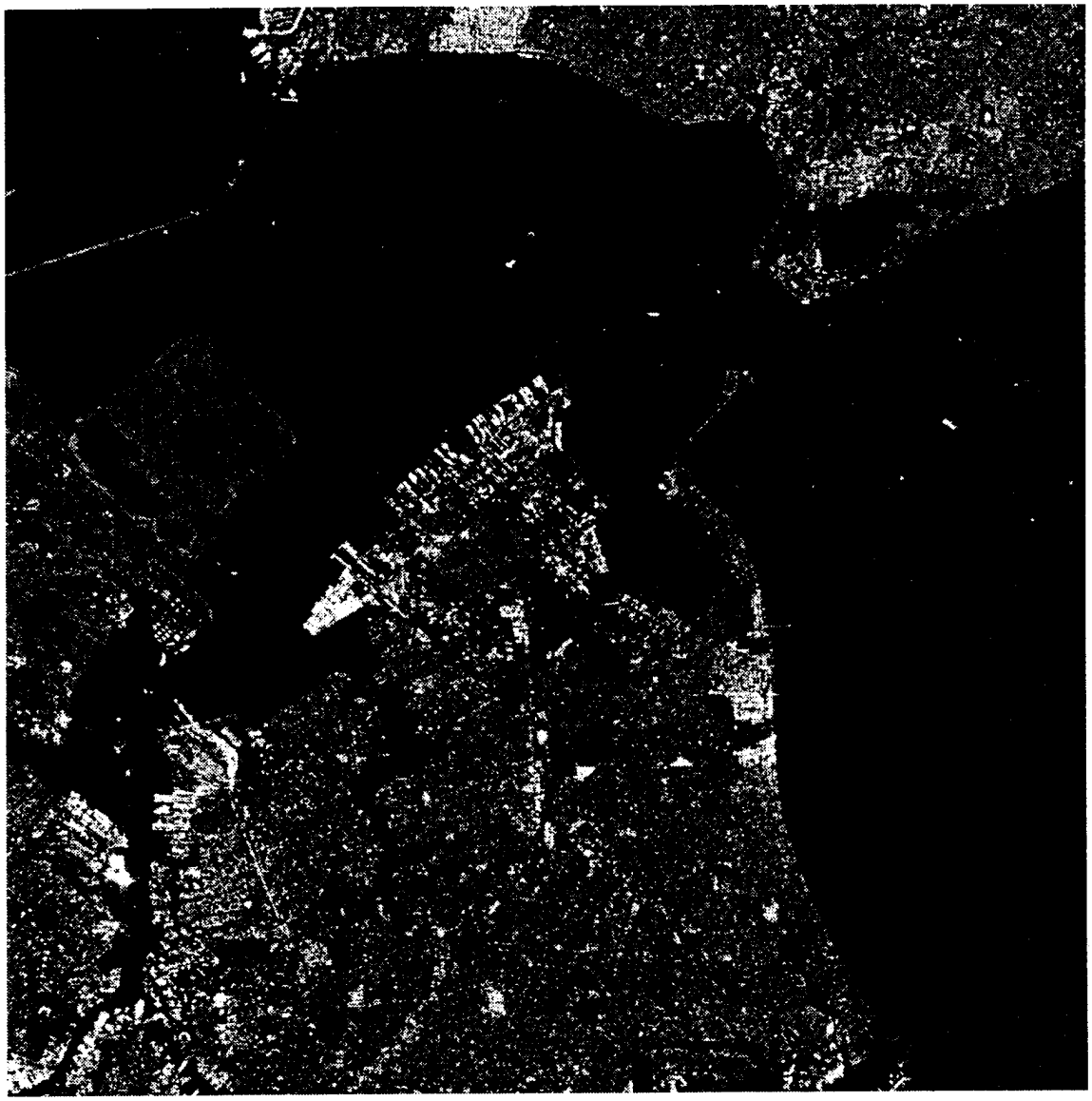

Figure 14: C-band HH polarization image of Norfolk, Virginia. Taken by the SIR-C Synthetic Aperture Radar on Space Shuttle mission STS-68 in October of 1994

Figure 15: C-band HV polarization image of Norfolk, Virginia. Taken by the SIR-C Synthetic Aperture Radar on Space Shuttle mission STS-68 in October of 1994

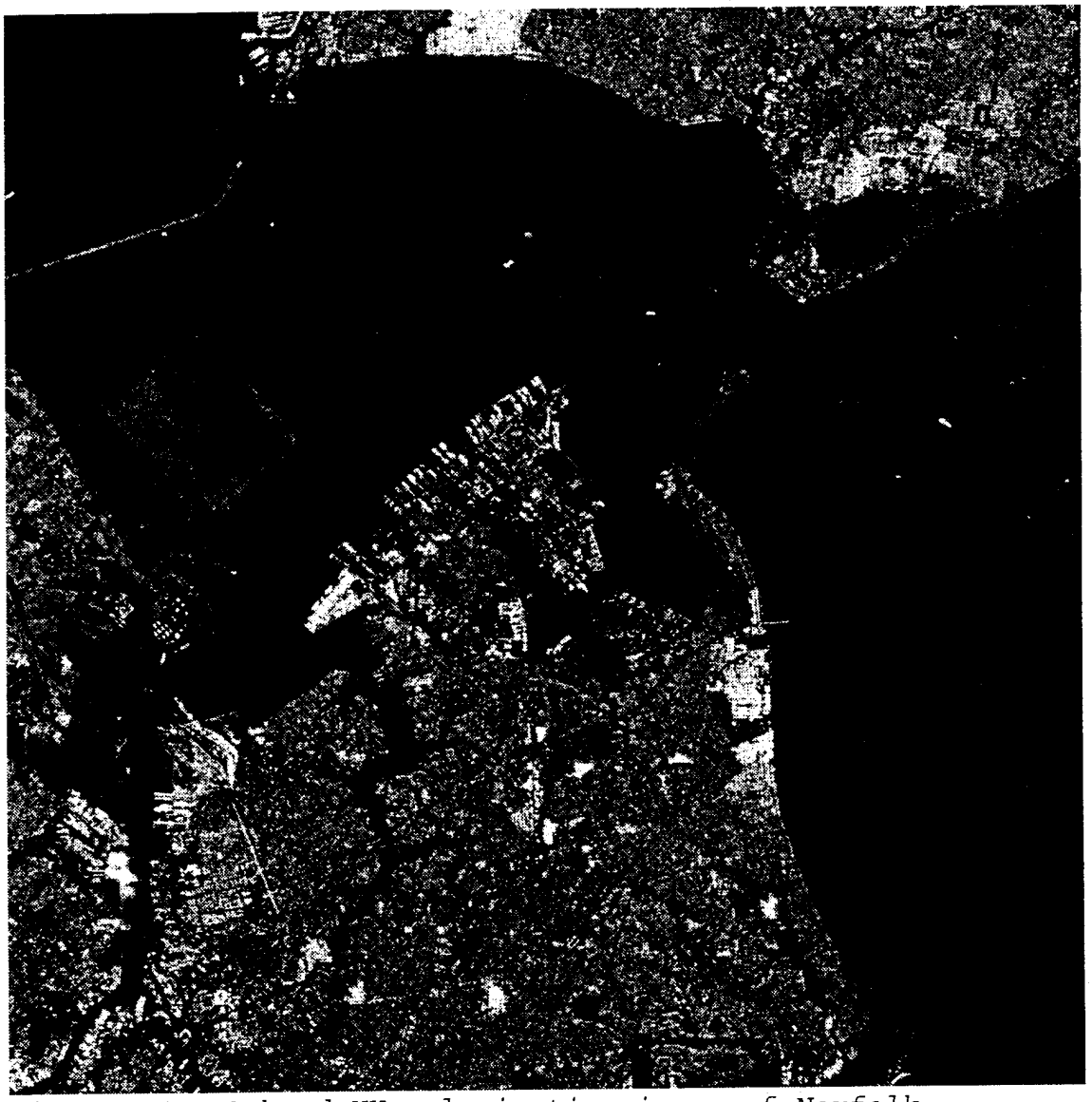

Figure 16: L-band HH polarization image of Norfolk, Virginia. Taken by the SIR-C Synthetic Aperture Radar on Space Shuttle mission STS-68 in October of 1994

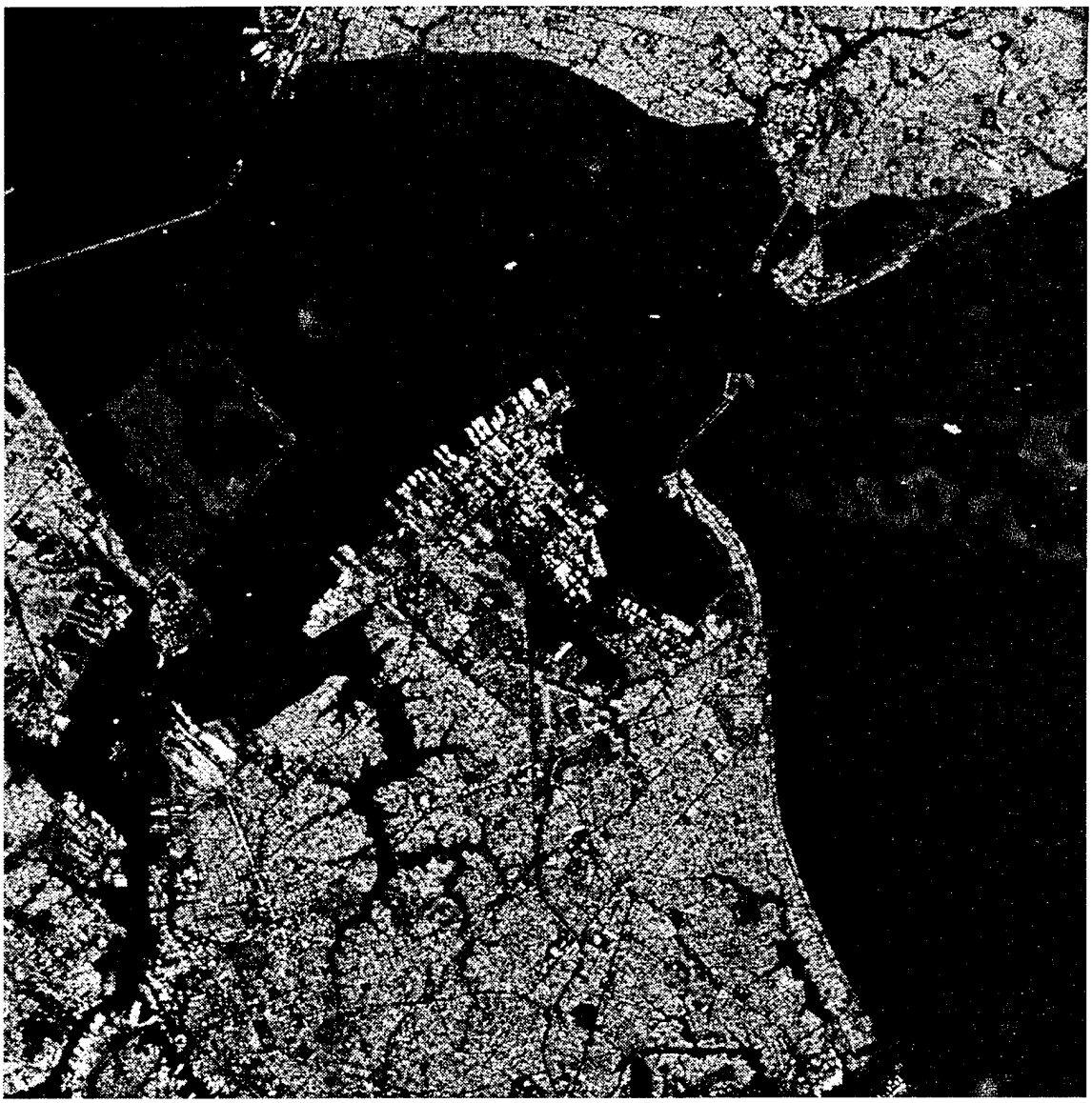

Figure 17: L-band HV polarization image of Norfolk, Virginia. Taken by the SIR-C Synthetic Aperture Radar on Space Shuttle mission STS-68 in October of 1994

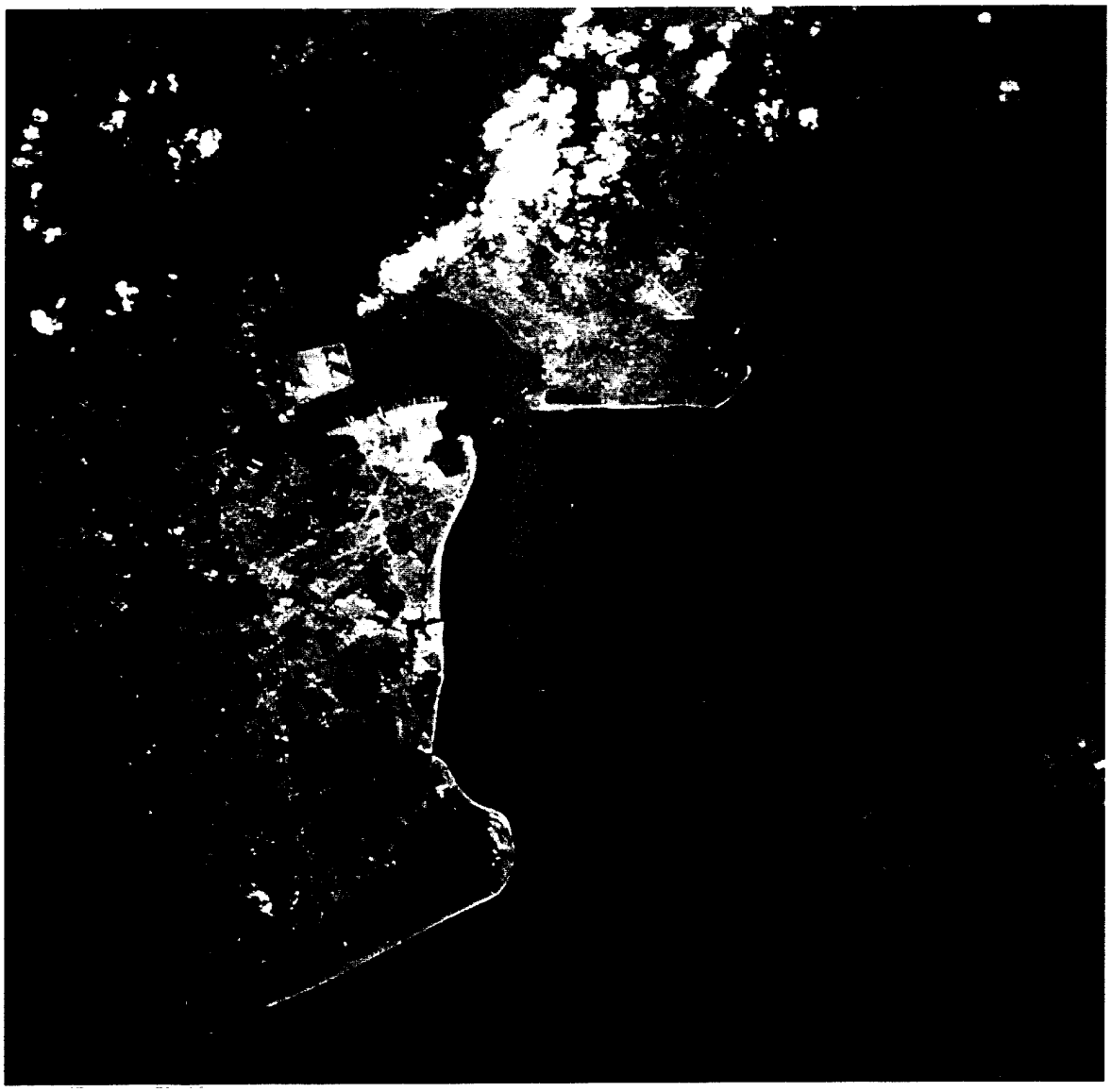

Figure 18: Digitized medium format visible image of Norfolk, Virginia taken from Space Shuttle mission STS-68 in October of 1994

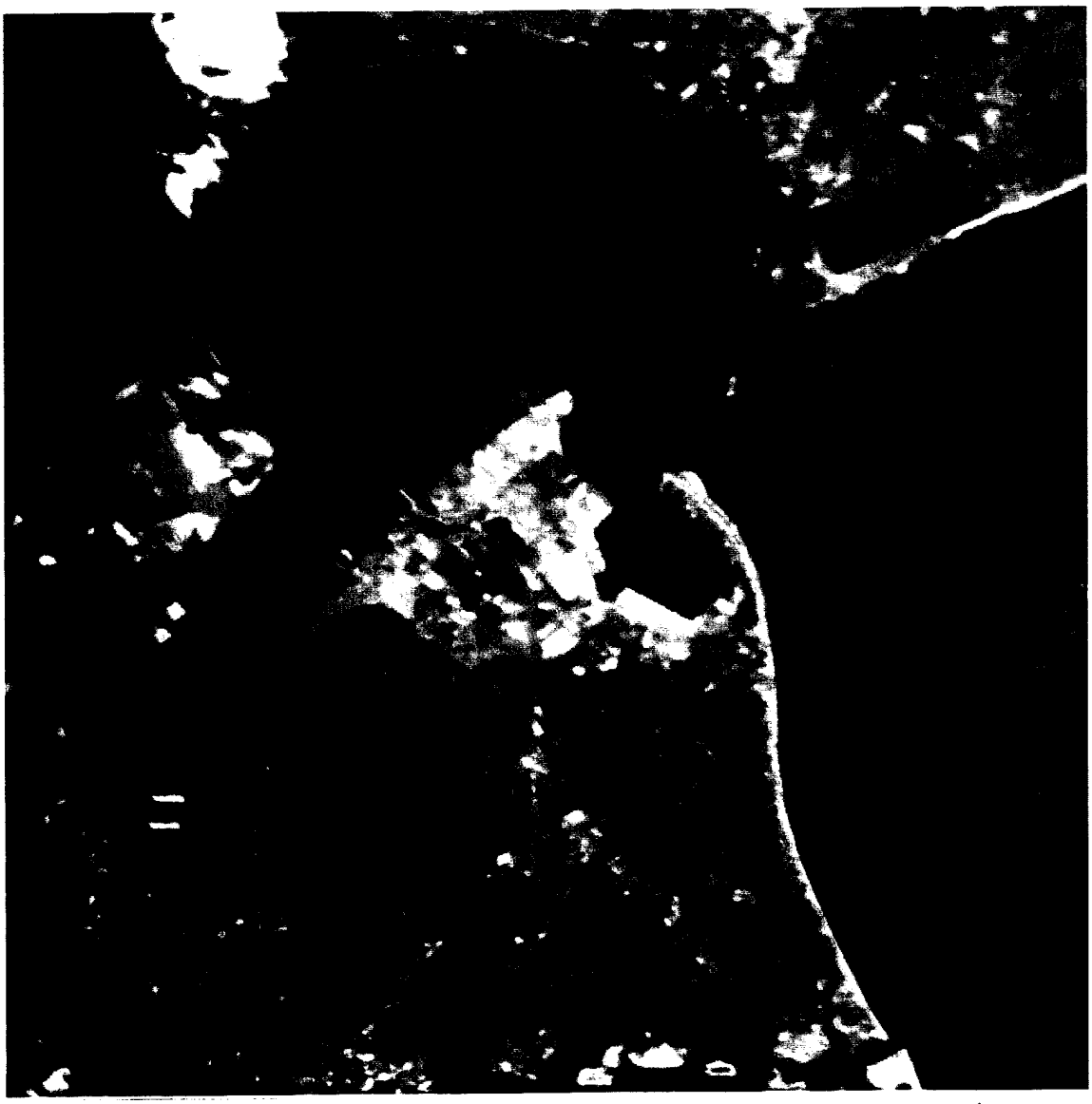

Figure 19: Warped medium format visible image from Figure 18 after geo-registration to radar image

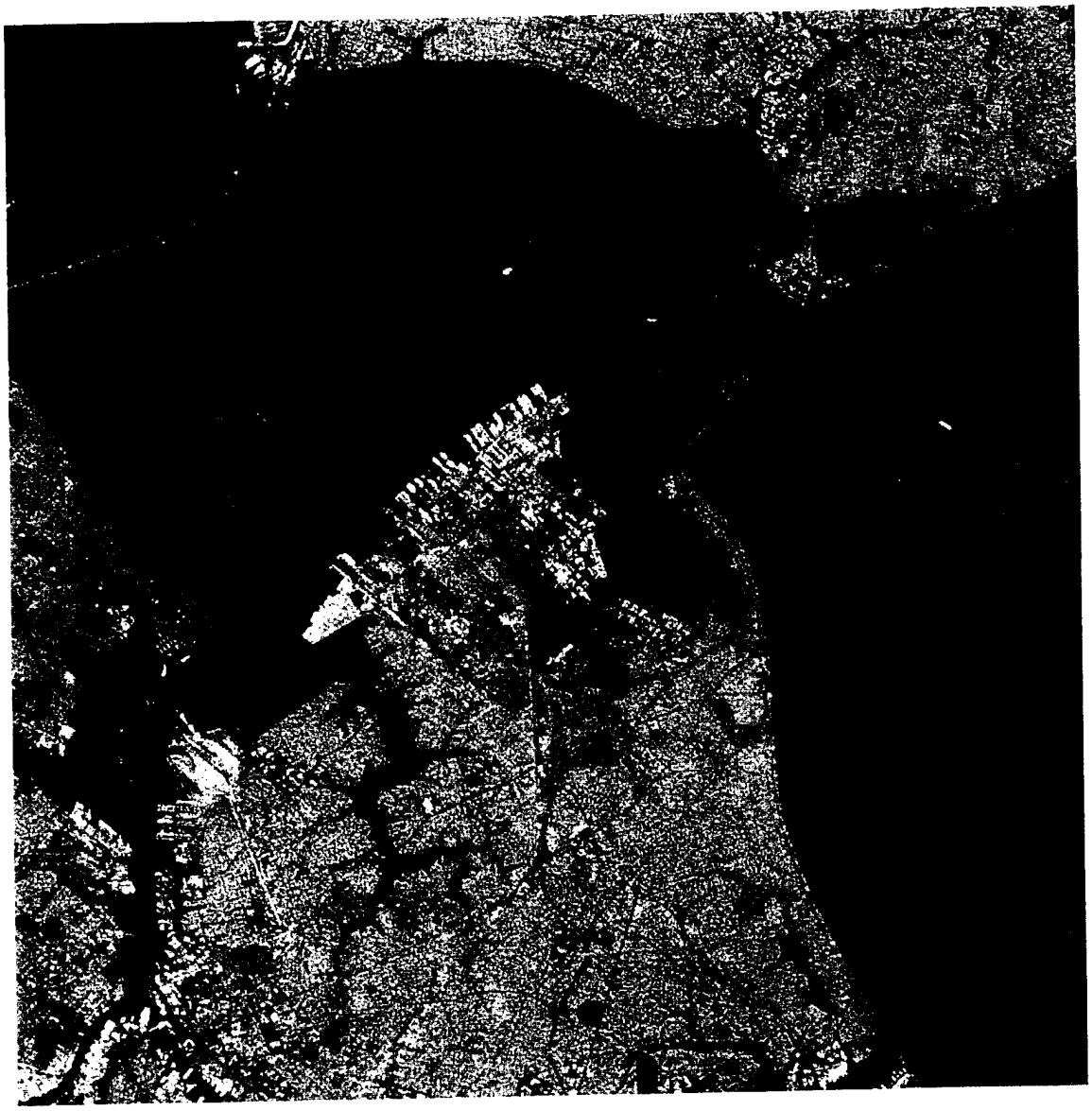

Figure 20: False color composite of SIR-C radar image of Norfolk, Virginia taken from Space Shuttle mission STS-68 in October, 1994. C-band HH polarization is red, C-band HV polarization is green, L-band HV polarization is blue

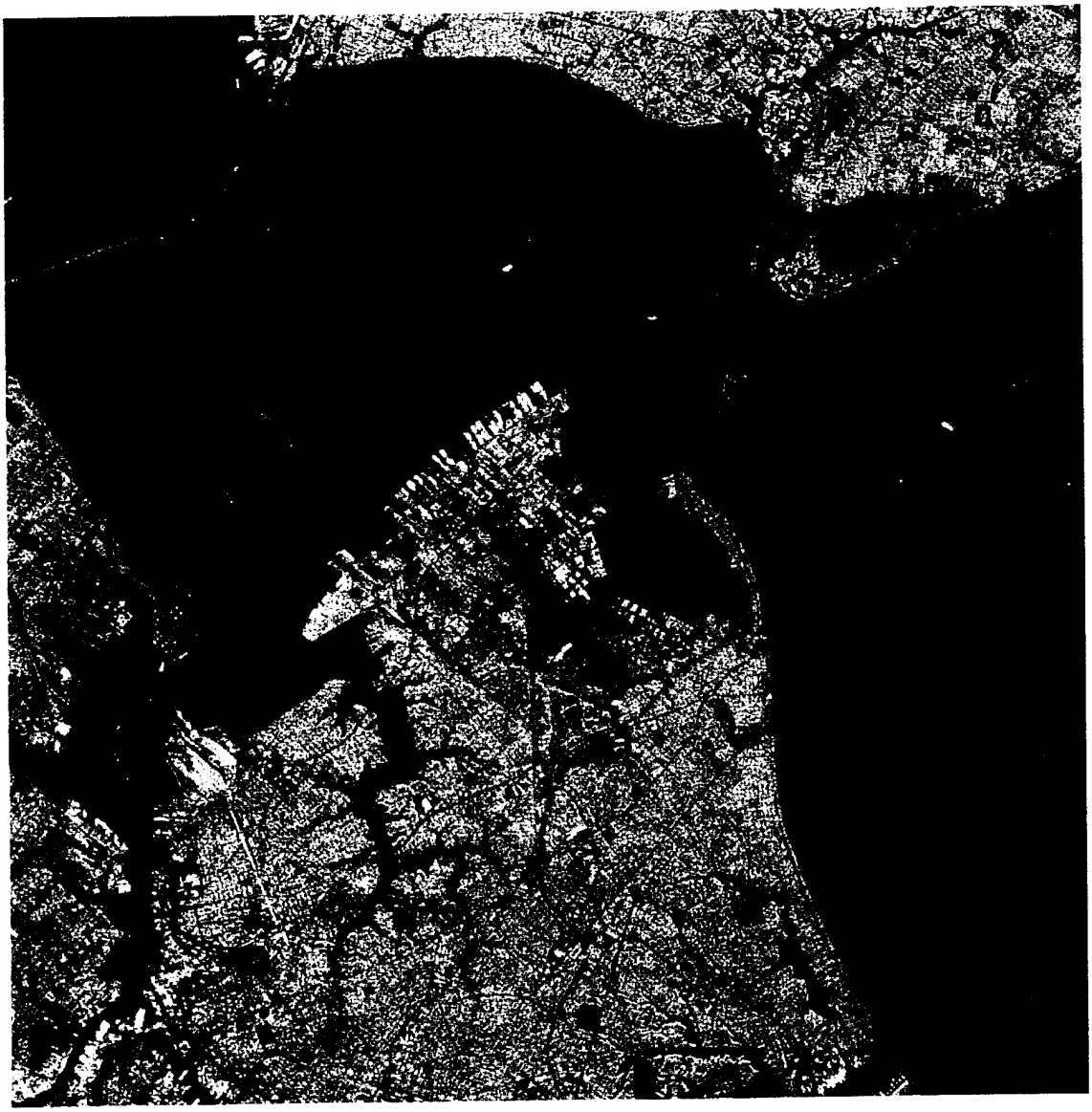

Figure 21: False color composite of SIR-C radar image of Norfolk, Virginia taken from Space Shuttle mission STS-68 in October, 1994. L-band HH polarization is red, L-band HV polarization is green, C-band HH polarization is blue

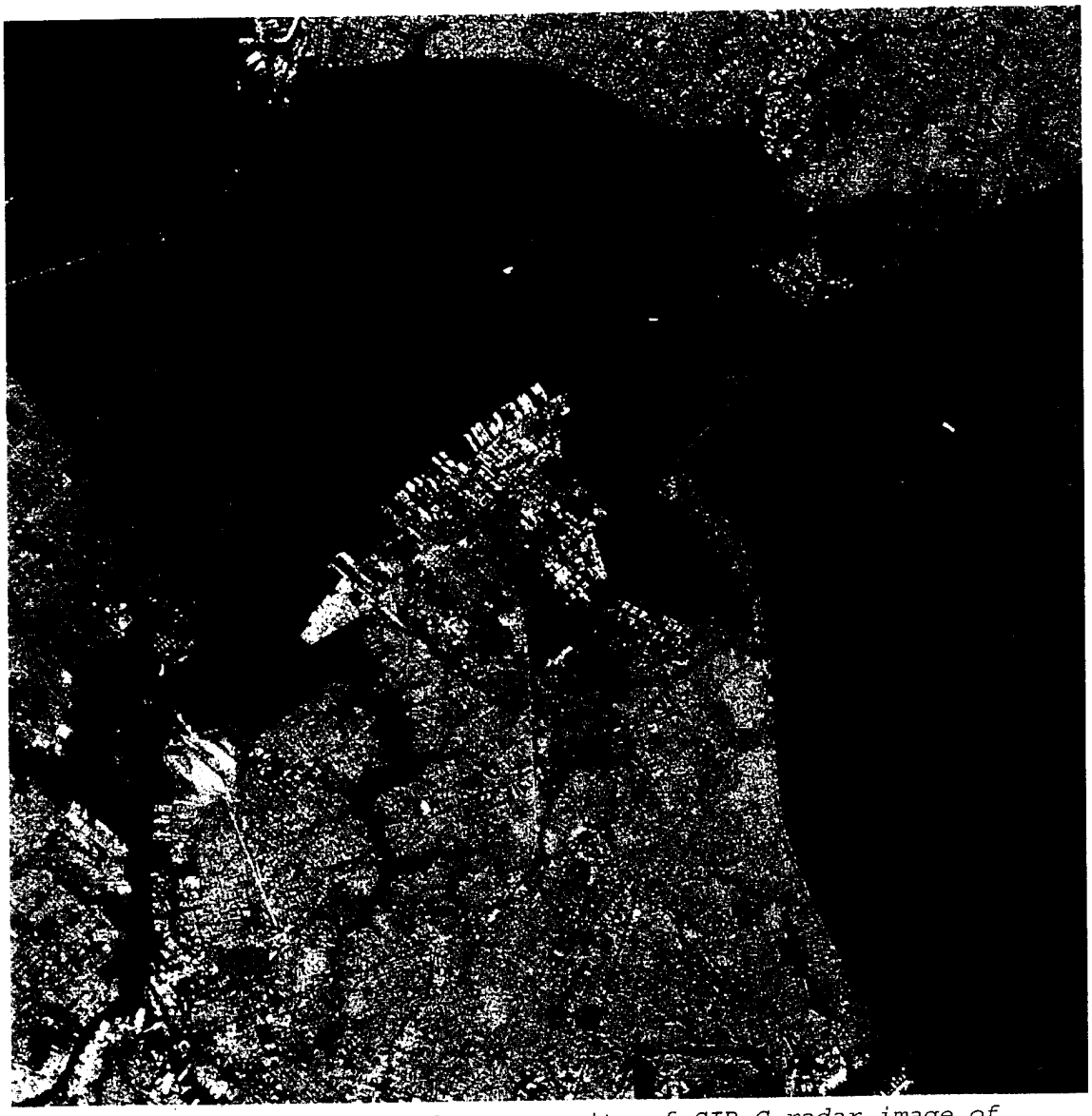

Figure 22: False color composite of SIR-C radar image of Norfolk, Virginia taken from Space Shuttle mission STS-68 in October, 1994. C-band HH polarization is red, C-band HV polarization is green, L-band HH polarization is blue

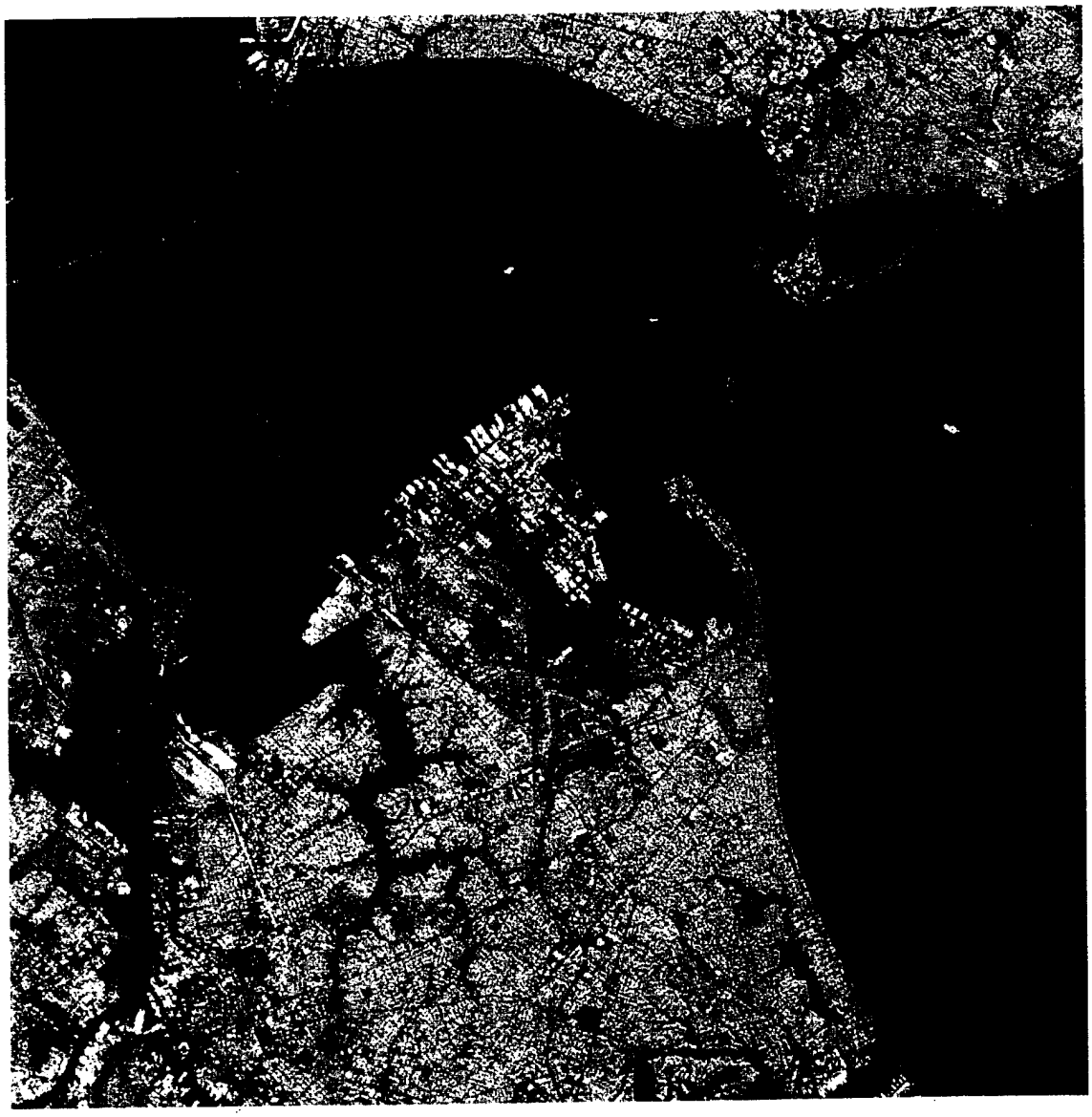

Figure 23: False color composite of SIR-C radar image of Norfolk, Virginia taken from Space Shuttle mission STS-68 in October, 1994. C-band HV polarization is red, L-band HV polarization is green, L-band HH polarization is blue

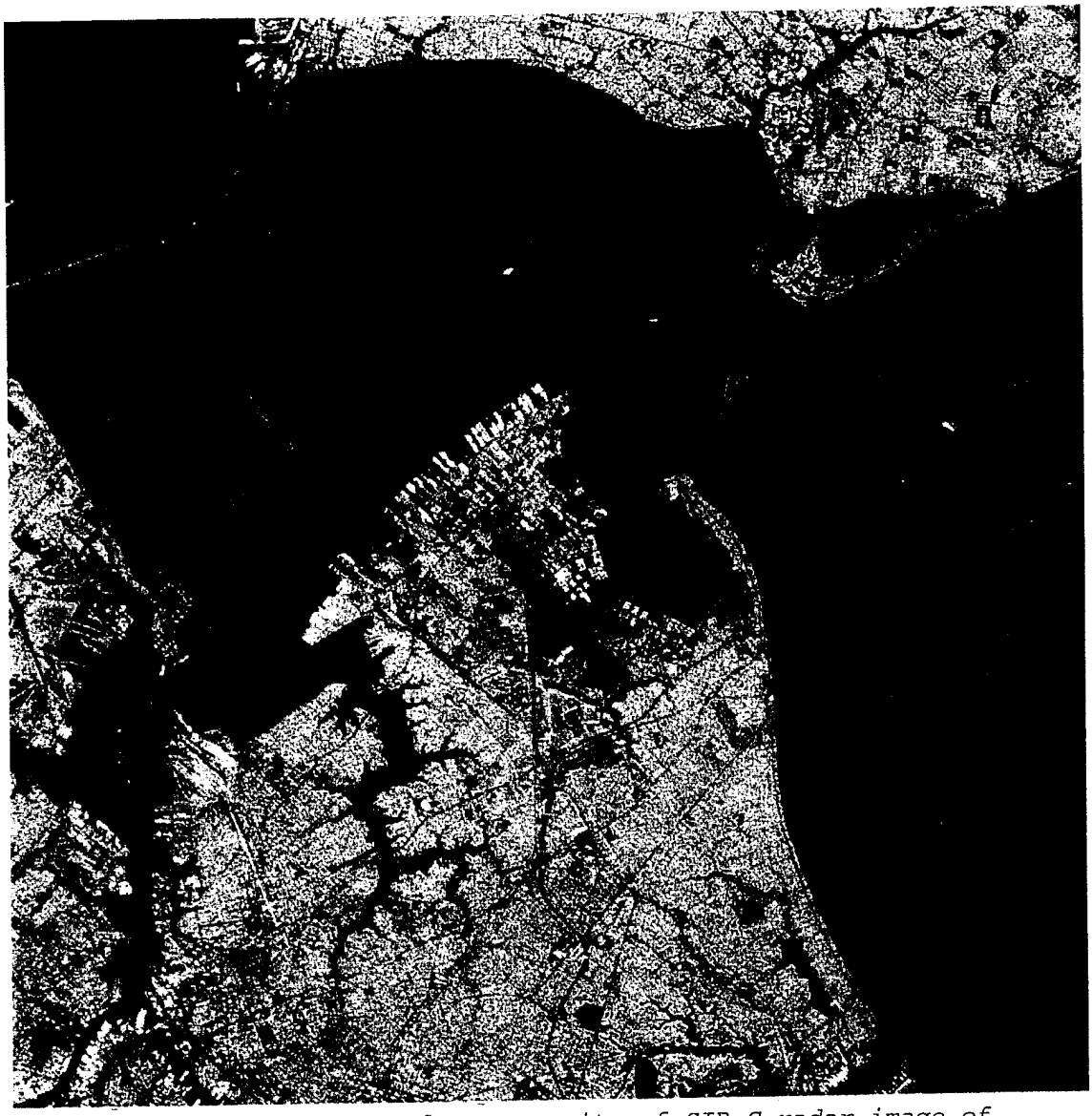

Figure 24: False color composite of SIR-C radar image of Norfolk, Virginia taken from Space Shuttle mission STS-68 in October, 1994. L-band HH polarization is red, L-band HV polarization is green, C-band HV polarization is blue

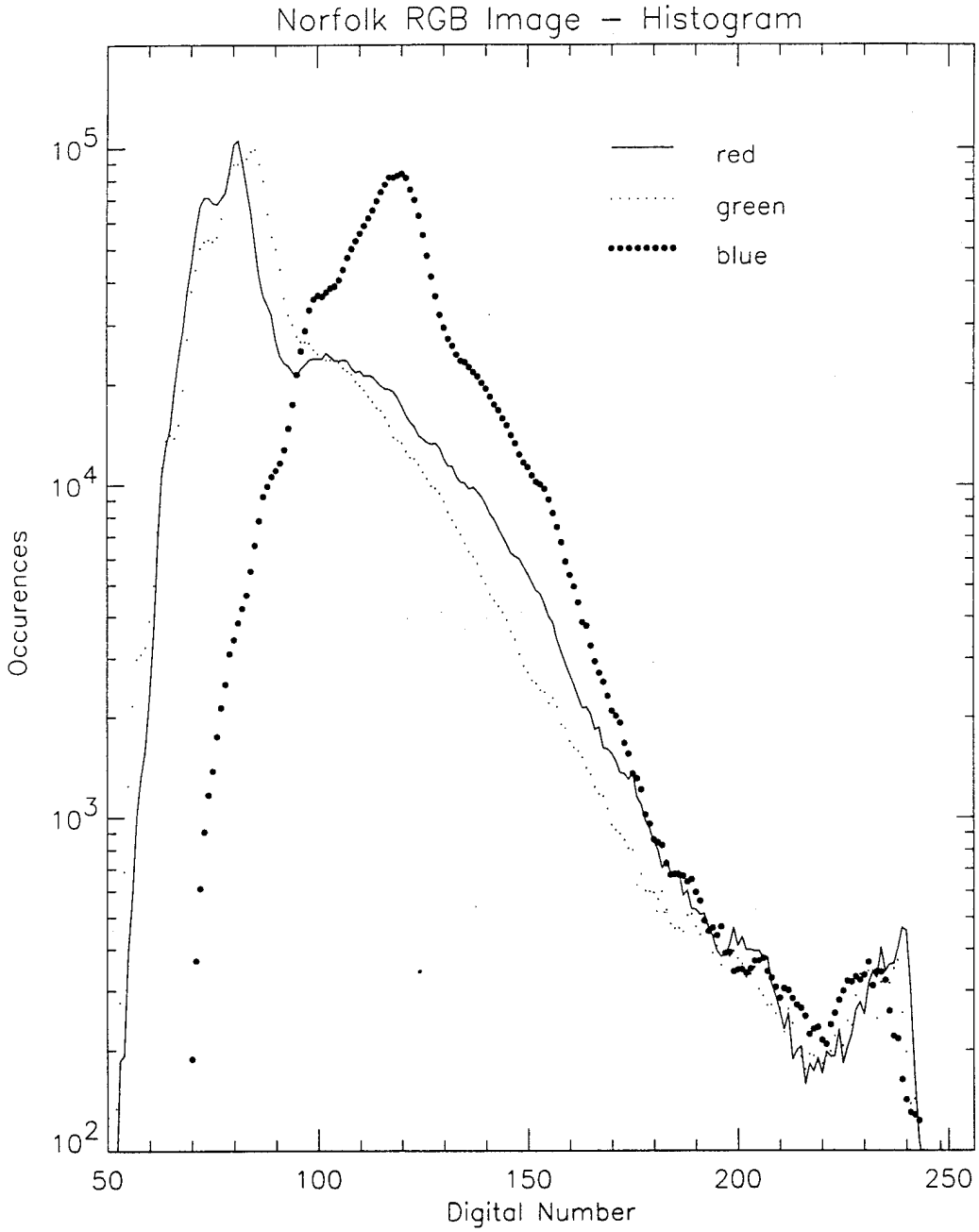

Figure 25: Histogram of red, green, and blue pixels from visible image of Norfolk, Virginia in Figure 19

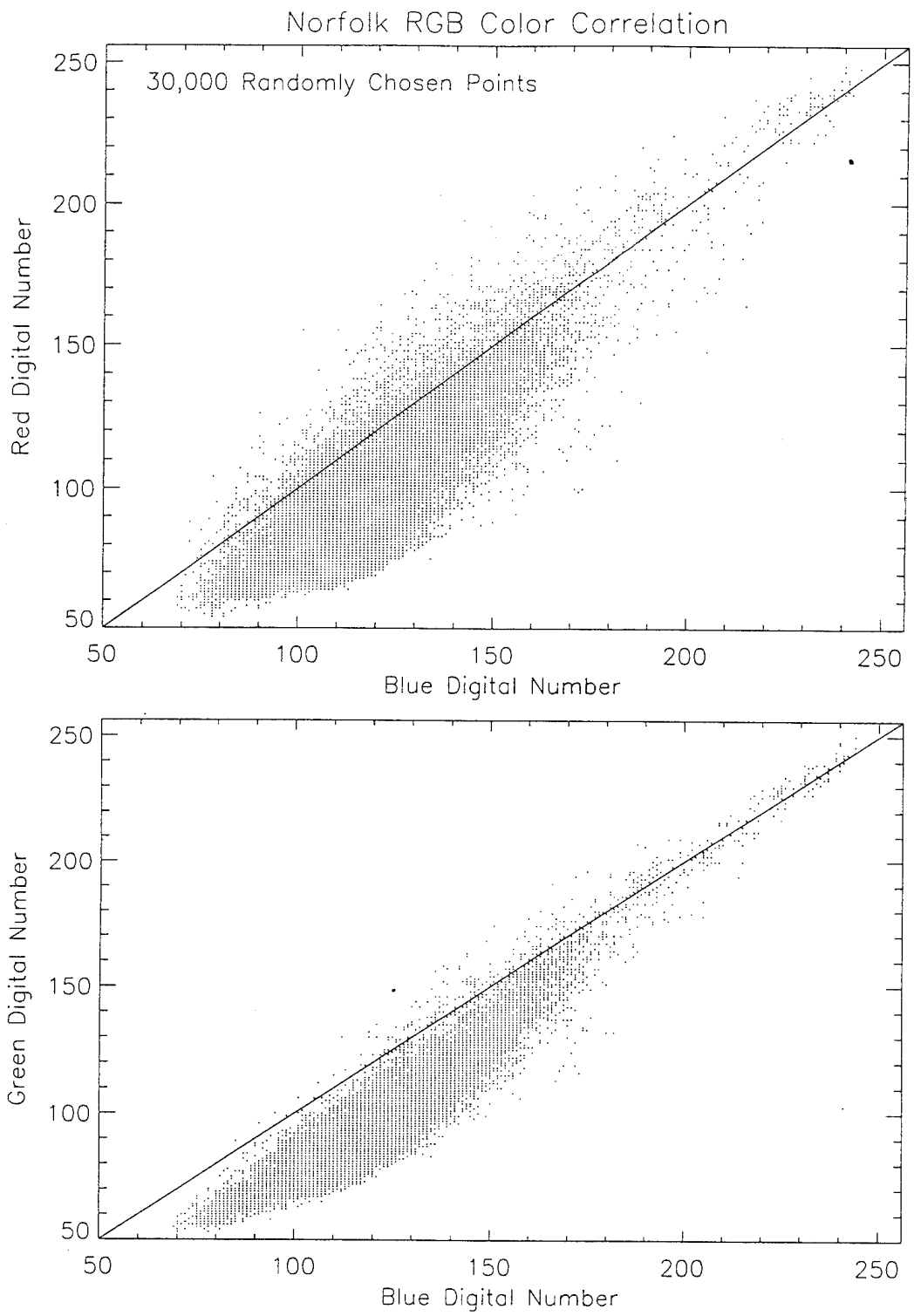

Figure 26: Scatterplots of blue pixels vs red and green pixel from visible image of Norfolk, Virginia in Figure 19

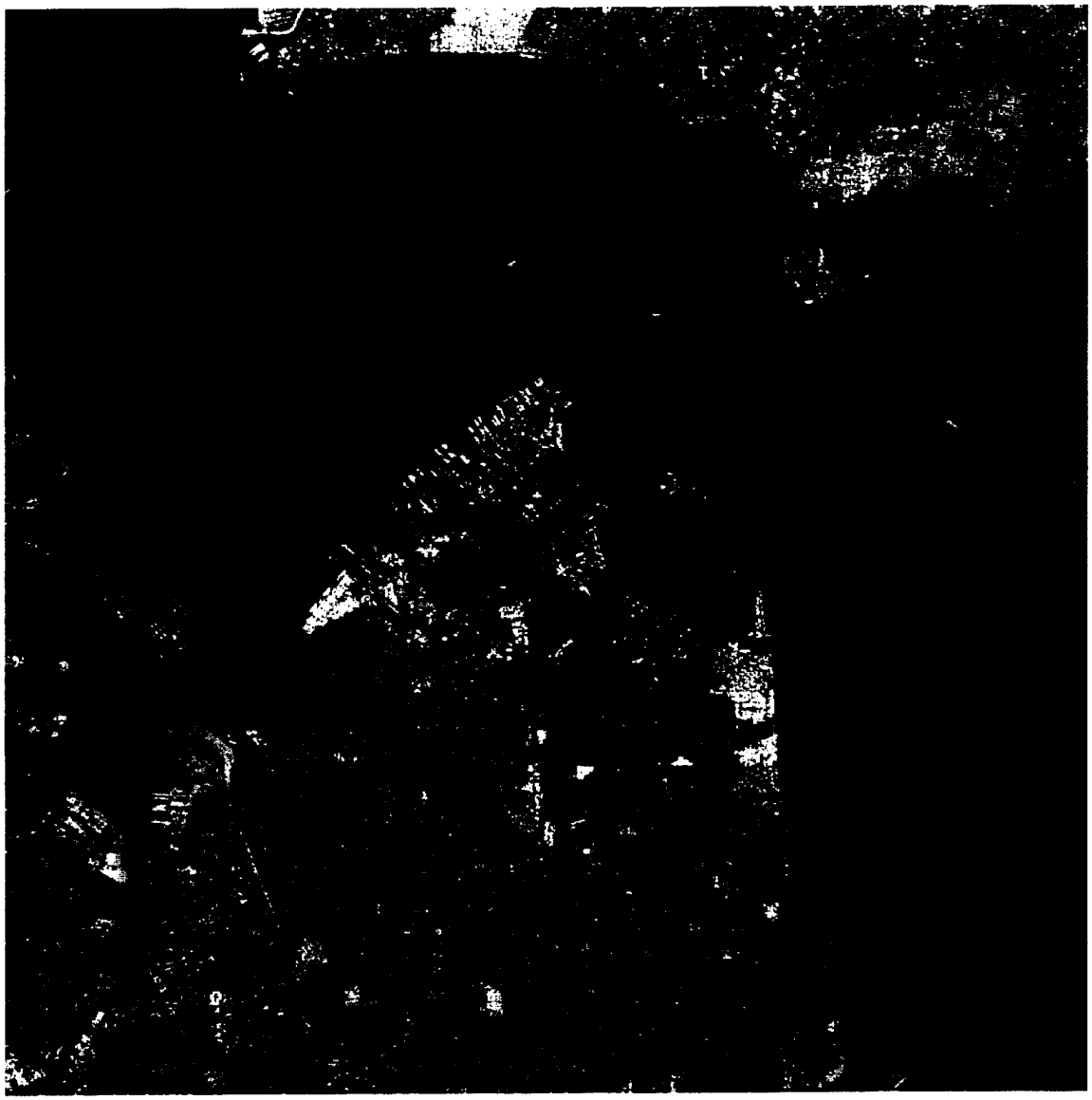

Figure 27: Radar and visible wavelength false color composite image of Norfolk, Virginia taken from Space Shuttle mission STS-68 in October, 1994. C-band HH polarization is red, L-band HH polarization is green, blue band from the visible image is blue

Figure 28: Radar and visible wavelength false color composite image of Norfolk, Virginia taken from Space Shuttle mission STS-68 in October, 1994. C-band HH polarization is red, L-band HV polarization is green, blue band from the visible image is blue

Figure 29: Radar and visible wavelength false color composite image of Norfolk, Virginia taken from Space Shuttle mission STS-68 in October, 1994. C-band HV polarization is red, L-band HH polarization is green, blue band from the visible image is blue

Figure 30: Radar and visible wavelength false color composite image of Norfolk, Virginia taken from Space Shuttle mission STS-68 in October, 1994. C-band HH polarization is red, green band from the visible image is green, L-band HH polarization is blue

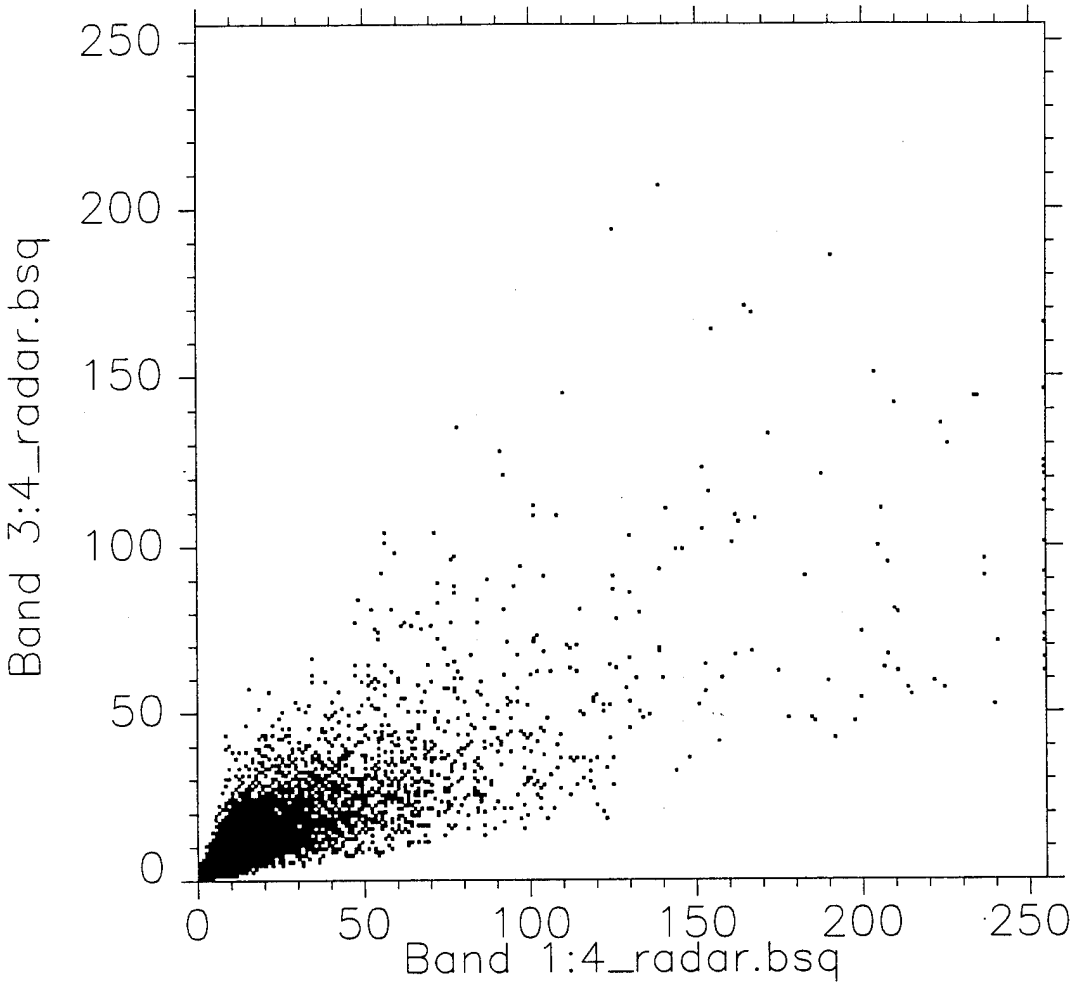

Figure 31: Scatterplot of C-band HH pixel brightness vs L-band HH pixel brightness

Figure 32: First principal component image of Norfolk, Virginia. Input for principal component analysis was four radar bands and three visible color bands

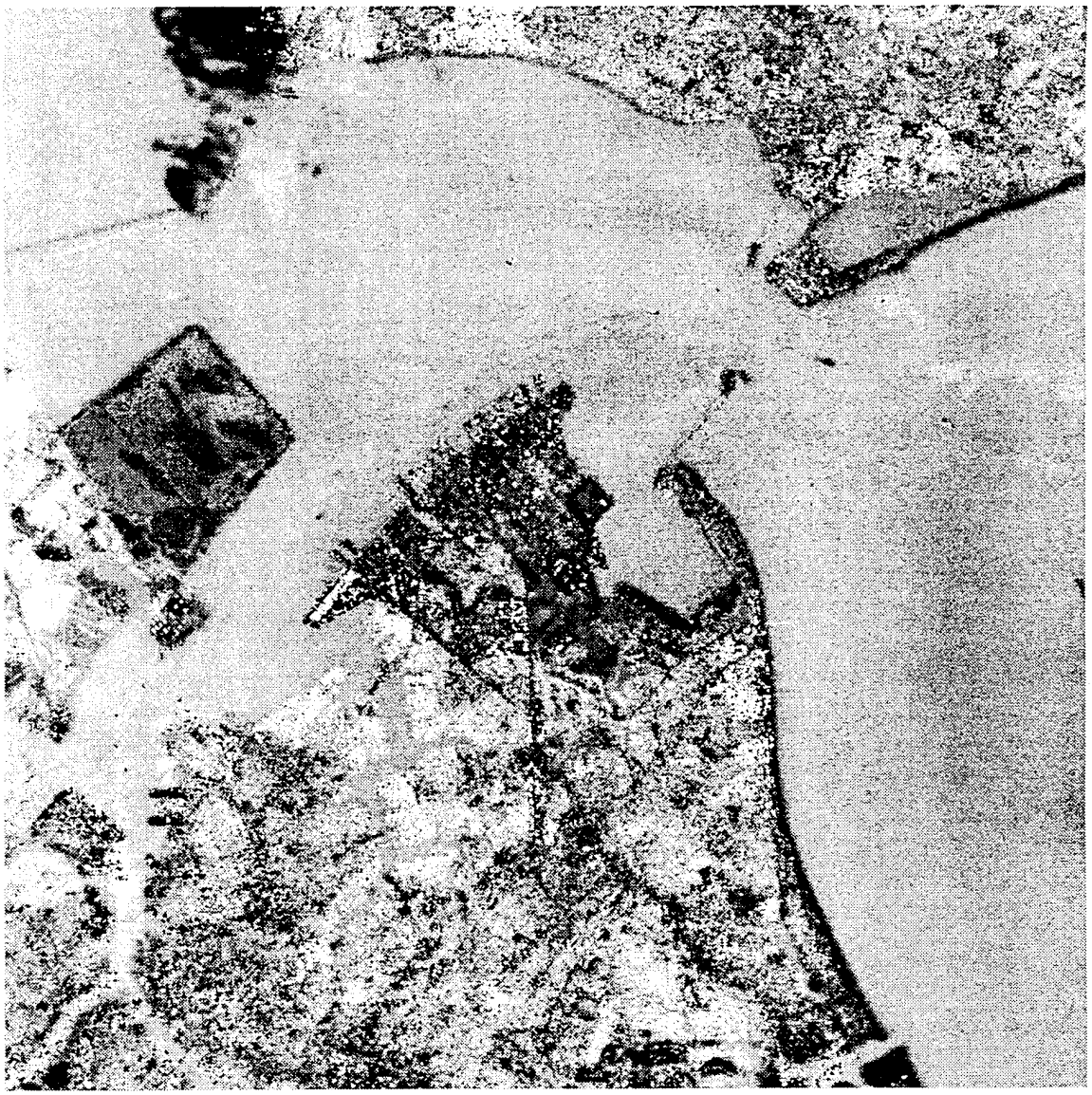

Figure 33: Second principal component image of Norfolk, Virginia. Input for principal component analysis was four radar bands and three visible color bands

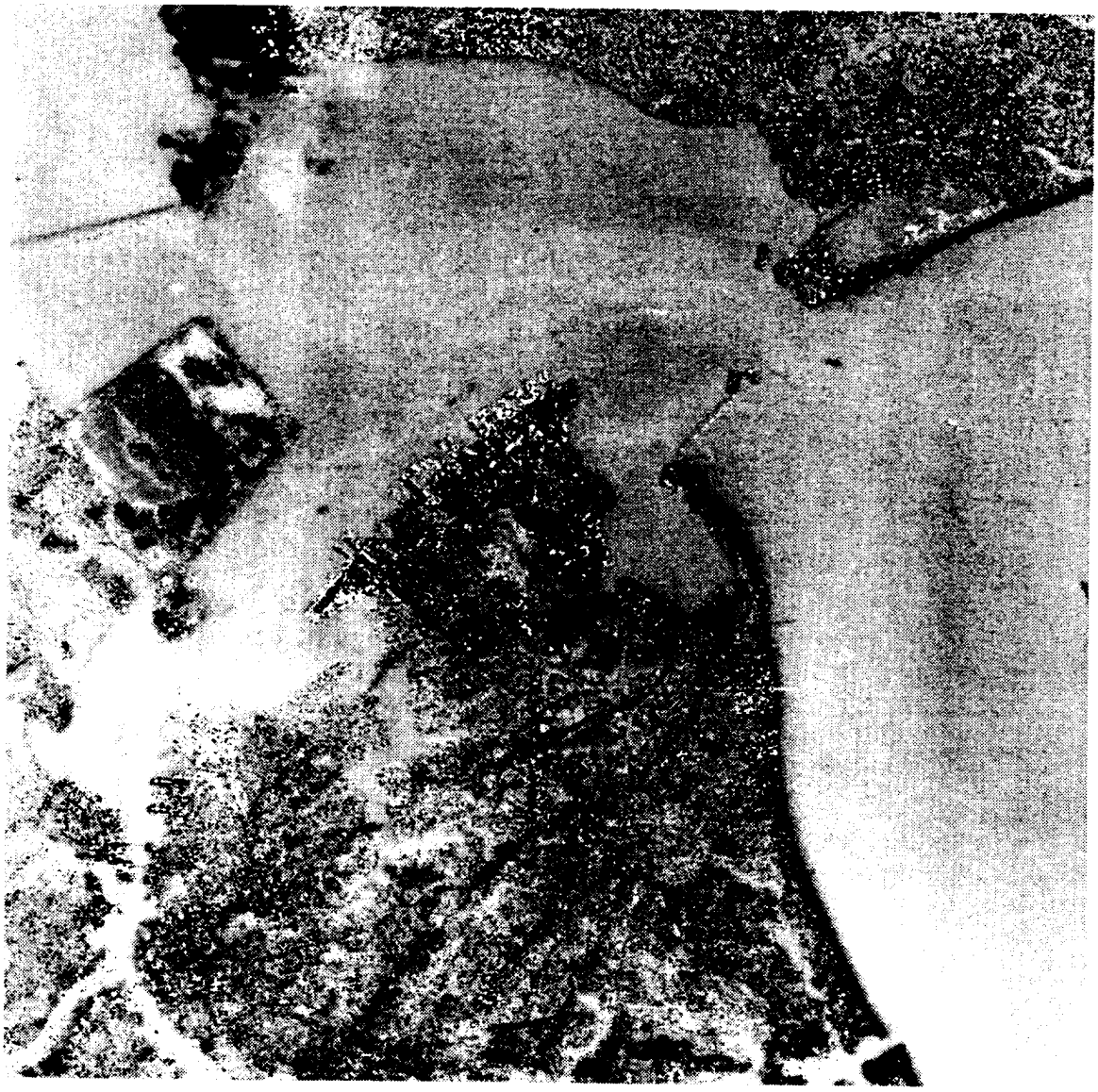

Figure 34: Third principal component image of Norfolk, Virginia. Input for principal component analysis was four radar bands and three visible color bands

Figure 35: Fourth principal component image of Norfolk, Virginia. Input for principal component analysis was four radar bands and three visible color bands

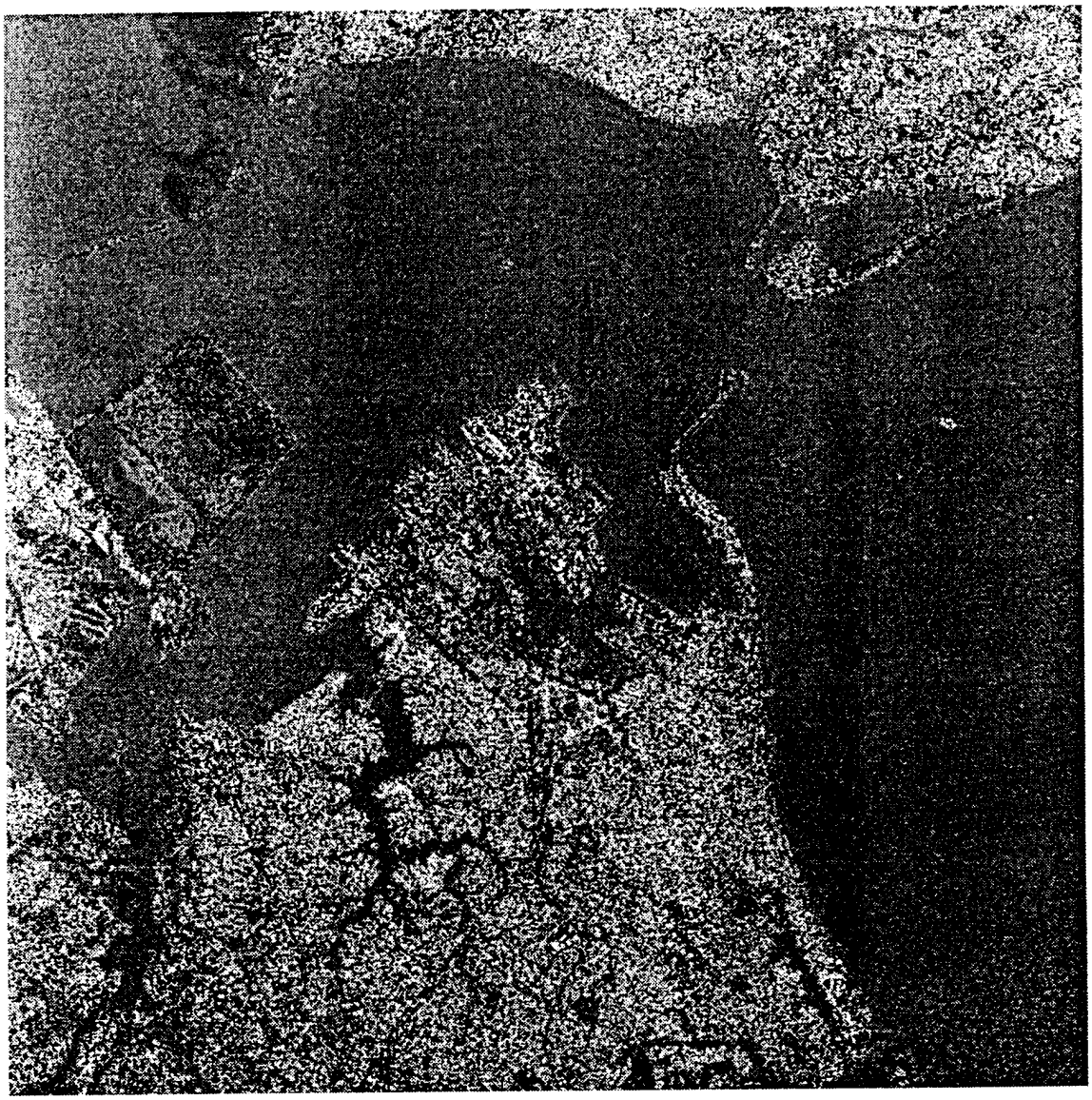

Figure 36: Fifth principal component image of Norfolk, Virginia. Input for principal component analysis was four radar bands and three visible color bands

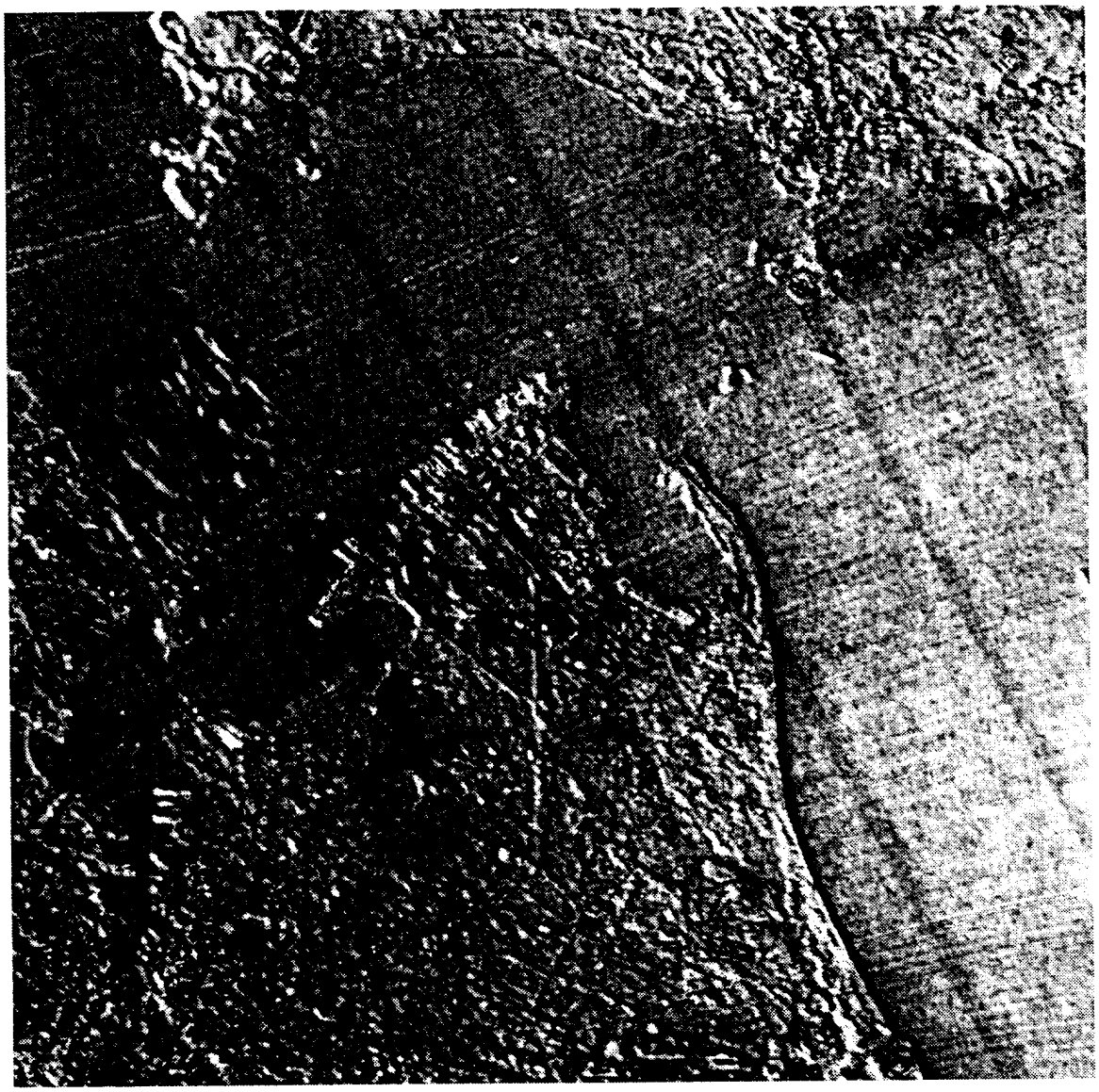

Figure 37: Sixth principal component image of Norfolk, Virginia. Input for principal component analysis was four radar bands and three visible color bands

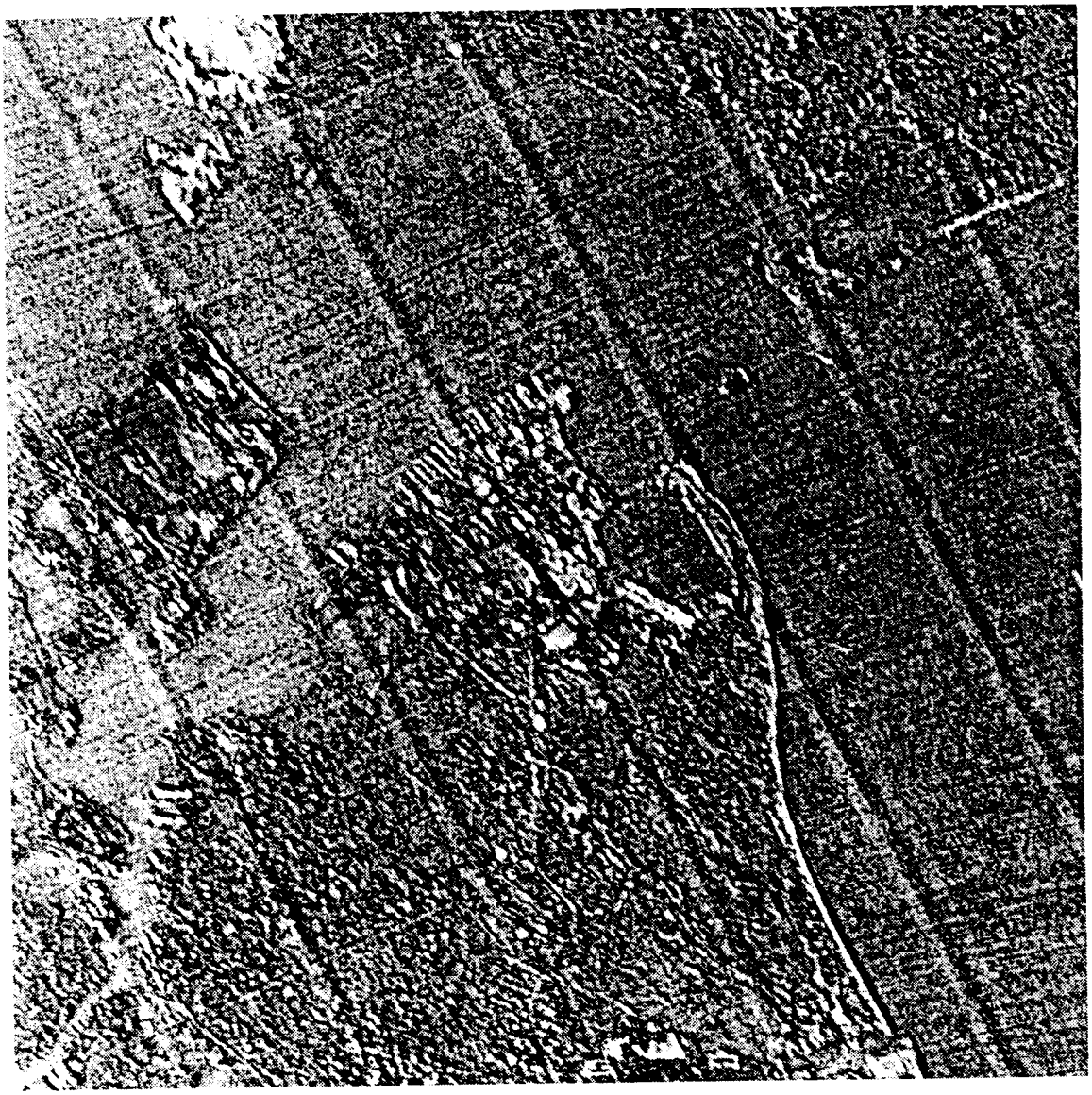

Figure 38: Seventh principal component image of Norfolk, Virginia. Input for principal component analysis was four radar bands and three visible color bands

Figure 39: False color composite image of first three principal component bands out of seven, image is of Norfolk, Virginia. Input for principal component analysis was four radar bands and three visible color bands. First principal component is red, second principal component is green, third principal component is blue.

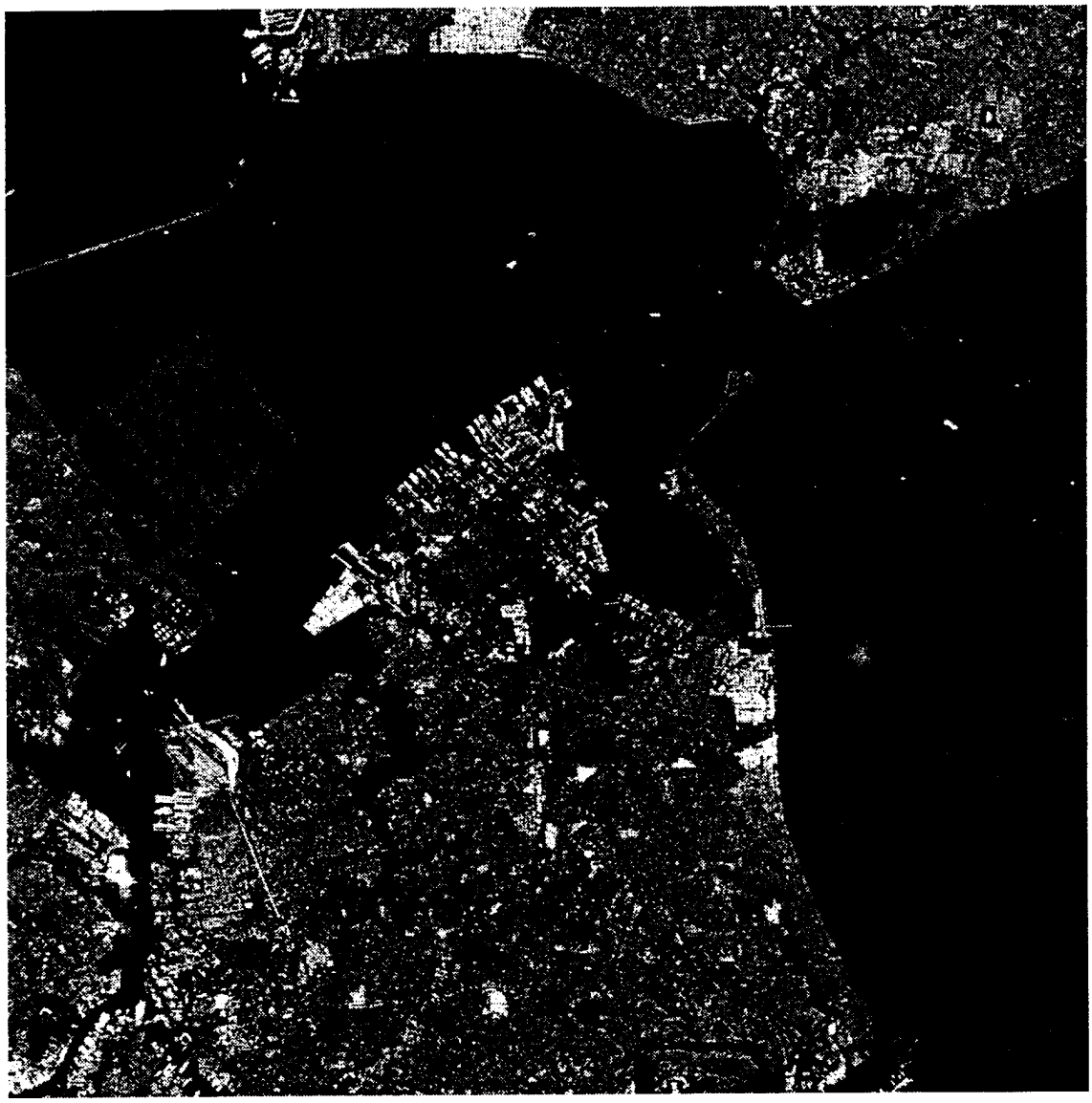

Figure 40: First principal component image of Norfolk, Virginia. Input for principal component analysis was four radar bands.

Figure 41: Second principal component image of Norfolk, Virginia. Input for principal component analysis was four radar bands.

Figure 42: Third principal component image of Norfolk, Virginia. Input for principal component analysis was four radar bands.

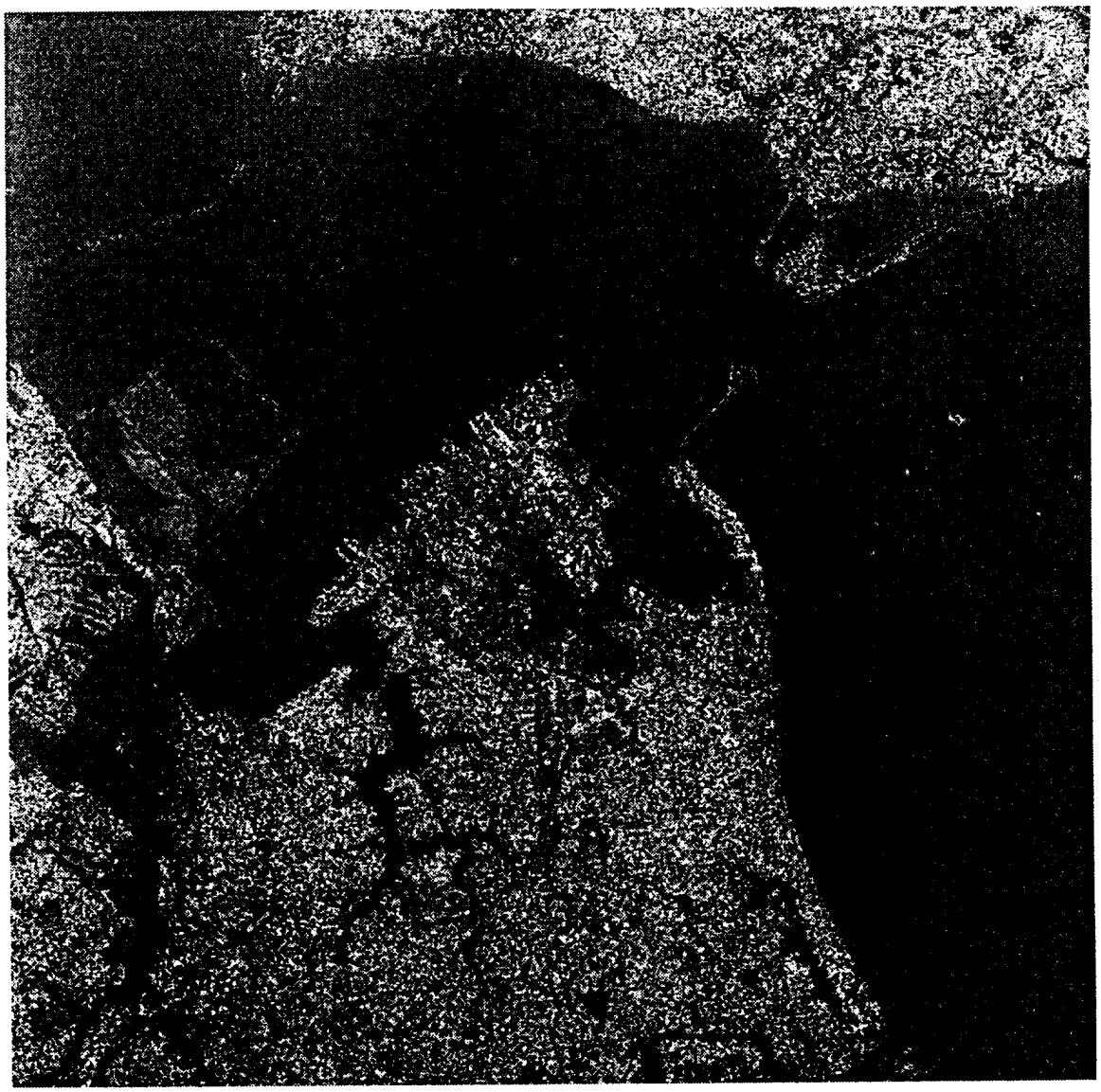

Figure 43: Fourth principal component image of Norfolk, Virginia. Input for principal component analysis was four radar bands.

Figure 44: False color composite image of first three principal component bands out of four, image is of Norfolk, Virginia. Input for principal component analysis was four radar bands. First principal component is red, second principal component is green, third principal component is blue.

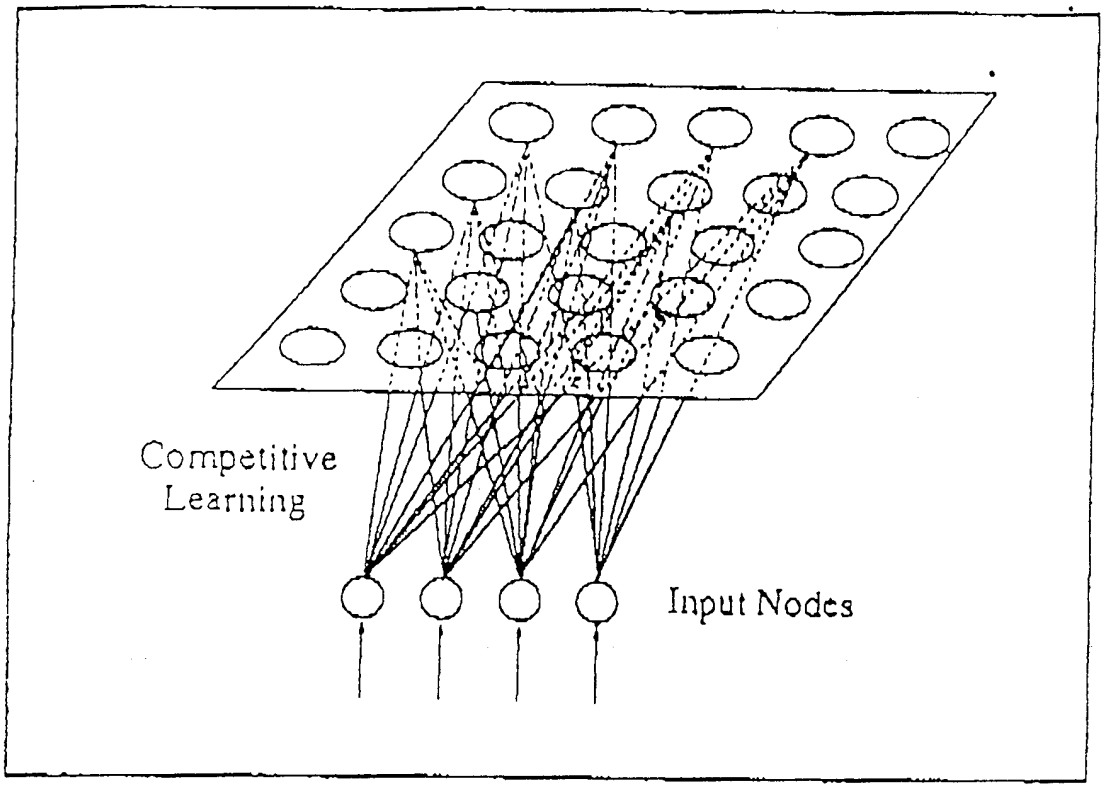

Figure 45: From Chiuderi [1994], Visual representation of neurons in a neural network classifier. Input nodes represent pixels of original image

Figure 46: Results of neural network analysis based on the input of C-band HV and L-band HV radar. seven null categories are represented in black, one classified category is white

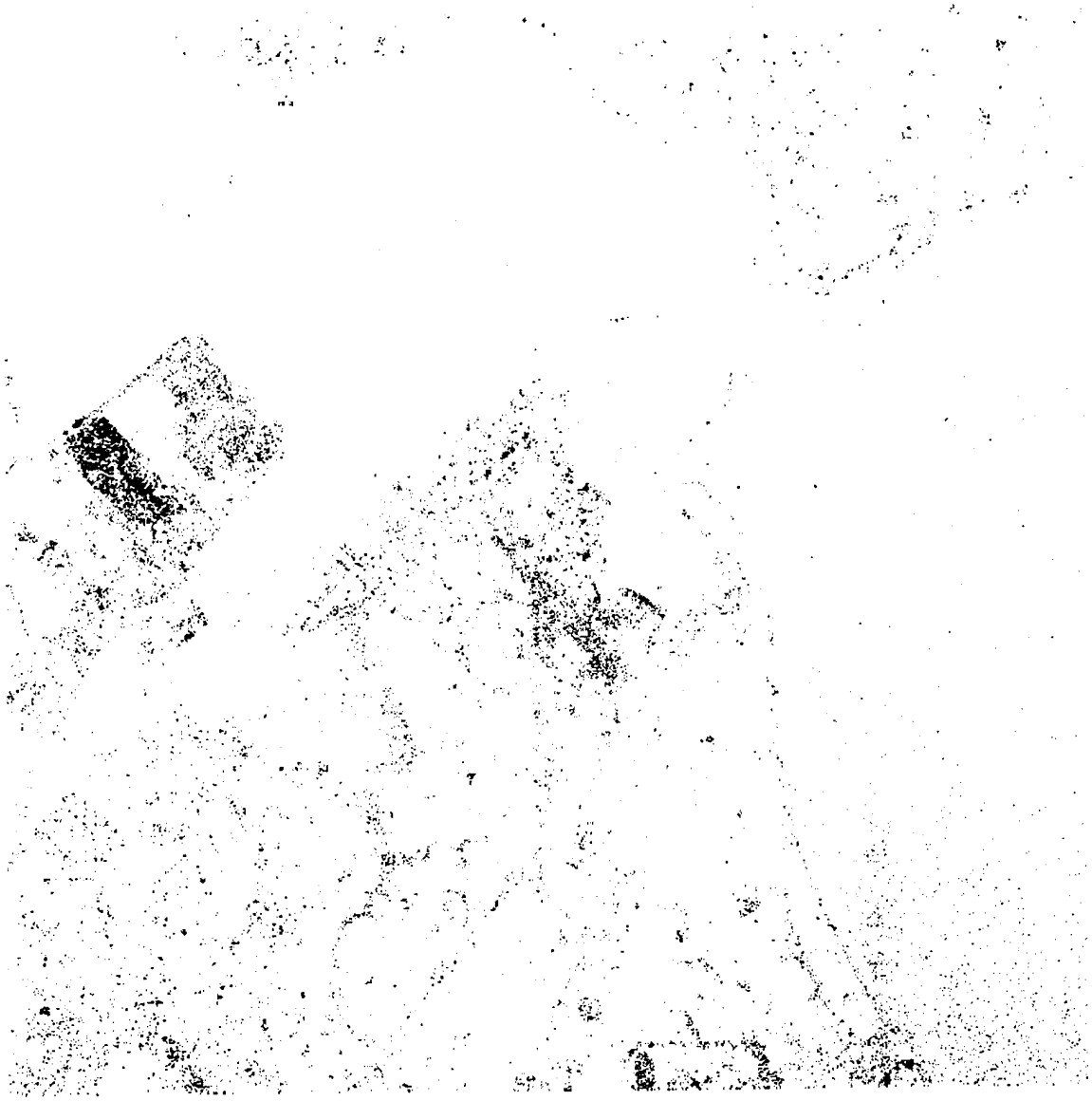

Figure 47: Results of neural network analysis based on the input of C-band HH and L-band HH radar. six null categories are represented in white, two classified categories are red and blue

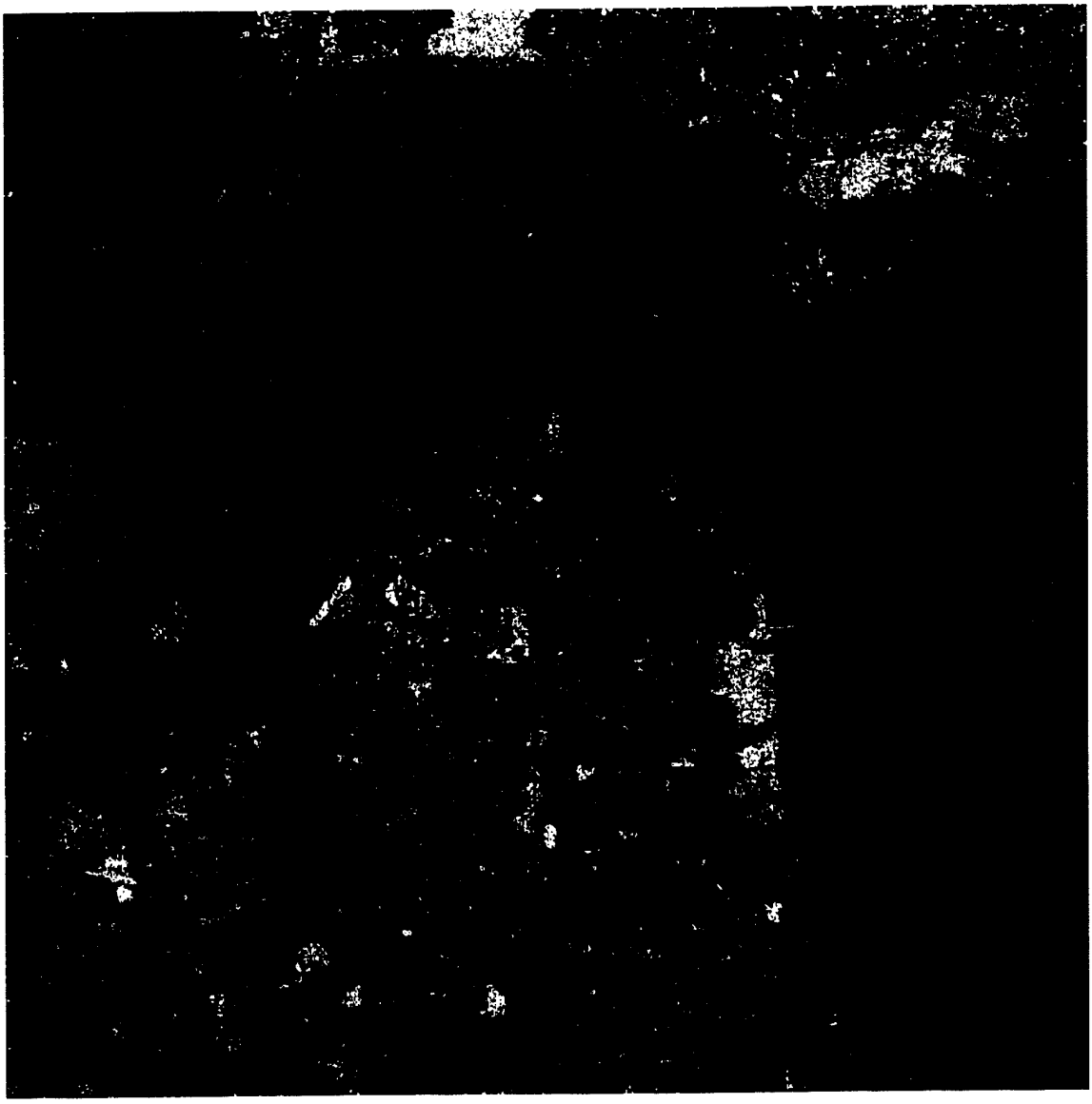

Figure 48: Results of neural network analysis based on the input of all four radar bands. Four null categories are represented in black, four classified categories are represented in red, green, blue, and white

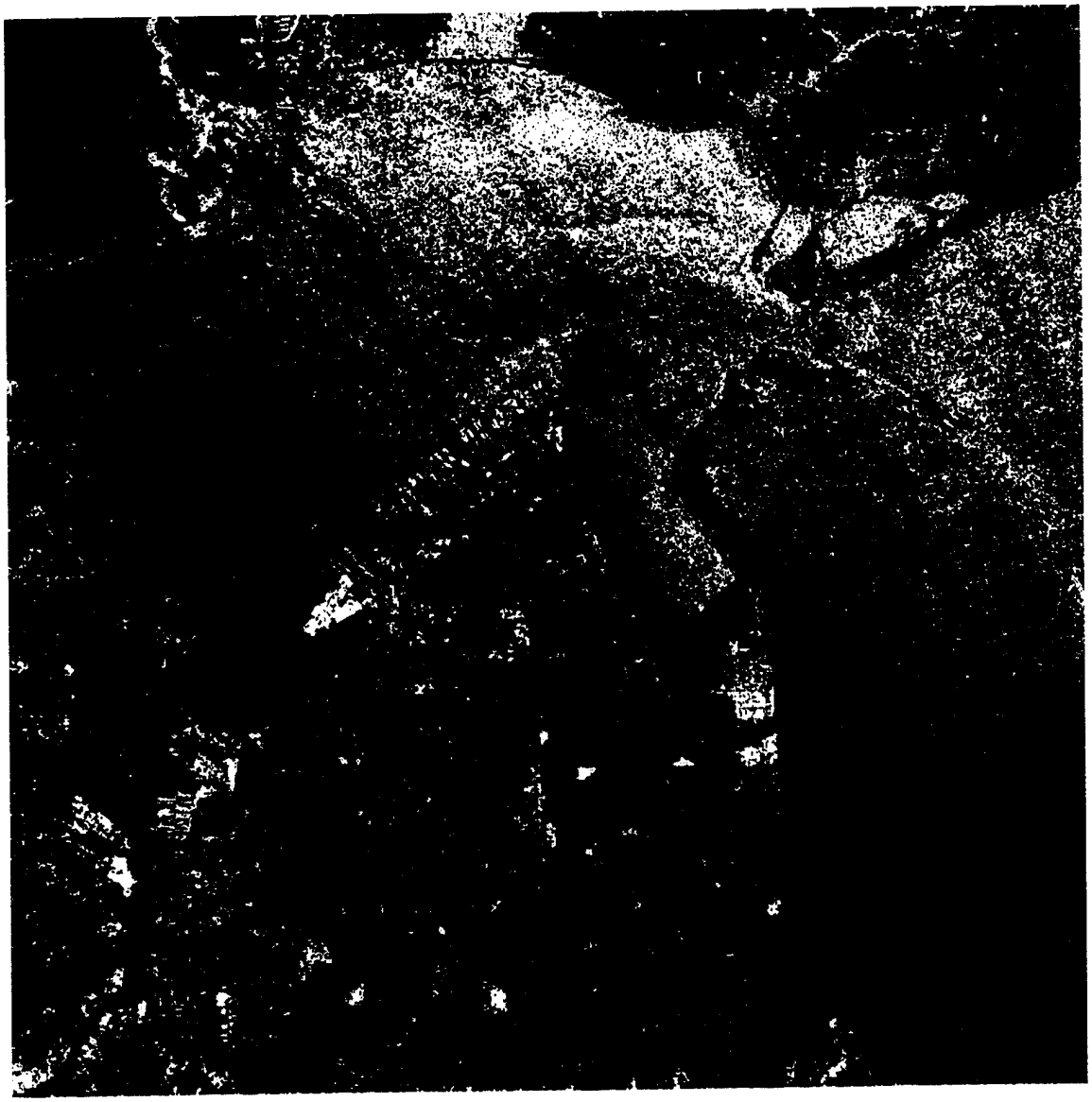

Figure 49: Results of neural network analysis based on the input of all four radar bands and all three visible bands. Three null categories are represented in black, five classified categories are represented in red, green, blue, yellow, and white

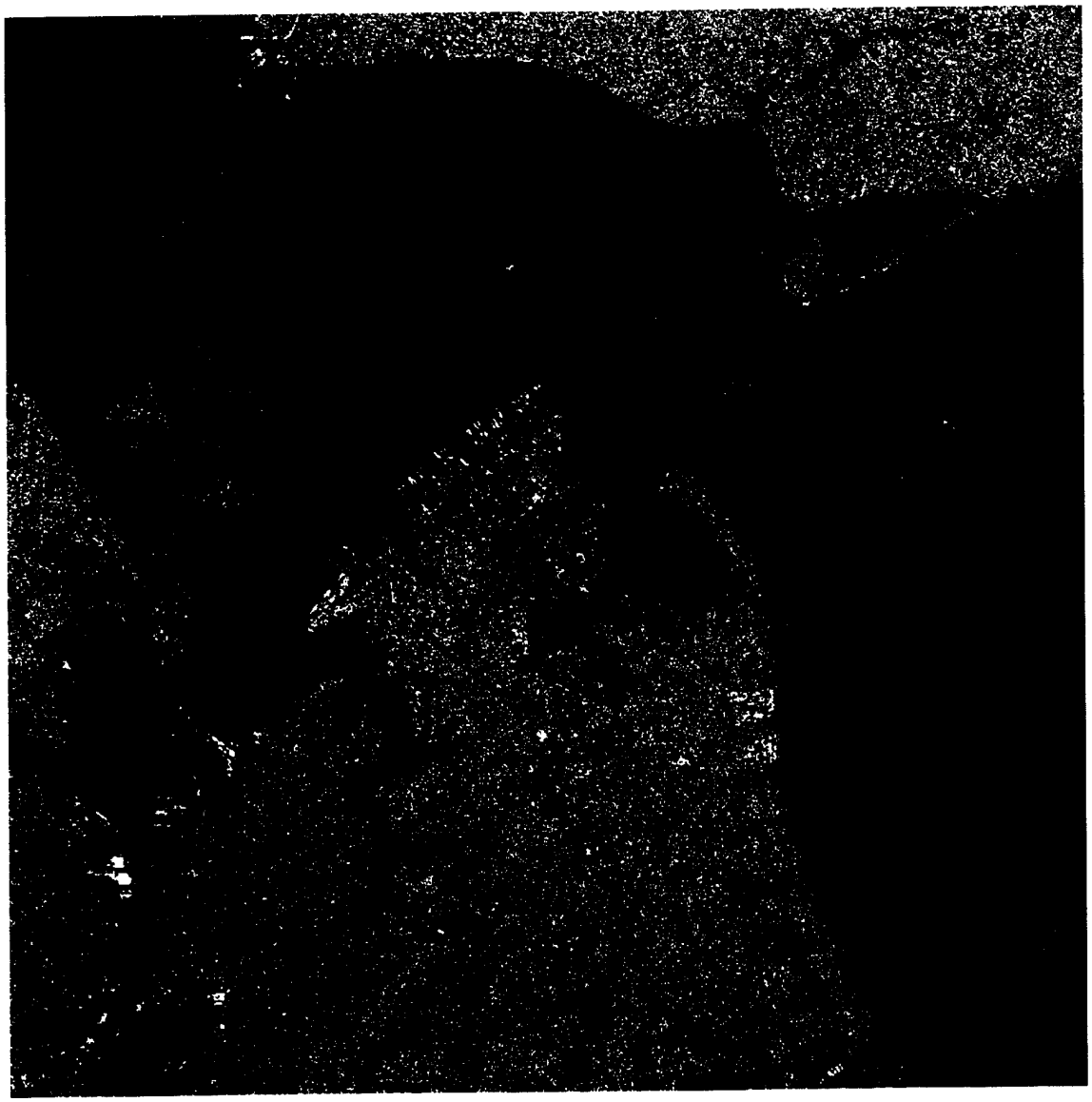

Figure 50: Results of neural network analysis based on the input of seven principal component bands. Inputs to principal component analysis were all four radar bands and all three visible bands. Four null categories are represented in black, four classified categories are represented in red, green, yellow, and white

Figure 51: Results of neural network analysis based on input of the first three of seven principal component bands. Inputs to principal component analysis were all four radar bands and all three visible bands. Four null categories are represented in black, four classified categories are represented in red, green, yellow, and white

LIST OF REFERENCES

Avery, T., Berlin, G., "Fundamentals of Remote Sensing and Airphoto Interpretation", Macmillan Publishing Company, 1985

Chavez, P.S., "Digital Merging of Landsat TM and Digitized NHAP Data for 1:24,000 Scale Image Mapping", Photogrammetric Engineering and Remote Sensing, Volume 52, October, 1986

Chiuderi, A., Fini, F., Cappelline, V., "An Application of Data Fusion to Landcover Classification of Remote Sensed Imagery: A Neural Network Approach", Proceedings of the IEEE International Conference on Multisensor Fusion and Integration for Intelligent Systems, October, 1994

Elachi, C., "Introduction to The Physics and Techniquies of Remote Sensing", John Wiley and Sons, 1987

Elachi, C., "Spaceborne Radar Remote Sensing: Applications and Techniques", IEEE Press, 1988

Freeman, T. , Chapman, B., " What is SIR-C/XSAR", Jet Propulsion Labratory, World Wide Web, 1994

Fung, A. K., Ulaby, F.T., "Manual of Remote Sensing", Chapter 4, American Society of Photogrammetry, 1983

Gautreaux, M. M., "Hyperspectral Imagery Analysis Using Neural Network Techniques", Master's Thesis, Naval Postgraduate School, Monterey, CA, June, 1995

Guindon, B., Harris, J.W.E., Teillet, P.M., Goodenough, D.G., Meunier, G.F., "Integration of MSS and SAR Data of Forested Regions in Mountainous Terrain", Proceedings of the Fourteenth International Symposium on Remote Sensing of Environment, Volume III, April, 1980

Gupta, R.P., "Remote Sensing Geology", Springer-Verlag, 1991

Haydn, R., Dalke, G.W., Henkle, J., Bare, J.E., "Application of the IHS Color Transform to the Processing of Multisensor Data and Image Enhancement", proceedings of the International Symposium on Remote Sensing of Arid and Semi-Arid Lands, Cairo, Egypt, 1982

Hoffer, R.M., "Combination of Landsat TM and ERS-1 Satellite Data to Discriminate Forest Cover Types in Brazil", Multispectral and Microwave Sensing of Forestry Hydrology, and Natural Resources, Mougin, Ranson, and Smith, SPIE Volume 2314, 1995

Kramer, H., "Earth Observation Remote Sensing", Springer-Verlag, 1992

Larson, D., "Engineering Conference on Synthetic Aperture Radar Technology and Applications", Chapter 16, University of Michigan, 1994

Leckie, D.G., "Synergism of Synthetic Aperture Radar and Visible/Infrared Data For Forest Type Discrimination", Photogrammetric Engineering and Remote Sensing, Volume 56, September, 1990

Lozano-Garcia, D.F., Hoffer, R.M., "Synergistic Effects of Combined Landsat-TM and SIR-B Data For Forest Resources Assessment", International Journal of Remote Sensing, Volume 14, 1993

McDonald, R.A., "CORONA: Success for Space Reconnaissance, A Look into the Cold War, and a Revolution for Intelligence", Photogrammetric Engineering and Remote Sensing, June, 1995

Moore, R.K., Chastant, L.J., Porcello, L., Stevenson, J., "Manual of Remote Sensing", Chapter 10, American Society of Photogrammetry, 1983

Newhall, B., "Airborne Camera", Hastings House Publishers, 1969

Onstott, R., "Engineering Conference on Synthetic Aperture Radar Technology and Applications", Chapter 10, University of Michigan, 1994

PCI Inc., "Using PCI Software", PCI Inc, Richmond Hill, Ontario, Canada, 1994

Richards, J.A., "Remote Sensing Digital Image Analysis", Springer-Verlag, 1993

Welch, R., Ehlers, M., "Merging Multiresolution SPOT HRV and Landsat TM Data", Photogrammetric Engineering and Remote Sensing, Volume 53, March 1987

Simonett, D.S., "Manual of Remote Sensing", Chapter 1, American Society of Photogrammetry, 1983

Strain, P., Engle, F., "Looking at Earth", Turner Publishing Inc, 1993

Wu, S.T., "Multisensor Data Analysis and its Application to Monitoring of Cropland, Forest, Strip Mines, and Cultural Targets", Machine Processing of Remotely Sensed Data Symposium, July, 1982

INITIAL DISTRIBUTION LIST

1. Defense Technical Information Center.....2
   Cameron Station
   Alexandria, Virginia 22304-6145

2. Library, Code 52.....2
   Naval Postgraduate School
   Monterey, California 93943-5101

3. Dr. R. C. Olsen.....3
   Code PH/OS
   Naval Postgraduate School
   Monterey, California 93943

4. Dr. William B. Colson.....1
   Code PH
   Naval Postgraduate School
   Monterey, California 93943

5. Andrew M. Hartigan.....1
   3212 Wynford Dr
   Fairfax, Virginia 22031

6. Andrew G. Hartigan.....2
   626 E. Burlwood La
   Lemoore, California 93245

7. Sue Runco.....1
   NASA Johnson Space Center
   SN-5 NASA Rd 1
   Houston, Texas 77058